Calhoun: The NPS Institutional Archive

DSpace Repository

Theses and Dissertations | 1. Thesis and Dissertation Collection, all items

2022-12

SEABED MORPHOLOGICAL PREDICTION WITH APPLICATION TO MOBILITY AND BURIAL OF MUNITIONS

Santos Pessanha, Vinicius

Monterey, CA; Naval Postgraduate School

https://hdl.handle.net/10945/71541

Copyright is reserved by the copyright owner.

Downloaded from NPS Archive: Calhoun

http://www.nps.edu/library

Calhoun is the Naval Postgraduate School's public access digital repository for research materials and institutional publications created by the NPS community. Calhoun is named for Professor of Mathematics Guy K. Calhoun, NPS's first appointed -- and published -- scholarly author.

Dudley Knox Library / Naval Postgraduate School
411 Dyer Road / 1 University Circle
Monterey, California USA 93943

NAVAL POSTGRADUATE SCHOOL

MONTEREY, CALIFORNIA

DISSERTATION

SEABED MORPHOLOGICAL PREDICTION WITH APPLICATION TO MOBILITY AND BURIAL OF MUNITIONS

by

Vinicius Santos Pessanha

December 2022

Dissertation Supervisor: Peter C. Chu

Approved for public release. Distribution is unlimited.

THIS PAGE INTENTIONALLY LEFT BLANK

REPORT DOCUMENTATION PAGE	*Form Approved OMB No. 0704-0188*

Public reporting burden for this collection of information is estimated to average 1 hour per response, including the time for reviewing instruction, searching existing data sources, gathering and maintaining the data needed, and completing and reviewing the collection of information. Send comments regarding this burden estimate or any other aspect of this collection of information, including suggestions for reducing this burden, to Washington headquarters Services, Directorate for Information Operations and Reports, 1215 Jefferson Davis Highway, Suite 1204, Arlington, VA 22202-4302, and to the Office of Management and Budget, Paperwork Reduction Project (0704-0188) Washington, DC, 20503.

1. AGENCY USE ONLY *(Leave blank)*	**2. REPORT DATE** December 2022	**3. REPORT TYPE AND DATES COVERED** Dissertation

4. TITLE AND SUBTITLE
SEABED MORPHOLOGICAL PREDICTION WITH APPLICATION TO MOBILITY AND BURIAL OF MUNITIONS

5. FUNDING NUMBERS

6. AUTHOR(S) Vinicius Santos Pessanha

7. PERFORMING ORGANIZATION NAME(S) AND ADDRESS(ES)
Naval Postgraduate School
Monterey, CA 93943-5000

8. PERFORMING ORGANIZATION REPORT NUMBER

9. SPONSORING / MONITORING AGENCY NAME(S) AND ADDRESS(ES)
SERDP, Alexandria, VA 22350

10. SPONSORING / MONITORING AGENCY REPORT NUMBER

11. SUPPLEMENTARY NOTES The views expressed in this thesis are those of the author and do not reflect the official policy or position of the Department of Defense or the U.S. Government.

12a. DISTRIBUTION / AVAILABILITY STATEMENT
Approved for public release. Distribution is unlimited.

12b. DISTRIBUTION CODE
A

13. ABSTRACT (maximum 200 words)

Hundreds of sites in littoral and inland waters across the United States have been reported as possibly containing underwater munitions, a safety hazard for the general public. Therefore, it is critical to determine and predict munition location and depth to implement remediation strategies. The mobility of munitions may be influenced by currents, waves, and seafloor slope. Burial depth may be affected by scour, sediment accretion, wave-induced liquefaction, and bedform migration. Here, environmental conditions and morphological evolution are investigated by examining observational data and modeling analyses to better understand the physical processes influencing the burial and mobility of munitions. The environmental models (Delft3D) are validated using observations from field experiments. A coupled Delft3D-object model capable of predicting the mobility and burial of objects on a sandy seafloor is presented. Although the object model limitation considers only cylindrical objects on flat seafloor, ignoring pitch and yaw movements, the coupled Delft3D-object model predictions agree well with observations. In addition, processes such as sediment transport, wave-induced liquefaction, and sand wave migration are examined. The findings show that environmental conditions from Delft3D can be used as a forcing term by other models (e.g., object and wave-induced liquefaction models), which is a valuable tool for predicting the fate of munitions.

14. SUBJECT TERMS
morphological modeling, sandy seafloor, munitions mobility and burial, object mobility model, Delft3D, Shields parameter, sediment scour, sediment accretion, wave-induced liquefaction, sand wave migration

15. NUMBER OF PAGES
149

16. PRICE CODE

17. SECURITY CLASSIFICATION OF REPORT	**18. SECURITY CLASSIFICATION OF THIS PAGE**	**19. SECURITY CLASSIFICATION OF ABSTRACT**	**20. LIMITATION OF ABSTRACT**
Unclassified	Unclassified	Unclassified	UU

NSN 7540-01-280-5500

Standard Form 298 (Rev. 2-89)
Prescribed by ANSI Std. 239-18

THIS PAGE INTENTIONALLY LEFT BLANK

Approved for public release. Distribution is unlimited.

SEABED MORPHOLOGICAL PREDICTION WITH APPLICATION TO MOBILITY AND BURIAL OF MUNITIONS

Vinicius Santos Pessanha
Capitao-de-Corveta, Brazilian Navy
BS, Brazilian Naval Academy, 2007
MS, Naval Postgraduate School, 2019

Submitted in partial fulfillment of the
requirements for the degree of

DOCTOR OF PHILOSOPHY IN PHYSICAL OCEANOGRAPHY

from the

NAVAL POSTGRADUATE SCHOOL
December 2022

Approved by:

Peter C. Chu
Department of Oceanography
Dissertation Supervisor
Dissertation Chair

Matthew K. Gough
Department of METOC and
USW Programs Office

Mara S. Orescanin
Department of Oceanography

Timour Radko
Department of Oceanography

Qing Wang
Department of Meteorology

Joseph Calantoni
Naval Research Laboratory

Approved by:

Peter C. Chu
Chair, Department of Oceanography

Joseph P. Hooper
Vice Provost of Academic Affairs

THIS PAGE INTENTIONALLY LEFT BLANK

ABSTRACT

Hundreds of sites in littoral and inland waters across the United States have been reported as possibly containing underwater munitions, a safety hazard for the general public. Therefore, it is critical to determine and predict munition location and depth to implement remediation strategies. The mobility of munitions may be influenced by currents, waves, and seafloor slope. Burial depth may be affected by scour, sediment accretion, wave-induced liquefaction, and bedform migration. Here, environmental conditions and morphological evolution are investigated by examining observational data and modeling analyses to better understand the physical processes influencing the burial and mobility of munitions. The environmental models (Delft3D) are validated using observations from field experiments. A coupled Delft3D-object model capable of predicting the mobility and burial of objects on a sandy seafloor is presented. Although the object model limitation considers only cylindrical objects on flat seafloor, ignoring pitch and yaw movements, the coupled Delft3D-object model predictions agree well with observations. In addition, processes such as sediment transport, wave-induced liquefaction, and sand wave migration are examined. The findings show that environmental conditions from Delft3D can be used as a forcing term by other models (e.g., object and wave-induced liquefaction models), which is a valuable tool for predicting the fate of munitions.

THIS PAGE INTENTIONALLY LEFT BLANK

TABLE OF CONTENTS

I. INTRODUCTION....1

II. COUPLED DELFT3D-OBJECT MODEL TO PREDICT MOBILITY OF MUNITIONS ON SANDY SEAFLOOR....5
A. INTRODUCTION....5
B. STUDY AREA....7
C. TREX13....9
1. Surrogate Munitions....9
2. Field Experiment....11
3. Data....12
D. DELFT3D....15
1. Model Description....15
2. Model Grids and Time Steps....15
3. Wind and Tidal Forcing....16
4. Initial and Boundary Conditions....17
5. Model Output....18
E. OBJECT MOBILITY MODEL....20
F. OBJECT SCOUR MODEL....22
G. PREDICTION OF OBJECT'S MOBILITY AND BURIAL....24
H. CONCLUSIONS....29
I. INTRODUCTION....31
J. FIELD EXPERIMENT....32
1. Study Area....32
2. Instrumentation....33
3. Time Series of Observed Data....34
K. MODELING SYSTEM....36
1. Grids, Bathymetry, and Wind Input....37
2. Initial and Boundary Conditions....37
3. Calibration and Model Parameters....38
L. RESULTS AND DISCUSSION....39
1. Consecutive Cold Fronts....39
2. Model Performance....40
3. Hydrodynamics....42
4. Morphological Changes....44
M. CONCLUSION....50

III. COUPLED MODEL PREDICTIONS OF WAVE-INDUCED LIQUEFACTION AND MORPHOLOGICAL CHANGES 53
A. INTRODUCTION 53
B. MATERIALS AND METHODS 55
1. Study Area and Field Experiment 55
2. The Hydro-morphodynamic Model: Approach and Setup 57
3. Wave-Induced Liquefaction Model 60
4. Simulation Design and Model Performance Assessment 62
C. RESULTS 62
1. Model Validation 62
2. Seafloor Evolution 65
3. Liquefaction Degree and Failure Depth 68
D. DISCUSSION 70
1. Impact of Waves and Currents on Morphological Changes 70
2. Tide Stations and Observed Sinking of the Shallow Quadpod 71
3. Factors Impacting Liquefaction 73
E. CONCLUSION 75

IV. OBSERVATIONS AND 3D MODEL SIMULATION OF SAND WAVE MIGRATION IN SHALLOW WATER ENVIRONMENT 77
A. INTRODUCTION 77
B. MATERIALS AND METHODS 80
1. Study Area and Field Experiment 80
2. Model Approach and Set-up 82
3. Simulation Design and Model Performance Assessment 85
C. RESULTS 86
1. Model Calibration 86
2. Model Validation 88
3. Sensitivity Studies 90
D. DISCUSSION 91
1. Tidal Flow Asymmetry, Wind, and Surface Waves 91
2. Influence of Tidal Currents and Surface Waves on Sand Wave Migration 93
3. Rotation of the Sand Wave 97
E. SUMMARY AND CONCLUSIONS 99

V. CONCLUSION 103

APPENDIX A. LOCATION OF OBJECT'S ROTATION AXIS IN SEDIMENT 107

APPENDIX B. DYNAMICS OF ROLLING OBJECT 109

APPENDIX C. DRAG, LIFT, BUOYANCY FORCES, AND ADDED MASS 113

APPENDIX D. DRAG COEFFICIENT 115

LIST OF REFERENCES 117

INITIAL DISTRIBUTION LIST 127

THIS PAGE INTENTIONALLY LEFT BLANK

LIST OF FIGURES

Figure 1. Flow chart of the coupled Delft3D-object model to predict objects' mobility and burial 7

Figure 2. Northern Gulf of Mexico off the coast of Panama City 8

Figure 3. Surface east-west and north-south wind component for the study area 9

Figure 4. Fabricated surrogate, purchased replica, and fabricated replica. Adapted from Calantoni et al. (2014). 10

Figure 5. Layout of objects laid by divers under the shallow quadpod. Adapted from Calantoni et al. (2014). 13

Figure 6. Study area with bathymetry 16

Figure 7. Time series of the environmental parameters 19

Figure 8. Roll of a cylindrical object on the seafloor 20

Figure 9. Time series of sediment Shields parameter (θ_{sed}) at the shallow quadpod computed from the Delft3D model output 23

Figure 10. Model predicted burial percentage $p_B(t)$ 25

Figure 11. Model predicted objects' mobility parameters for percentage burial (θ_{opb}) 27

Figure 12. Model predicted displacement $l(t)$ for each object 28

Figure 13. Positions for all visible objects at the shallow quadpod location. Panels (a) and (b) are adapted from Calantoni et al. (2014). 29

Figure 14. Northern Gulf of Mexico map 33

Figure 15. Time series of observed current magnitude, significant wave height, and seafloor elevation 35

Figure 16. Bathymetry, depth contours, and computational grids enclosures 38

Figure 17. Surface analysis including passage of cold fronts through the northern Gulf of Mexico during 3–6 May 2013. Adapted from NOAA/WPC (2020) 40

Figure 18. Comparison between observed and predicted water level 42
Figure 19. Comparison between observed and predicted significant wave height (H_s), wave peak period (T_p), and mean wave direction (θ) 43
Figure 20. Comparison between observed and predicted cross-shore and alongshore current 44
Figure 21. Sediment accretion time series at the shallow quadpod location 45
Figure 22. Sonar images and predicted seafloor elevation 47
Figure 23. Time evolution of the cross-shore erosion/accretion of sediment 48
Figure 24. Development of the cross-shore bed level profile 49
Figure 25. Model results for suspended and bedload sediment transport at the shallow quadpod location 50
Figure 26. Study area and model domain 57
Figure 27. Bathymetry and bathymetric contours 59
Figure 28. Model validation 64
Figure 29. Sonar images 66
Figure 30. Predicted erosion/accretion of sediment 67
Figure 31. Predicted sediment transport and observed seafloor elevation 68
Figure 32. Liquefaction degree (L) time series at shallow and deep quadpod locations 69
Figure 33. Liquefaction degree (L) map computed from model output 70
Figure 34. Shields parameter time series 71
Figure 35. Water level difference between stations 72
Figure 36. Scatter plots of liquefaction degree (L), depth, dissipation of wave energy, wave steepness, and relative water depth 74
Figure 37. Study area and limits of model grids 81
Figure 38. Bathymetry in the study area 82
Figure 39. Model calibration for hydrodynamics 86

Figure 40. Model calibration for morphology 87
Figure 41. Model validation for hydrodynamics 88
Figure 42. Observed and simulated bathymetric change 89
Figure 43. Model performance for morphology 90
Figure 44. Bed level profiles along transect 3 for cases I, II, and III 91
Figure 45. Tidal flow asymmetry, wind, and surface waves 92
Figure 46. Predicted mean sand wave migration speed and Shields parameter 95
Figure 47. Predicted mean sand wave migration speed and Shields parameter for a period with no large surface wave events 96
Figure 48. Bed level profiles along transects 1 and 7 for cases I and II 97
Figure 49. Shields parameter map 99
Figure 50. Axis of rotation of the cylinder in the sediment 108
Figure 51. Forces and torques on a partially buried cylinder 110

THIS PAGE INTENTIONALLY LEFT BLANK

LIST OF TABLES

Table 1. List of surrogate and replica munitions used during TREX13. Adapted from Calantoni et al. (2014). 10

Table 2. Sediment properties. Adapted from Calantoni et al. (2014). 14

Table 3. Qualification of model performance using RMAE for wave height and current magnitude. Adapted from van Rijn et al. (2003). 41

Table 4. Qualification of model performance using RMSE and bias. Adapted from Williams and Esteves (2017). 41

Table 5. Qualification of model performance using BSS for morphological changes. Adapted from van Rijn et al. (2003). 41

Table 6. Seafloor and sea water properties applied to the analytical solution 61

THIS PAGE INTENTIONALLY LEFT BLANK

LIST OF ACRONYMS AND ABBREVIATIONS

3D	three-dimensional
DDB	Delft Delft3D dashboard
Delft3D-Flow	flow module of Delft3D
Delft3D-MOR	morphology module of Delft3D
Delft3D-Wave	wave module of Delft3D
ECMWF	European Centre for Medium-Range Weather Forecasts
JONSWAP	Joint North Sea Wave Project
NDBC	National Data Buoy Center
NGDC	National Geophysical Data Center
NOAA	National Oceanic and Atmospheric Administration
SERDP	Strategic Environmental Research and Development Program
SWAN	Simulating Waves Nearshore
TREX13	Target Reverberation Experiment 2013

THIS PAGE INTENTIONALLY LEFT BLANK

ACKNOWLEDGMENTS

This dissertation could not have been finished without the support of my advisor, Prof. Peter C. Chu. I will be eternally grateful to you for allowing me to work with you on this project. These were years of many challenges that were only overcome thanks to your guidance and steady motivation. Thank you for your patience, mentorship, and determination to teach.

Thanks go also to the members of my committee. I want to thank Prof. Timour Radko for his advice and encouragement throughout the years. Prof. Mara Orescanin made several excellent comments, all of which helped to strengthen the dissertation. I've benefited greatly from talks with Dr. Matt Gough, and I want to thank him for participating in my research and his comments on my papers. I also appreciate Dr. Joseph Calantoni and Prof. Qing Wang's willingness to serve on the committee, as well as their support and time.

Special thanks to the Department of Oceanography staff and faculty. Your professionalism and dedication have always been one of the sources of my motivation and inspiration.

To my wife, Thiciane, and children, Pedro and Ana, thank you for your love, patience, and support. My parents, Nelson and Lucia, and my brothers, Wellington and Bruno, deserve particular thanks for their help and dedication in these years I've been so far away.

Thanks to Dr. Joseph Calantoni and Dr. Peter Traykovski for providing the field data, without which the completion of this research would have been impossible. Finally, I want to thank the Brazilian Navy for supporting my academic growth and education.

THIS PAGE INTENTIONALLY LEFT BLANK

I. INTRODUCTION

A survey conducted by the U.S. Army Corps of Engineers, Navy, and Marine Corps considering the location of former military bases and records of shipwrecks, ocean disposal operations, accidents, and training areas identified more than 430 sites in the coastal and inland waters throughout the United States as possibly containing underwater munitions (SERDP 2010; Pessanha 2019). Because most of these identified locations are in shallow water, the general public is at risk. Moreover, releasing chemical components from munitions may endanger human health and marine life, underscoring the relevance of taking well-planned measures to address this issue (Chu et al. 2021).

The location and burial depth of munitions are essential to underwater munition remediation. On a sandy seabed, the location of munitions may be affected by the mobility induced by currents, waves, and seafloor slope, whereas burial depth may be impacted by scour driven by currents, sediment accretion, wave-induced liquefaction, and bedform migration. Numerical models can predict the environmental conditions and can therefore be an effective tool for determining the mobility and burial of munitions.

In this study, the physical processes influencing the burial and mobility of munitions are investigated by analyzing data from two field experiments and modeling studies. The numerical models described in Chapters II, III, and IV are validated using results from a field experiment conducted near Panama City, Florida. Additionally, the model validation in Chapter V uses observational data from a field experiment that took place in Martha's Vineyard, Massachusetts. The overall objective of this dissertation is to model the hydro-morphodynamic forcing, improving the understanding of the physical processes causing mobility and burial of munitions.

This dissertation is composed of four journal papers (Chapters II–V): two published papers and two papers submitted for peer review. Each paper is self-contained and has its own distinct sections, including an introduction, methods, results, discussion, and conclusion. All papers addressed the local hydrodynamics, which may affect munitions mobility. Moreover, the morphological processes impacting the burial of

munitions are covered as follows, scour in Chapter II, sediment transport in Chapter III, wave-induced liquefaction in Chapter IV, and sand wave migration in Chapter V. In addition to this introductory chapter, Chapter VI summarizes conclusions from the four journal papers. A brief overview of each of Chapters II–V is provided below.

Chapter II, "Coupled Delft3D-Object Model to Predict Mobility of Munitions on Sandy Seafloor" published by *Fluids* (Chu et al. 2021), presents a coupled Delft3D-object model to predict the mobility and burial of objects on the sandy seafloor. The Delft3D model is used to predict environmental factors, including currents, waves, and water level changes. These variables are used as the forcing term for the object model, which includes the dynamics of a rolling cylinder around its major axis and an empirical sediment scour model with re-exposure parameterization. Observational data are used to validate the model. This chapter was completed under the direct guidance of Dr. Chu. My author contributions included writing the original draft (primarily in the introduction, study area, and Delft3D model description), the Delft3D model setup, calibration, validation, and visualization.

Chapter III, "Sediment Accretion in a Lower-Energetic Location during Two Consecutive Cold Fronts" published by the *Journal of Operational Oceanography* (Pessanha et al. 2022), examines changes in the seafloor elevation during the passage of two consecutive cold fronts using the Delft3D model to predict the local hydrodynamics and morphological evolution. The model results are compared with field measurements that include the burial of munitions observed by sonar images.

Chapter IV, "Coupled Model Predictions of Wave-Induced Liquefaction and Morphological Changes" submitted to the *Journal of Sea Research* for peer review, implements a coupled hydro-morphodynamic and wave-induced liquefaction model to predict morphological changes and seafloor instability causing the burial of munitions.

Chapter V, "Observations and 3D Model Simulation of Sand Wave Migration in Shallow Water Environment" submitted to the *International Journal of Sediment Research* for peer review, investigates the physical processes causing the fast migration and the rotational aspect of sand waves of approximately 2 m in height observed near the

southeastern corner of Martha's Vineyard, Massachusetts. A three-dimensional model is implemented to reproduce the local hydro-morphodynamics, including the complex bathymetry, tidal forcing, winds, and surface waves.

THIS PAGE INTENTIONALLY LEFT BLANK

II. COUPLED DELFT3D-OBJECT MODEL TO PREDICT MOBILITY OF MUNITIONS ON SANDY SEAFLOOR

This chapter was previously published by *Fluids* (Chu et al. 2021). Co-authors include Peter C. Chu[1], Vinícius S. Pessanha,[1] Chenwu Fan[1], and Joseph Calantoni.[2] Content related to this research has also been published by IEEE (Chu et al. 2022). In addition, as part of this research effort, Dr. Chu's interim report published by the Strategic Environmental Research and Development Program (SERDP) (Chu 2020) reported on the earlier progress of this research by Dr. Chu.

A. INTRODUCTION

The U.S. Army Corps of Engineers and the Navy have identified more than 400 underwater sites potentially contaminated with munitions (SERDP 2010). Thus, an efficient model to forecast mobility and burial of munitions on the seabed can improve risk assessment and reduce costs related to management and remediation actions. During the ONR-accelerated research initiative (ARI) 2001–2005 "Mine Burial Prediction" (Bennett 2000), a physical model, called IMPACT35, was developed to predict the trajectory of a mine through air, water, and sediment to forecast the amount of burial that occurs upon impact with the seafloor (Chu 2009; Chu et al. 2004, 2005; Chu and Fan 2007, 2005, 2006). IMPACT35 has six degrees of freedom (DoF). Three degrees of freedom refer to the position of center of mass of the object, and the other three degrees of freedom represent the orientation of the object (roll, yaw, and pitch).

A munition on the seabed is less movable than a sea mine in a water column. Therefore, the existing 6-DoF model (e.g., IMPACT35) for sea mine burial prediction needs modification. Also, the object model requires localized environmental parameters such as waves, currents, and sediment transport in order to accurately predict the location, mobility, and burial of underwater munitions. When wind transmits momentum to the water surface, it may form waves that produce near-seabed orbital motion responsible for

[1] Department of Oceanography, Naval Postgraduate School.

[2] Ocean Sciences Division, U.S. Naval Research Laboratory, Stennis Space Center.

stirred-up sediment and increase the sediment transport. In contrast, wave orbital motion in the company of currents intensifies the bed shear stress and decreases the intensity of the current. Furthermore, the dissipation of wave energy in the surf zone induces currents along and across the shore. All the littoral flows carry a significant quantity of sediments. Recently, an object model was developed to predict a munition's mobility and burial on the sandy seafloor using the observational environmental data (currents, waves, sediment, morphology) as the forcing term (Chu et al. 2022).

An open-source software, Delft3D, has been developed to predict currents, waves, sediment transport, and morphology in estuarine, fluvial, and littoral environments (Deltares 2022a,b; Booij et al. 1999). Delft3D output provides the environmental parameters around the munition, which are required by the 6-DoF model for predicting the munition's burial and mobility. Under the sponsorship of SERDP, experimental (Calantoni et al. 2014; Traykovski and Austin 2017) and analytical (Friedrichs et al. 2016; Rennie et al. 2017) studies focus on the identification of the conditions that determine the onset of a specific and important motion (i.e., roll of the munition around its main axis, both on a hard surface and on a sand bed in the presence of concurrent scour burial). In this study, a coupled Delft3D-object model has been developed to predict hydrodynamic and morphological processes as well as munitions' burial and mobility on the sandy sea floor. The Delft3D model output was taken as the forcing term for the object model (Figure 1).

The coupled system consists of two major components: Delft3D and object model. The object model has five parts: (a) cylindrical object model with the burial percentage Shields parameter (θ_{opb}); (b) sediment scour model with sediment Shields parameter (θ_{sed}); (c) object's physical parameters such as diameter (D), object's relative density versus water density (S_o), mass (M), and rolling moment about its symmetric axis (I_o); (d) environmental variables such as near seabed ocean currents, bottom wave orbital velocity (Ubr), water depth (h), wave peak period (T_P), significant wave height (H_S), and sediment characteristics; and (e) model output such as the burial percentage p_B, and the object's displacement.

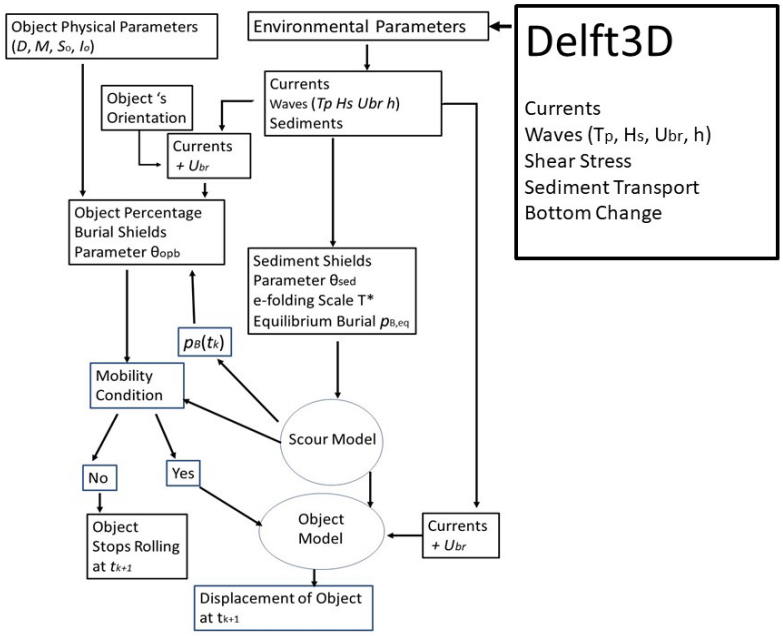

Figure 1. Flow chart of the coupled Delft3D-object model to predict objects' mobility and burial

The Target Reverberation Experiment 2013 (TREX13) in Panama City, Florida from 21 April to 13 May 2013 produced a unique data set containing environmental measurements such as waves, currents, and sediment samples as well as mobility and burial of munitions (Calantoni et al. 2014). The TREX13 data were used to verify the coupled model. The remainder of the paper is outlined as follows. Section B depicts the study area. Section C describes the observational data from TREX13. Sections D–F present the Delft3D, the object mobility model, and the object scour model. Section G presents prediction of the object's mobility and burial by the coupled Delft3D-object model. Section H presents the conclusions. Detailed object modeling information is included in Appendices A–D.

B. STUDY AREA

The study area is off the coast of Panama City near the San Andrew Bay, indicated by the region enclosed by the red lines in Figure 2. The tides are diurnal with the amplitude of highest astronomical tide (HAT) of 8.914 m and a maximum tidal range of 0.4 m (Bunya et al. 2010). The wind has strong seasonal variation: primarily from the

north in winter and fall, and mostly from the south in summer and spring. The hurricane season in the Gulf of Mexico is typically from June to November with the peak occurring in August and September. During the off-hurricane season, the surface winds were not strong during 20 April–13 May 2013 with the east-west component (Figure 3a) and the north-south component (Figure 3b) from the National Oceanic and Atmospheric Administration (NOAA) station PACF1 (nearest to the study area) (NOAA/National Data Buoy Center [NDBC]) and the ERA5 Reanalysis data with 0.25° resolution from the European Centre for Medium-Range Weather Forecasts (ECMWF) (ECMWF 2019). It is noted that, on 5 May 2013, a cold front was over northern Texas and passed over Panama City between 5 and 6 May 2013, causing a storm event and stronger waves. However, in general, the study area during the off-hurricane season represents the low-energy regime (Calantoni et al. 2014).

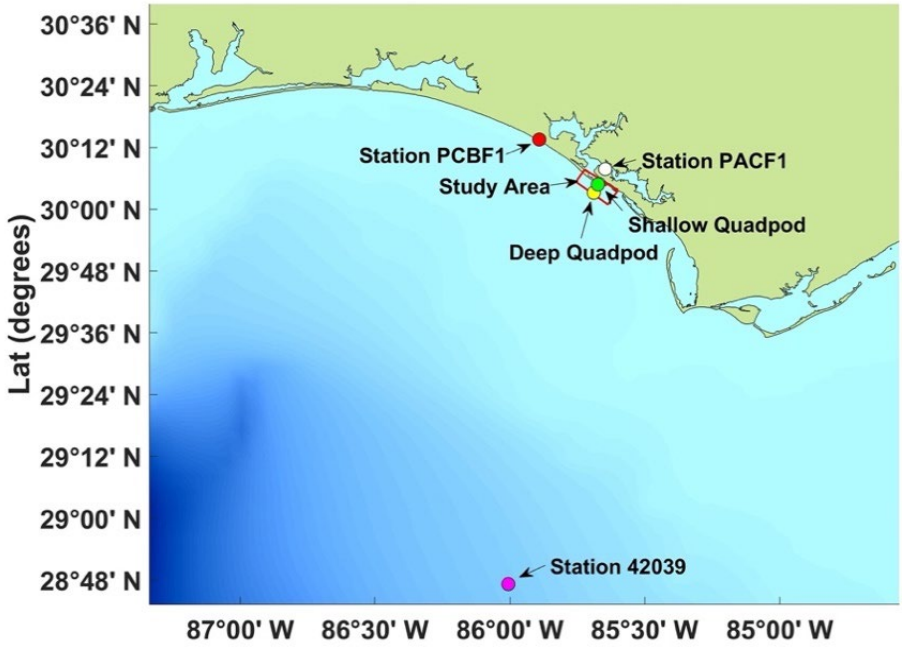

Northern Gulf of Mexico off the coast of Panama City with locations of the shallow quadpod (30° 04.81′ N, 85° 40.41′ W) and deep quadpod (30° 03.02′ N, 85° 41.34′ W) and the NOAA stations PACF1, PCBF1, and 42039. The study area is enclosed by the red lines. The NOAA station PACF1 is nearest to the study area.

Figure 2. Northern Gulf of Mexico off the coast of Panama City

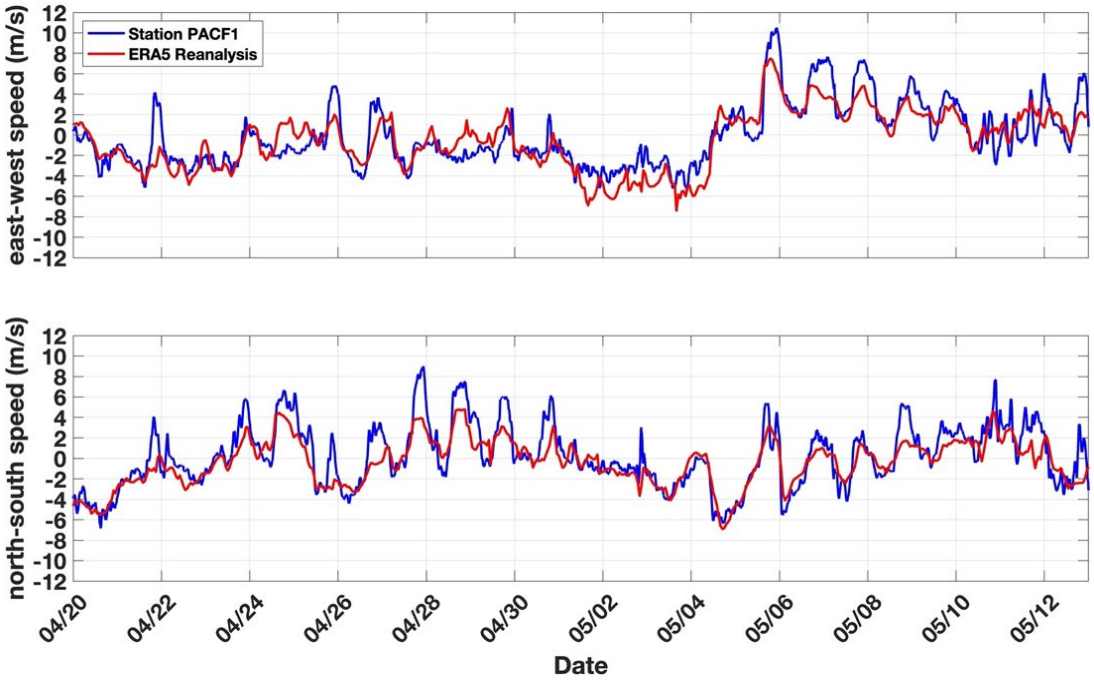

Surface (upper panel) east-west wind component and (lower panel) and north-south wind component for the study area from the NOAA station PACF1 (blue curves) (NOAA/NDBC) and the ERA5 Reanalysis data with 0.25° resolution from the European Centre for Medium-Range Weather Forecasts (ECMWF) (red curves) (ECMWF 2019).

Figure 3. Surface east-west and north-south wind component for the study area

C. TREX13

1. Surrogate Munitions

During TREX13, four types of surrogate and replica munitions were used to roughly represent the 155 mm HE M107, 81 mm mortar, 25 mm cartridge, and 20 mm cartridge and were designed and fabricated using crude drawings and specifications provided by existing Army Technical Manuals (e.g., TM 43–0001-27 and TM 43–0001-28) (Calantoni et al. 2014) (Figure 4). Table 1 shows the complete list of deployed and recovered munitions along with brief descriptions and their physical properties such as bulk density and rolling moment that closely match their real counterparts.

Fabricated surrogate, purchased replica, and fabricated replica of (left) 155 mm HE M107, (middle) 81 mm mortar, and (right) 25mm and 20 mm cartridges.

Figure 4. Fabricated surrogate, purchased replica, and fabricated replica. Adapted from Calantoni et al. (2014).

Table 1. List of surrogate and replica munitions used during TREX13. Adapted from Calantoni et al. (2014).

Type with Diameter	**Labels**	**Materials Type**	**Recovered**	**Rolling Moment** (10^{-4} kg m^2)	**Volume** (10^{-5} m^3)	**Mass** (kg)	**Density** (kg m^{-3})
155 mm, HE, M107	D5, D6	*Delrin, 304 Stainless* Surrogate	D5, D6	923.59	768.38	34.15	4,444
	D3, D4	*Aluminum* Replica	D3, D4	500.48	768.38	20.91	2,721
81 mm mortar	C3, C4	*Delrin, 316 Stainless, Aluminum tail fins* Surrogate	C3, C4	24.73	120.93	3.76	3,109
	C5, C6	*304 Stainless, Aluminum tail fins* Replica	C5, C6	50.51	120.93	8.70	7,194
	C1, C2	*Urethane* Replica		8.34	120.93	1.45	1,199
25 mm cartridge	B5, B6	*Delrin, 316 Stainless* Surrogate	B5, B6	0.46	16.55	0.39	2,356

Type with Diameter	Labels	Materials Type	Recovered	Rolling Moment (10^{-4} kg m^2)	Volume (10^{-5} m^3)	Mass (kg)	Density (kg m^{-3})
20 mm cartridge	B7, B8	*304 Stainless* Replica	B7, B8	1.98	16.55	1.32	7,975
	B3, B4	*Aluminum* Replica	B3, B4	0.68	16.55	0.43	2,598
	B1, B2	*Delrin* Replica		0.35	16.55	0.23	1,390
	A5, A6	*Delrin, 316 Stainless* Surrogate	A6	0.13	7.70	0.20	2,597
	A7, A8	*304 Stainless* Replica	A7	0.53	7.70	0.63	8,181
	A3, A4	*Aluminum* Replica	A3, A4	0.18	7.70	0.19	2,468
	A1, A2	*Delrin* Replica		0.09	7.70	0.11	1,429

A total of 26 objects were deployed and 18 objects were recovered. Type surrogate munitions were fabricated to have rolling moments within 10% of the estimated rolling moment of the real counterpart.

2. Field Experiment

A field experiment was conducted to simultaneously collect both environmental (currents, waves, and sediment samples) data and locations of surrogate/replica munitions on the seafloor from 21 April 2013 to 13 May 2013 at two sites (Calantoni et al. 2014). Instruments were mounted on a pair of large rugged frames (herein referred to as "quadpods") that were deployed at two different water depths (herein referred to as "deep" and "shallow"). The quadpods were deployed in the northern Gulf of Mexico offshore of Panama City Beach, Florida USA (Figure 5a). The deep quadpod was deployed at 30° 03.02330 N, 85° 41.33630 W, in about 20 m water depth, while the shallow quadpod was deployed at 30° 04.80994 N, 85° 40.41064 W, in about 7.5 m water depth. A sector scanning sonar was mounted on one of the legs of each of the quadpods, scanning a 110° swath every 12 minutes.

The data captured by TREX13 were during the time when hurricanes are least expected to occur. Therefore, the environmental conditions during hurricanes are ignored. It implies the hypothesis that the munitions' mobility will not be influenced by hurricane-generated waves and currents. This is because in shallow-water depths of 10–20 m, extreme significant wave heights resulting from hurricanes will cause large near-bed-orbital velocities leading to rapid scouring and burial, and in turn stopping the munitions' mobility.

The divers' performance confirmed this hypothesis. Divers laid four surrogate munitions and nine replica munitions on the seafloor near each of the shallow and deep quadpods within the view field of the sector scanning sonar on 21 April 2013 (Figure 5b). The location and orientation of surrogate and replica munitions were detected by the sector scanning sonar and maintenance diver with video camera. Only objects laid by divers under the shallow quadpod was photographed (Figure 5c). The field of view of the sector scanning sonar is roughly represented by the light blue. The locations of the surrogates are denoted by the dark blue circle in the upper left. The other replicas were grouped according to relative bulk density. In this case the red boxes denote the objects that were not recovered from the shallow quadpod site. Thus, the initial surrogate munitions' location and orientation provided from the TREX13 are only for the shallow quadpod. Immediately after the storm event on 5–6 May 2013, a maintenance dive performed in the morning of 8 May 2013 found that the surrogates and replicas may have been buried in place as opposed to being transported away by the waves and currents. Excavating by hands, divers were able to recover a total of eight munitions buried just below the surface very near the known initial locations at the shallow quadpod. The observational period for the munitions' location and burial was 21 April–7 May 2013.

3. Data

As described in Calantoni et al. (2014), the combination of the munitions' mobility and the driving environmental conditions was observed. Waves and currents were obtained using both an acoustic surface tracking (Nortek AWAC) and pressure time

series. Two sediment cores were collected at the shallow quadpod location during the deployment (core# D1) and retrieval (core # R1). It was found that both cores contained nearly 100% sand (Table 2). Therefore, the Shield's parameter can be used for identifying mobility of sediments. Grain size distributions were obtained with standard sieve techniques and results for porosity, bulk density, and void ratio were obtained by measuring the weight loss or water weight. The median grain diameter (d_{50}) is around 0.23 mm and the sediment density (ρ_s) is about 2.69×10^3 kg m^{-3}. These two parameters are most significant to influence sediment mobility and are needed for the object scour burial model (see Section F).

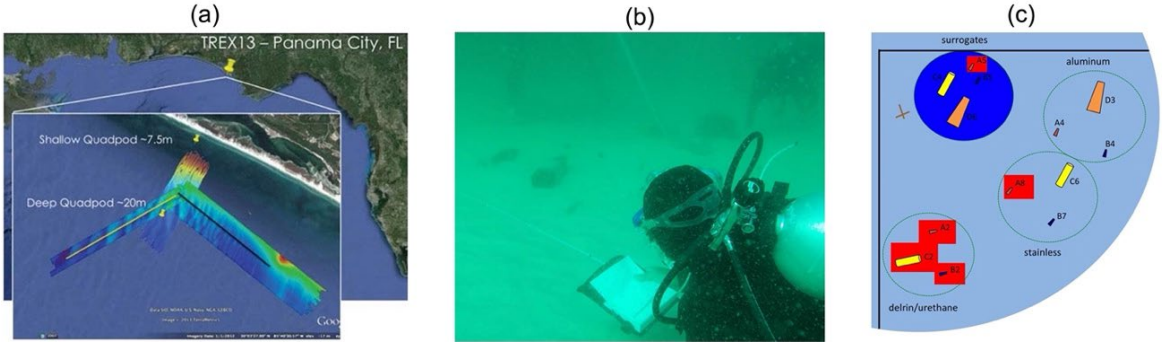

(a) Locations of deep and shallow quadpods, (b) the photo of divers laying the object field during the shallow quadpod deployment, and (c) layout of objects laid by divers under the shallow quadpod.

Figure 5. Layout of objects laid by divers under the shallow quadpod. Adapted from Calantoni et al. (2014).

Table 2. Sediment properties. Adapted from Calantoni et al. (2014).

Depth Range (cm)	% **Gravel**		% **Sand**		**Mean** Phi-Value		**Standard Deviation** Phi-Value		% **Porosity**		**Bulk Density** (g/cc)		**Void Ratio** (e)	
Core #	D1	R1	D1	R1	D1	R1	D1	R1	D1	R1	D1	R1	D1	R1
0–2	0.00	0.04	100.00	99.96	2.14	2.06	0.39	0.40	38.35	39.55	2.04	2.02	0.62	0.65
2–4	0.00	0.00	100.00	100.00	2.12	2.04	0.40	0.40	39.28	40.14	2.03	2.02	0.65	0.67
4–6	0.00	0.02	100.00	99.98	2.13	2.08	0.42	0.46	39.13	38.96	2.03	2.03	0.64	0.64
6–8	0.02	0.01	99.98	99.99	2.23	2.21	0.43	0.44	38.84	39.46	2.04	2.03	0.63	0.65
8–10	0.13	0.01	99.87	99.99	1.94	2.24	0.62	0.40	37.62	39.26	2.06	2.03	0.60	0.65

Sediment properties from diver push cores taken during the deployment (D1) and the retrieval (R1) of the instrumentation at the shallow quadpod location.

D. DELFT3D

1. Model Description

The open-source Delft3D version 4.04.01 was implemented in the TREX13 area to predict currents and waves. Under the wind and tidal forcing, the flow module (Deltares 2022a) predicts the water level and currents, feeds the current data into the wave and morphology modules as input, computes the sediment transport, and updates the bathymetry. The wave module (Deltares 2022b) is used to predict the wave generation, propagation, dissipation, and non-linear wave-wave interactions in the nearshore environment with the inputs such as water level, bathymetry, wind, and currents from the flow module. The wave module uses Simulating Waves Nearshore (SWAN), which is a third-generation model derived from the Eulerian wave action balance equation (Booij et al. 1999). Since we are only interested in the wave parameters such as the peak period (T_P), significant wave height (H_S), and bottom wave orbital velocity (*Ubr*), with the temporal resolution of 1 h for the object model, the coupling time between the flow and wave modules is also set to 1 h. The morphology module works in an integrated way with the wave and flow modules in a cycle. This system is a process-based model that considers the impact of waves, currents, and sediment transport on morphological changes.

2. Model Grids and Time Steps

Two grids with different grid cell sizes were nested (Figure 6) to create a region with finer resolution. These rectangular grids compose the flow domain. The flow outer grid (coarser resolution) is composed by 137×75 grid points with spacing of 50 m in both longshore and cross-shore directions. The flow inner grid (finer resolution) grid has 20 m resolution and was divided into 139×124 grid points equally spaced. The sediment transport and morphological evolution were computed only in the flow inner grid. The wave domain (Figure 6) is defined in order to avoid the boundary effect and allow the use of deep quadpod data to set up the wave boundary conditions. The wave grid is composed of 273×111 grid points with 50 m resolution. The bathymetric data (Figure 6) was from the Northern Gulf Coast Digital Elevation Model from the National Oceanic and

Atmospheric Administration/National Geophysical Data Center (NOAA/NGDC) (NOAA/NGDC 2010). The resolution of this data set varies between 1/3 arc-second and 1 arc-second (around 10 and 30 m). The time step is set as 12 seconds for the coarse domain (grid size 50 m) and 6 seconds for the finer domain (grid size 20 m). The small time-steps (12 s, 6 s) are needed in order to satisfy the Courant-Friedrichs-Lewy (CFL) condition of computational stability for the Delft3D flow module.

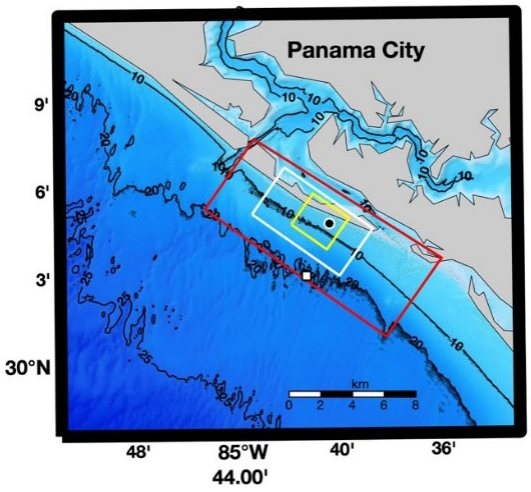

Study area with bathymetry, depth contours (10 m, 20 m, and 25 m), and computational grids for wave module (red), flow module with coarse resolution (white), and flow module with fine resolution (yellow). The black dot represents the shallow quadpod location, and the white square denotes the deep quadpod location.

Figure 6. Study area with bathymetry

3. Wind and Tidal Forcing

The wind input files were set up using the ERA5 Reanalysis data from ECMWF, with 0.25° resolution (ECMWF 2019) for the flow and wave modules. The Global Inverse Tide Model TPXO 8.0 with 1/45-degree resolution was used to create the boundary conditions for the flow module. For the alongshore boundary, the water level with astronomic forcing was imposed. The water level gradient (a so-called Neumann boundary condition) was chosen with a constant zero water level slope in the longshore

direction for both across-shore open boundaries. It allows for flow to leave and enter the lateral boundaries with no spurious circulation.

4. Initial and Boundary Conditions

As an initial condition, the water level and current velocity were set to zero. Additionally, the sediment transport boundary conditions were set by specifying the inflow concentration as zero kg/m^3. The initial condition for the sand sediment was set as a uniform zero concentration, and the initial bed of sediment was set to 5 m. Wave boundary conditions were set based on the measurements from the deep quadpod location using the significant wave height, wave period, wave directions, and directional spreading. These parameters were applied uniformly on the three open boundaries. The spin-up interval of 720 minutes was established to prevent any influence of a possible initial hydrodynamic instability on the bottom change calculation, which starts only after the spin-up interval. The sediment type was set as sand with a sediment-specific density of 2,650 kg/m^3.

The calibration was conducted to adjust the parameters to the best agreement between the modeled and observed water level, waves, and currents. For water level, calibration was through minimizing the difference in amplitude and phase between predicted and measured tides. For waves, the calibration was to determine the optimal Joint North Sea Wave Project (JONSWAP) bottom friction coefficient and wave height to water depth ratio. For currents, the calibration was to identify the best Chézy bottom roughness, horizontal eddy viscosity, and diffusivity. The calibration period was set up as 21–27 April 2013, which correspond to 27% of the entire period of observations (21 April–13 May). During this process, parameters were adjusted separately. While one was fine-tuned, the others remained constant. The calibrated JONSWAP bottom friction coefficient was 0.067 m^2/s^3 and wave height to water depth ratio was 0.7 for the wave module, the Chézy bottom roughness was 65 $m^{1/2}/s$, horizontal eddy viscosity was 0.5 m^2/s, and horizontal diffusivity was 10 m^2/s for the flow module.

5. Model Output

The Delft3D output data with 1-hour resolution are used as input to the object model. The output from the flow module includes the water depth (h) and the current velocity, $\boldsymbol{U}_c = \boldsymbol{i}v_e + \boldsymbol{j}v_n$, with ($\boldsymbol{i}$, $\boldsymbol{j}$) the unit vectors in longitudinal and latitudinal directions, and $U_c = (v_e^2+v_n^2)^{1/2}$ the current speed. The output from the wave module includes the wave peak-period (T_P), significant wave height (H_S), wave direction, and bottom wave orbital velocity (U_{br}). The bottom water velocity vector of combined current and waves is represented by $\boldsymbol{V}_w$ with $|\boldsymbol{V}_w| = U_c + U_{br}$ and the orientation, $\psi = \tan^{-1}(v_n/v_e)$. Figure 7 shows the time series of the environmental parameters [v_e, v_n, h, T_P, H_S, U_{br}] predicted by the Delft3D (red curve) and observed by the AWAC (black curve). The AWAC only provides the observed data for [v_e, v_n, h, T_P, H_S], but not the bottom orbital velocity U_{br}, which was calculated using a well-established linear wave model with MATLAB function (Wiberg and Sherwood 2008) with the observed water depth (h), significant wave height (H_S), and peak period (T_P) (see Appendix D in Wiberg and Sherwood [2008]).

Since the munitions were found totally buried without mobility in the morning of 8 May 2013 by the divers in the TREX13 and the TREX13 provides the munitions' mobility information from 21 April to 7 May 2013, the integration period for the coupled Delft3D-object model was set as 21 April–7 May 2013. The root-mean-square error (RMSE) between the Delft3D output and the TREX13 observations is 0.105 m for the water level, 0.111 m/s for the east-west current speed, 0.0641 m/s for the north-south current speed, 0.0946 m for the significant wave height, and 0.0928 m/s for the bottom wave orbital velocity. The Bias between the Delft3D output and the TREX13 observations is -0.0244 m for the water level, -0.0367 m/s for the east-west current speed, 0.0055 m/s for the north-south current speed, 0.0429 m for the significant wave height, and -0.0786 m/s for the bottom wave orbital velocity. The correlation coefficient between the Delft3D output and the TREX13 observations is high as 0.966 for the significant wave height and 0.941 for the bottom wave orbital velocity; reasonably high as 0.796 for the water depth, 0.571 for the north-south current speed, and 0.551 for the east-west current speed; and the lowest as 0.373 for the peak wave period. The performance of the

Delft3D modeling is reasonably good according to the criteria presented in (van Rijn et al. 2003).

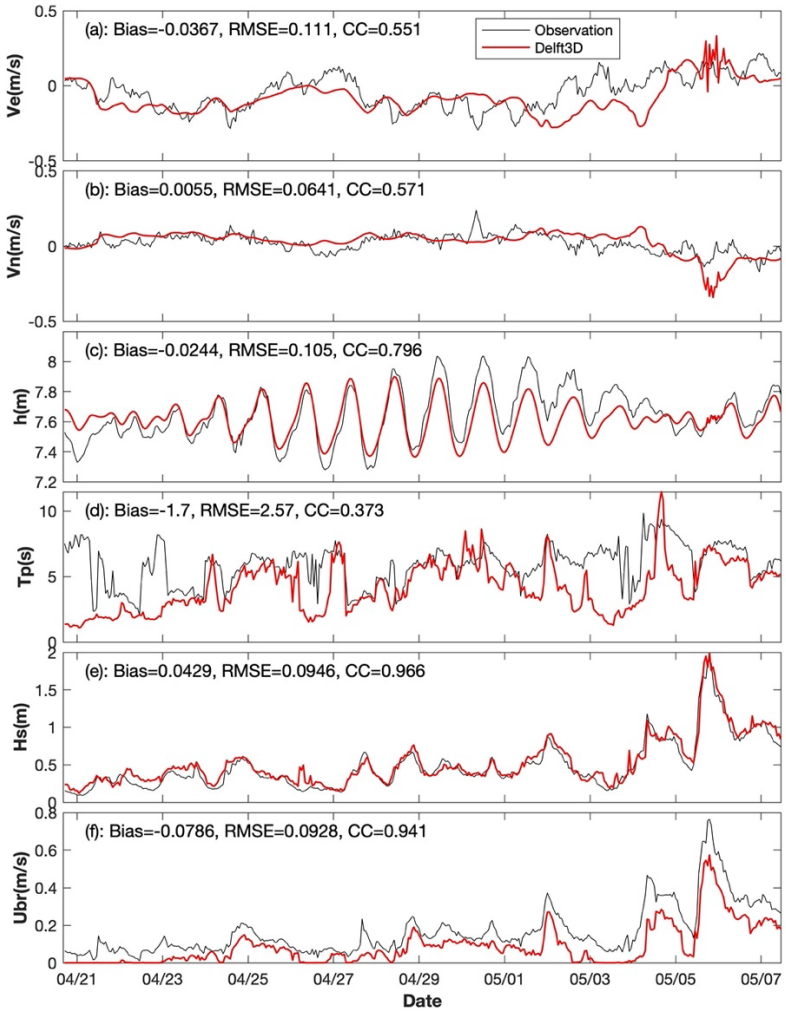

Comparison of Delft3D predicted (red) and observed during the TREX13 (black) at the shallow quadpod from 21 April to 7 May 2013: (a) near bed (~0.15 m) longitudinal current v_e (m/s), (b) near bed (~0.15 m) latitudinal current v_n (m/s), (c) water depth h (m), (d) peak period T_P (s), (e) significant wave height H_S (m), and (f) computed bottom wave orbital velocity U_{br} (m/s).

Figure 7. Time series of the environmental parameters

E. OBJECT MOBILITY MODEL

Consider a cylindrical object with length L and diameter D buried in the seabed with the burial depth B ($B < D/2$). Let the water velocity (consisting current and waves) near the seabed ($\boldsymbol{V}_w$) be in the direction towards the cylinder with an angle, ϕ, perpendicular to main axis of the cylinder, and be decomposed into $\boldsymbol{V}_w = (U, V)$ with U the perpendicular component, and V the parallel component (Figure 8) to the main axis of the cylinder. As the object rolls with angular velocity ω on seabed with the object's burial let the axis of rotation inside the sediment be at depth b ($b < B$) (see Appendix A).

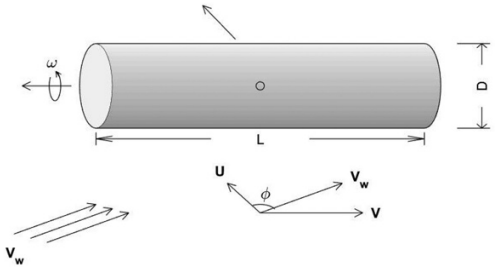

Roll of a cylindrical object on the seafloor with large aspect ratio forced by the combination of ocean currents and bottom wave orbital velocity. Here, ($\pi/2$-ϕ) is the angle between $\boldsymbol{V}_w$ and the main axis of the cylinder.

Figure 8. Roll of a cylindrical object on the seafloor

As an object rolls around the point b (see Figure 50 in Appendix A) with an angular velocity ω, the translation velocity of the object is given by

$$u_o = \omega\left(\frac{D}{2} - b\right) . \tag{1}$$

The corresponding moment of momentum equation of the rolling object is given by [see equation (A17) in Appendix B]

$$\begin{cases} I_A^* \dfrac{d\omega}{dt} = T_F - \Pi(\rho_o - \rho_w)\sqrt{b(D-b)} & \text{if} \quad p_B < 0.5, \quad \theta_{opb} > 1 \\ \omega = 0, \quad \text{otherwise} \end{cases}, \tag{2}$$

where $I_A^* = I_o + (\rho_o \Pi D^2/4) + (D/2 - b)\rho_w \Pi(D/2 + B/2 - b)$; I_o is the rolling moment of the munition about the symmetric axis of the munition (see Figure 51); T_F is the forward

torque caused by the drag force (F_d) and lift force (F_l) (see Appendix C); $p_B = B/D$, is the percentage burial, and θ_{opb} is the object mobility parameter for percentage burial (see Appendix B); (ρ_o, ρ_w) are densities of object and water; Π is the volume of the munition.

Let the relative horizontal velocity of the rolling object be defined by

$$\hat{u}_o = \frac{u_o}{U} \quad . \tag{3}$$

Substitution of (1) into (2) and use of (3) leads to a special Riccati equation,

$$\begin{cases} \dfrac{d(1-\hat{u}_o)}{dt} + \alpha(1-\hat{u}_o)^2 = \beta \quad \text{if} \quad p_B < 0.5, \quad \theta_{opb}(t) > 1 \\ \hat{u}_o = 0, \quad \text{otherwise} \end{cases}, \tag{4}$$

where

$$\begin{aligned} \alpha &= \frac{(1-2p_b)}{8I_A^*}\rho_w C_d |U| D^3 L\left[(1-p_B)(1+p_B-2p_b)+2\gamma\sqrt{p_b(1-p_b)}\right] > 0 \\ \beta &= \frac{(1-2p_b)}{2I_A^*|U|} g\rho_w \Pi(S_o-1)D^2\sqrt{p_b(1-p_b)} > 0 \end{aligned} \quad . \tag{5}$$

The special Riccati equation (4) has an analytical solution from integration from tk to tk+1 (k = 0, 1, 2,…, K-1) (Kamke 1977)

$$\hat{u}_o(t) = \begin{cases} 1 - \dfrac{[1-\hat{u}_o(t_k)]\sqrt{\alpha_k\beta_k} + \beta_k \tanh\left[(\sqrt{\alpha_k\beta_k})(t-t_k)\right]}{\sqrt{\alpha_k\beta_k} + \alpha_k[1-\hat{u}_o(t_k)]\tanh\left[(\sqrt{\alpha_k\beta_k})(t-t_k)\right]}, \text{ for } p_B(t_k) < 0.5, \theta_{opb}(t_k) > 1 \\ 0, \text{ for } p_B(t_k) \geq 0.5, \theta_{opb}(t_k) \leq 1, t_k < t \leq t_{k+1}, \alpha_k = \alpha(t_k), \beta_k = \beta(t_k) \end{cases} \tag{6}$$

with α_k and β_k as known constants during the integration. Substitution of (6) into (3) leads to the dimensional horizontal velocity of the rolling object, $u_o(t) = U\hat{u}_o(t)$, which should be used for each time interval Δt. The solution (6) depends on (α_k, β_k), which involve three types of parameters: (a) time-independent physical parameters of the object for S_o, Π, L, and D; (b) time-dependent water velocity, $U(t_k)$, from Delft3D model output; (c) time-dependent relative depth of sediment rolling axis [$p_b(t_k)$], and burial percentage [$p_B(t_k)$] determined using a scour burial model. Let l be the displacement of object

$$dl/dt = u_o \tag{7}$$

Integration of l with respect to time t leads to the munition's displacement.

F. OBJECT SCOUR MODEL

Existing studies on scour burial were all concentrated on motionless objects. The ratio between the fluid force (bottom shear stress) and the weight of the sediment particles; that is, sediment Shields parameter (θ_{sed})

$$\theta_{sed} = \frac{f U_{br}^2}{g(S_{sed}-1)d_{50}}, \quad S_{sed} = \frac{\rho_s}{\rho_w}, \quad f = \exp\left[5.5\left(\frac{6U_{br}T_P}{\pi d_{50}}\right)^{-0.2} - 6.3\right], \tag{8}$$

is crucial for scour burial of motionless object and in turn for prediction of the percentage burial parameter $p_B(t) = B/D$ (Friedrichs et al. 2016; Rennie et al. 2017). Here, f is the wave friction factor (Nielsen 1992), ρ_s the sediment grain density, and d_{50} the medium sand grain size. Using the wave data (T_P, U_{br}) from Figures 6e and 6g, and sediment parameters (ρ_s= 2.69×10^3 kg/m^3, d_{50}=0.23×10^{-3} m) from the TREX13 (Calantoni et al. 2014; Chu et al. 2022), the sediment Shields parameter (θ_{sed}) is calculated from 21 April to 7 May 2013. It is less than 0.1 all the time except for when an atmospheric cold front passed by on 05–06 May 2013. The maximum value of θ_{sed} reached 0.33 (Figure 9).

As pointed out in Nielsen (1992), the equilibrium percentage burial $p_{B,eq}$ for motionless cylinders induced by scour tends to increase as θ_{sed} increases. An empirical formula has been established,

$$p_{B,eq} = a_1\theta_{sed}^{a_2} - a_3, \tag{9}$$

with different choices of the coefficients (a_1, a_2, a_3) determined experimentally for cylinders subject to steady currents: a_1 = 11, a_2 = 0.5, a_3 = 1.73 (Whitehouse 1997), a_1 = 0.7, a_2 = a_3 = 0 (Sumer et al. 2001), a_1 = 2, a_2 = 0.8, a_3 = 0 (Demir and García 2007), and for cylinders under waves (depending on wave period): a_1 = 1.6, a_2 = 0.85, a_3 = 0 for Tp longer than 4 seconds (Cataño-Lopera et al. 2007). For motionless cylinders before scour burial reaching equilibrium the percentage burial follows an exponential relationship (Whitehouse 1997)

$$p_B(t_k) = p_{B,eq}\left[1 - \exp\left(-\frac{t_k}{T^*}\right)\right], \tag{10}$$

where the e-folding time scale T* is given by

$$T^* = \frac{c_1 \theta_{sed}^{c_2} D^2}{\left[g(S_{sed} - 1) d_{50}^3 \right]^{0.5}}, \quad c_1 = 1.5, \quad c_2 = 0.11. \tag{11}$$

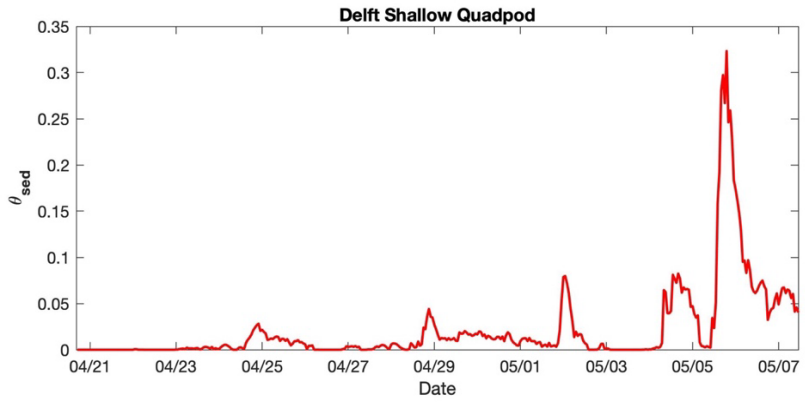

Figure 9. Time series of sediment Shields parameter (θ_{sed}) at the shallow quadpod computed from the Delft3D model output

With the bottom wave orbital velocity (U_{br}), sediment density (ρ_s), medium grain size (d_{50}), and in turn the sediment Shields parameter (θ_{sed}), the equilibrium object percentage burial ($p_{B,eq}$) is calculated using (9) with coefficients a_1 = 1.6, a_2 = 0.85, a_3 = 0. The sediment supporting depth b (or p_b) is calculated from burial depth B (or p_B) using (10), such that

$$b(t_k) = \lambda B(t_k), \quad p_b(t_k) = b(t_k) / D = \lambda p_B(t_k), \quad \lambda = 0.453 \tag{12}$$

It is noted that the predicted burial percentage (p_B) computed from (10) represents the depth that an object on the surface would bury to at that moment. An object deployed at the beginning of the time sequence would, however, always remain buried at the deepest burial it has reached so far. The burial depth of the base of the object below the ambient seabed is equivalent to the greatest depth that the scour pit has reached up to that point in time (Trembanis et al. 2007). In other words, scour only acts to bury an object deeper. It can never unbury (re-exposure) as the time series suggested by (10). Similar to Trembanis et al. (2007), a simple parameterization was proposed by Chu et al. (2022) to represent the re-exposure process starting from k (= 1, 2, …): (a) doing nothing if $p_B(t_{k+1}) \geq p_B(t_k)$, (b) computing the weighted average

$$\tilde{p}_B(t_{k+1}) = w p_B(t_k) + (1-w) p_B(t_{k+1}) \quad \text{if } p_B(t_{k+1}) < p_B(t_k) \tag{13}$$

with w the weight coefficient. In this study, we take w = 0.80. The object mobility and burial model consists of equations (6)–(13).

G. PREDICTION OF OBJECT'S MOBILITY AND BURIAL

The munitions' mobility and burial were predicted using the object mobility and burial models with the environmental variables predicted by the Delft3D (Figure 1) as the forcing term. The model was integrated for each surrogate (or replica) munition deployed in the shallow quadpod with its initial location and orientation (Figure 5c) from 12:40 local time on 20 April 2013. The angle between $\boldsymbol{V}_w$ (data represented by the red curves in panels a, b in Figure 7) and the direction perpendicular to cylinder's main axis is determined. The velocity vector of combined current and waves ($\boldsymbol{V}_w$) is then transformed into $\boldsymbol{V}_w = (U, V)$, with U the perpendicular component and V the paralleling component. The component U is used in the model. The object's physical parameters such as the diameter (D), volume, mass (M), and density (ρ_o) are obtained from Table 1.

The environmental data such as the water depth (h), wave peak period (T_P), significant wave height (H_S), bottom wave orbital velocity (U_{br}) (represented by the red curves in Figure 7), and sediment data (100% sand, d_{50} = 0.23 mm, $\rho_s = 2.69\times10^3$ kg m^{-3}) are used by the sediment scour model, demonstrated in equations (8)–(13), to get the burial percentage $p_B(t_k)$, and in turn the relative rolling center depth $p_b(t_k)$. With an object's physical parameters (D, ρ_o, M), the calculated $p_b(t_k)$, model-predicted bottom current velocity component perpendicular to the object's main axis $U(t_k)$, and coefficients [$\alpha(t_k)$, $\beta(t_k)$] for the object mobility model, demonstrated in Equation (5), the object's displacement at the next time step $l(t_{k+1})$ can be predicted using (7).

Based on the known initial locations of the objects at the shallow quadpod (Figure 5c), the model predicts the object's burial percentage [$p_B(t_k)$] shown in Figure 10, the objects' mobility parameter for percentage burial [$\theta_{opb}(t_k)$] shown in Figure 11, and the object's displacement [$l(t_k)$] shown in Figure 12. The burial percentages p_B for all the objects were less than 0.5 except during the storm event on 12:00 5 May to 00:00 6 May

2013 local time (Figure 10). The red color in Figure 11 shows that the object's rolling condition [θ_{opb}>1] is satisfied.

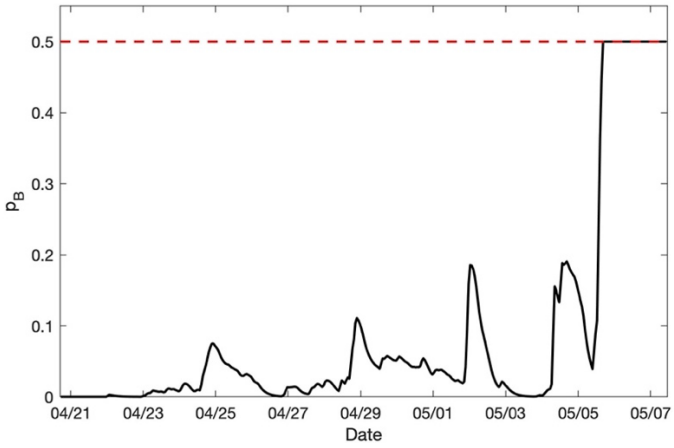

Model predicted burial percentage $p_B(t)$ with re-exposure parameterization for each object at the shallow quadpod from 20 April to 7 May 2013. The predicted burial percentage $p_B(t)$ is less than 0.5 for all the munitions during the whole time period except during the storm event from 12:00 5 May to 00:00 6 May 2013. The burial percentage $p_B(t)$ is the same for each object since it only depends on the sediment characteristics [see equations (9)–(11)].

Figure 10. Model predicted burial percentage $p_B(t)$

The surrogate and replica munitions' mobility and burial were observed by divers and sector scanning sonar images during the field experiment depicted in Section B and in Calantoni et al. (2014). A total of 8 munitions in place at the shallow quadpod location were recovered by divers during the maintenance dive performed on 8 May 2013 (Figure 5b). Note that the munitions excavated by the divers at the shallow quadpod location on 8 May 2013 were immediately redeployed for the duration of the experiment. An overview of the observed munitions' mobility throughout the whole TREX13 experiment (20 April to 07 May 2013) is shown in Figure 13a, and during the storm event on 13:00–20:00 5 May 2013 in Figure 13b. The objects A2 and C2 were immediately mobile and transported out of the field of view because they were last seen on 23 April 2013 (very crude observational information), however, the other objects were almost not mobile (Figure 13a). The predicted large displacements of 20.7 m of A2 from

12:00 21 April to 12:00 24 April 2013 and 6.52 m for C2 from 12:00 21 April to 00:00 23 April 2013 (Figure 12) qualitatively agree with the crude observational information about A2 and C2.

Furthermore, overview of the modeled objects' mobility throughout the whole TREX13 experiment (20 April to 07 May 2013) is shown in Figure 13c and during the storm event on 13:00–20:00 5 May 2013 in Figure 13d. Similarity between the observation (Figures 13a, b) and the model prediction (Figures 13 c, d) shows model capability. However, the model-data discrepancy exists. For example, yaw of munitions D3 and D6 was observed (Figures 11a, b) but not predicted (Figures 11c, d). The munition D3 (rightmost triangles in Figures 11 a, b) moved, but the model predicted a value of l = 0 m by predicting that D3 never moved (Figures 10, 11c, d). The model limitation is due to the four assumptions such as (a) cylinder with large aspect ratio ($L \gg D$), (b) no yaw and pitch, (c) percentage burial depth less than 0.5, and (d) flat seabed. Even if the bottom profile is flat when the object is deployed, the sand tends to accumulate in front of the object and to be eroded on the opposite side thus creating a wavy bed that affects the dynamics of the object. The model will lose capability in the real world if the shape of munition is evidently different from the cylinder with $L \gg D$ and the effect of wavy seabed is large on the dynamics of the object.

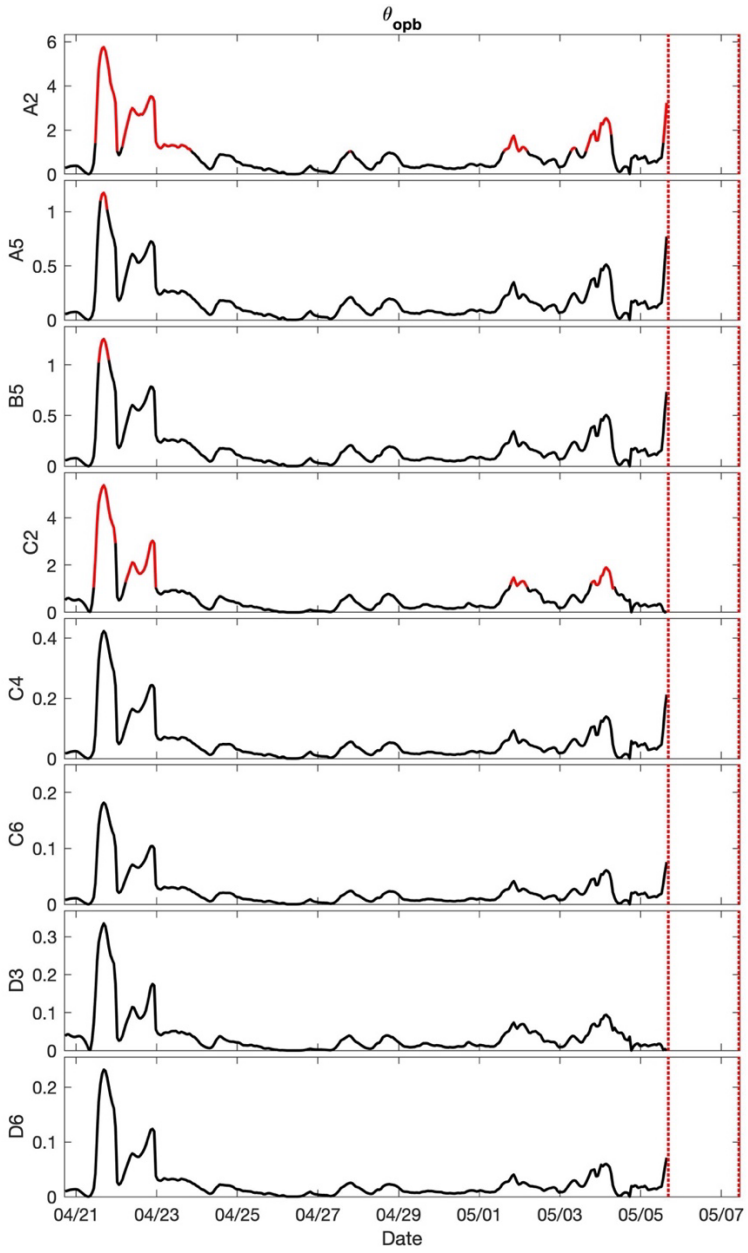

Model predicted objects' mobility parameters for percentage burial (θ_{opb}) at the shallow quadpod from 20 April to 7 May 2013. The red color shows that the condition for rolling the object (θ_{opb}>1) is satisfied. The parameter θ_{opb} is not computed between 12:00 5 May to 00:00 6 May 2013 since the predicted burial percentage $p_B(t)$ is larger than 0.5. Among the eight objects, only A2 and C2 have evident time periods that the condition for rolling the object (θ_{opb} >1) is satisfied.

Figure 11. Model predicted objects' mobility parameters for percentage burial (θ_{opb})

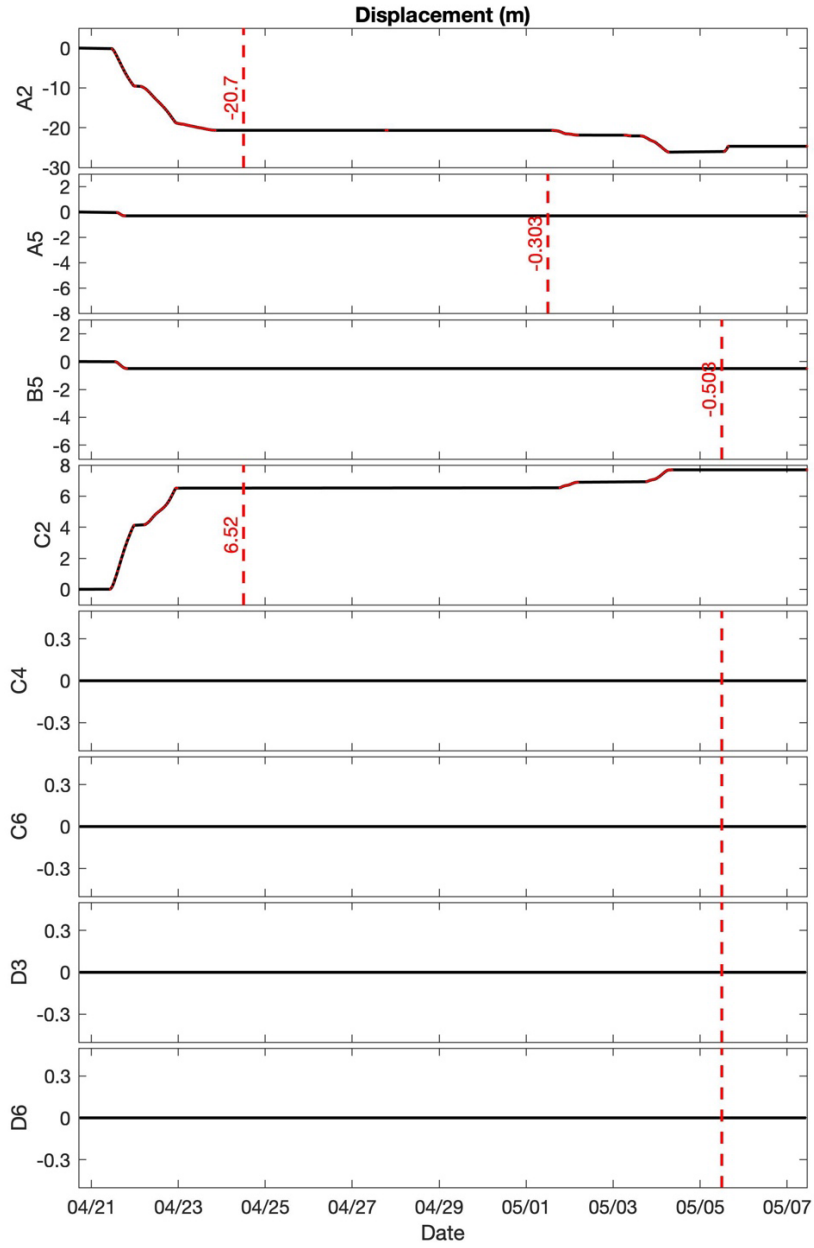

Model predicted displacement $l(t)$ for each object at the shallow quadpod from 20 April to 7 May 2013. Among the eight objects, only A2 and C2 were immediately mobile and displaced 20.7 m (A2) and 6.52 m (C2) on 12:00 24 April 2013 (dashed line); other munitions A5, B5, C4, C6, D3, D6 were completely motionless. According to the TREX13 report (Calantoni et al. 2014), the objects A2 and C2 were immediately mobile and transported out of the field of view because they were last seen on 23 April 2013. After 23 April 2013, their locations were never observed.

Figure 12. Model predicted displacement $l(t)$ for each object

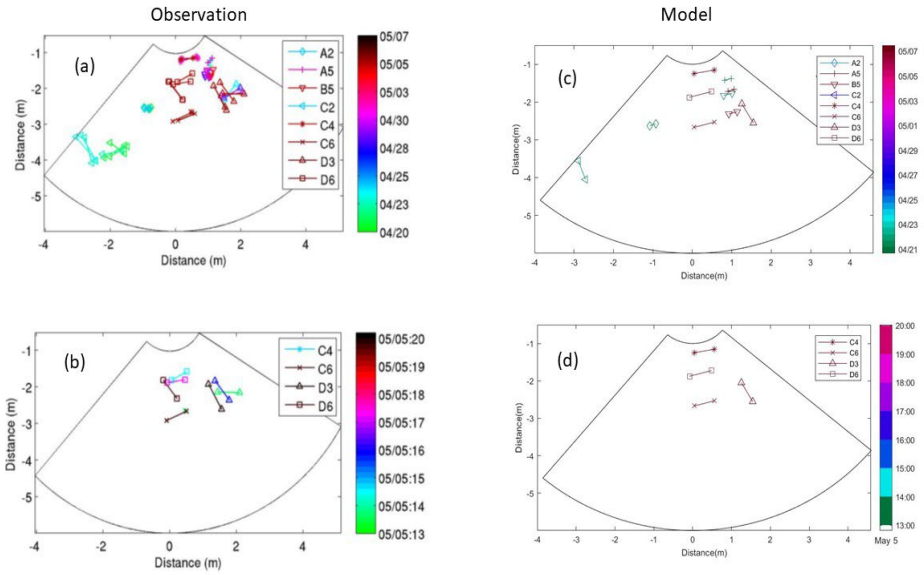

Positions for all visible objects at the shallow quadpod location up to the maintenance dive performed on 8 May are illustrated. (a) Observation for 20 April–07 May 2013, (b) observation for 13:00–20:00 on 5 May 2013, (c) model prediction for 20 April–07 May 2013, and (d) model prediction for 13:00–20:00 on 5 May 2013 are illustrated. The color bars denote the last time when each object was visible with dates for (a, b) and hour on 5 May for (c, d).

Figure 13. Positions for all visible objects at the shallow quadpod location. Panels (a) and (b) are adapted from Calantoni et al. (2014).

H. CONCLUSIONS

1. A coupled Delft3D-object model was recently developed to predict underwater cylindrical objects' mobility and burial in sandy bed. The roll of the object is the major dynamic of this model, with a new concept of its rolling center in the sediment. The object's displacement caused by rolling satisfies the Riccati equation with analytical solution. Along with the dynamical model, the empirical scour model with re-exposure parameterization is used as part of the prediction system.

2. Data collected at the shallow quadpod during TREX13 (21 April to 23 May 2013) off the coast of Panama City, Florida were used as model verification. The environmental data such as bottom currents, water depth

(h), peak period (T_P), and significant wave height (H_S) are used to verify the Delft3D model. The objects' positions tracked by the sector scanning sonar images and the maintenance divers are used to verify the object's mobility and burial model.

3. The model predicted objects' positions agree qualitatively well with the observed surrogates (or replicas) data. The observation shows that the objects A2 and C2 were immediately mobile and transported out of the field of view because they were last seen on 23 April 2013. The other objects were almost not mobile. The objects with large mobility are A2 (displaced 20.7 m from 12:00 21 April to 12:00 24 April 2013) and C2 (displaced 6.52 m for C2 from 12:00 21 April to 00:00 23 April 2013). A2 is a 20 mm cartridge with a mass of 0.11 kg and density of 1,429 kg m^{-3}. C2 is an 81 mm mortar with a mass of 1.45 kg and density of 1.199 kg m^{-3} (see Table 1). The other objects with almost no mobility are A5 (density of 2,597 kg m^{-3}), B5 (density of 2,356 kg m^{-3}), C4 (density of 3,109 kg m^{-3}), C6 (density of 7,194 kg m^{-3}), D3 (density of 2,721 kg m^{-3}), and D6 (density of 4,444 kg m^{-3}). The larger the object's density, the smaller the object's mobility parameter for percentage burial [see Equation (A14)]. However, it is noted that the observational objects' data are quite crude and not sufficient to accurately verify the model prediction on an object's mobility and burial.

4. Although the coupled Delft3D-object model has the capability to predict the object's mobility, the model has its own weaknesses, such as for cylindrical objects. Also, it only considers the roll of the cylinder around its major axis. The object model ignores pitch and yaw. In addition, the seabed is assumed to be flat. It is necessary to extend the object modeling to more realistic seabed environments and object shapes and more complete motion for operational use.

Sediment accretion in a lower-energetic location during two consecutive cold fronts

This chapter was previously published by *Journal of Operational Oceanography* (Pessanha et al. 2022). Co-authors include Vinícius S. Pessanha[3], Peter C. Chu,[3] and Matt K. Gough[3].

I. INTRODUCTION

Waves and currents drive sediment transport, leading to the seafloor evolution through sediment accretion and erosion (Roelvink and Reniers 2012). Field observations have demonstrated that high-energy storm waves can produce offshore sediment transport (Komar 1998) and erode the coastline while wave-induced undertow currents carry sediment in the offshore direction and form sand bars (van Rijn 2013). These morphological effects can be accentuated during consecutive storms when the interval between storms is shorter than the beach recovery period for a single storm (Morton et al. 1995; Callaghan et al. 2008). In the initial storm phase, rapid erosion near the beach and nearshore bar are expected, along with gradual surf zone sediment redistribution (Vousdoukas et al. 2012). The second storm produces more extensive seafloor changes, taking advantage of the destabilizing effect of the first storm on the seafloor that does not have enough time to recover (Lee et al. 1998).

Accurate prediction of erosion and sediment accretion can reduce the costs of environmental remediation efforts aimed at recovering underwater munitions, although it is very challenging. The U.S. Army Corps of Engineers, Navy, and Marine Corps have identified more than 430 locations in the United States as potentially containing underwater munitions with polluting potential (SERDP 2010). From 2001 to 2005, the U.S. Office of Naval Research (ONR) fostered research on mine burial prediction through an Accelerated Research Initiative (ARI) (Bennett 2000). As part of efforts to improve the risk assessment to remediation actions, a six degrees of freedom (6-DoF) model named IMPACT35 was developed to predict the three-dimensional trajectory of sea mines (Chu et al. 2004; Chu and Fan 2005, 2006; Chu 2009) and refurbished into an underwater munition scour burial (UnMUSB) model to predict seafloor munitions'

[3] Department of Oceanography, Naval Postgraduate School.

mobility and burial (Chu et al. 2021, 2022; Chu and Fan 2022). The UnMUSB model requires environmental parameters such as waves, currents, and sediment accretion/ erosion in order to accurately predict the location, mobility, and burial of munition. Delft3D, a freely available open-source numerical model software package (Deltares 2022a), is capable of providing the parameters required by UnMUSB.

Previous works on sedimentation and erosion caused by consecutive storms have studied high-energy storm events in typically higher-energetic locations (Lee et al. 1998; Ferreira 2005; Callaghan et al. 2008; Vousdoukas et al. 2012), but not on moderate-energy storm events in lower-energetic locations. In this study, Delft3D is used to predict the measured seafloor elevation obtained at a single mooring over the mid-shelf off the coast of Panama City, Florida (lower-energetic location) and to identify the mechanisms responsible for the observed sediment accretion and erosion during the passage of two consecutive atmospheric cold fronts using observed significant wave heights, mean currents, and sonar images.

J. FIELD EXPERIMENT

1. Study Area

The study area, off the coast of Panama City, Florida, in the northern Gulf of Mexico (Figure 14), is considered a lower-energetic location (Calantoni et al. 2014), where the mean wave period is 8 seconds and the mean wave height is 0.9 m (Farrar et al. 1994a). This area has a diurnal tide with a maximum tidal range of 0.4 m (Bunya et al. 2010) and seasonal winds primarily from the north in winter and fall and from the south in summer and spring with a weak mean wind speed of around 3 m/s (Chu et al. 2006). In the hurricane seasons, from June to November, high waves and surges associated with sporadic storms can cause significant morphologic changes on the coast of Panama City (Taiani et al. 2012). The sedimentation is primarily quartz sand with a grain density of approximately 2,650 kg/m^3 (Plant et al. 2013). The sediment collected during TREX13 is within the fine sand category at the shallow quadpod location (solid dot in Figure 14b).

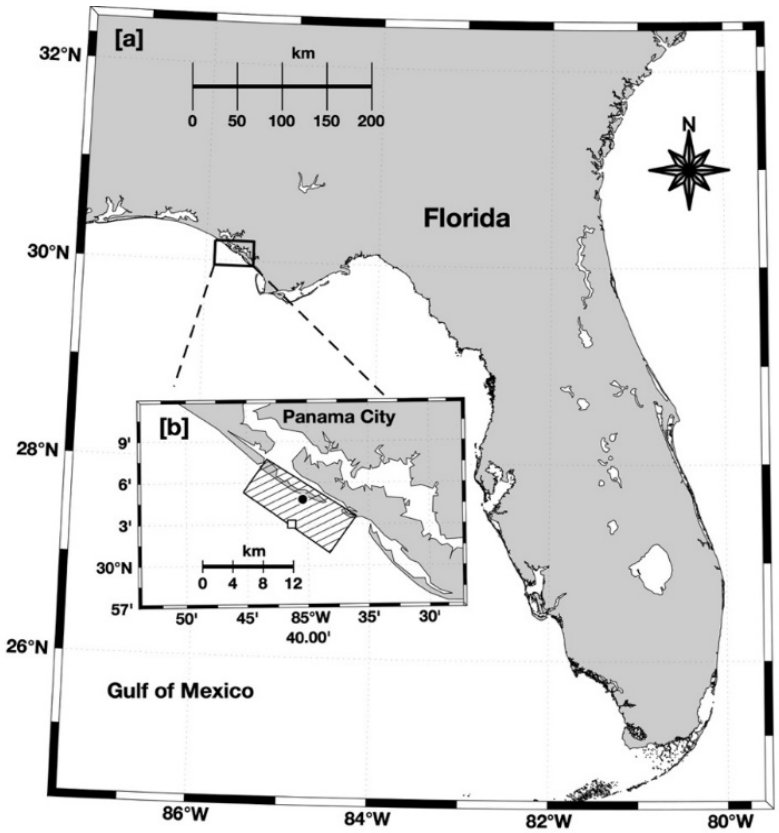

(a) The location of the coast of Panama City is indicated by the black rectangle. (b) The study area is highlighted by the hatched rectangle. The black dot represents the location of the shallow quadpod at 30° 04.81′ N, 85° 40.41′ W, and the white square denotes the deep quadpod location at 30° 03.02′ N, 85° 41.34′ W.

Figure 14. Northern Gulf of Mexico map

2. Instrumentation

During the TREX13 in April and May 2013, two metal structures called shallow and deep quadpods were deployed cross-shore on 20 April with attached oceanographic instrumentation. The shallow quadpod is approximately 2.3 m tall at the water depth of 7.5m (black dot in Figure 14b), and the deep quadpod is approximately 3.3 m tall at the water depth of 20m (white dot in Figure 14b). Non-explosive surrogate munitions with different sizes and densities were placed on the seafloor in both quadpod locations (Calantoni et al. 2014). Locations of surrogates along with seafloor topography were recorded once every 12 minutes by a 2.25 MHz sector scanning sonar Imagenex 881 at 105 cm above the seafloor with 110 degrees of azimuth and 6-m range. Horizontal

currents were measured for 20 minutes every half hour at 2 Hz from the top of each quadpod to the surface at 50 cm vertical resolution by upward-looking Nortek AWAC 1 MHz acoustic Doppler current profilers (ADCP) at 2.3 m above the seafloor. Mean currents were computed from the hourly depth-averaged flow. The mean water level, significant wave height (highest one-third of waves), mean wave direction, and peak wave period were estimated from AWAC pressure data. Additionally, the seafloor elevation was measured by the identified depth of maximum backscatter from a faced-down 1.5 MHz Sontek pulse coherent acoustic Doppler profiler (PC-ADP) at 80 cm above the seafloor. The PC-ADP also continuously measured the seafloor up to 80 cm and the suspended sediment concentration with 5 cm bins of spatial resolution and 2Hz of temporal resolution. All equipment was retrieved on 23 May 2013.

3. Time Series of Observed Data

Considerable modifications in the seafloor were observed during TREX13 after the passage of two consecutive cold fronts in early May 2013. The evolution of current magnitude, significant wave height, and sediment accretion at the shallow quadpod are provided in Figure 15. The gray stripes in Figures 15a and 15b represent the two periods of sediment accretion corresponding to the first and second cold front passages. The oceanographic conditions before 4 May (i.e., before front passage) represented typical lower-energetic features with weak hourly averaged current speed ranging between 0.01 and 0.15 m/s (Figure 15a) and small significant wave height ranging between 0.2 and 0.5 m (Figure 15b). The significant wave height increased to 1.2 m during the first cold front passage and reached 2 m during the second front passage. The seafloor elevation (black line in Figure 15c) was measured from the PC-ADP maximum backscatter of the water column from the seafloor up to 0.6 m and increased approximately 5 cm and 15 cm during the first and second cold front passages. Suspended sediment in the water column is also observed (greenish backscatter) starting from the first front passage. The backscatter of suspended sediment is even stronger (yellowish/reddish) during the second front passage, indicating that sediment transport is likely increasing.

In both front passages, sediment accretion and significant wave height increased simultaneously. Such an apparent synchronization between wave and sedimentation and the weak currents associated with the two cold front passages (Figure 15) suggest that waves primarily drive the observed morphological changes. Although similar conditions of waves and currents were observed at the deep quadpod, the seafloor elevation changes were not evident.

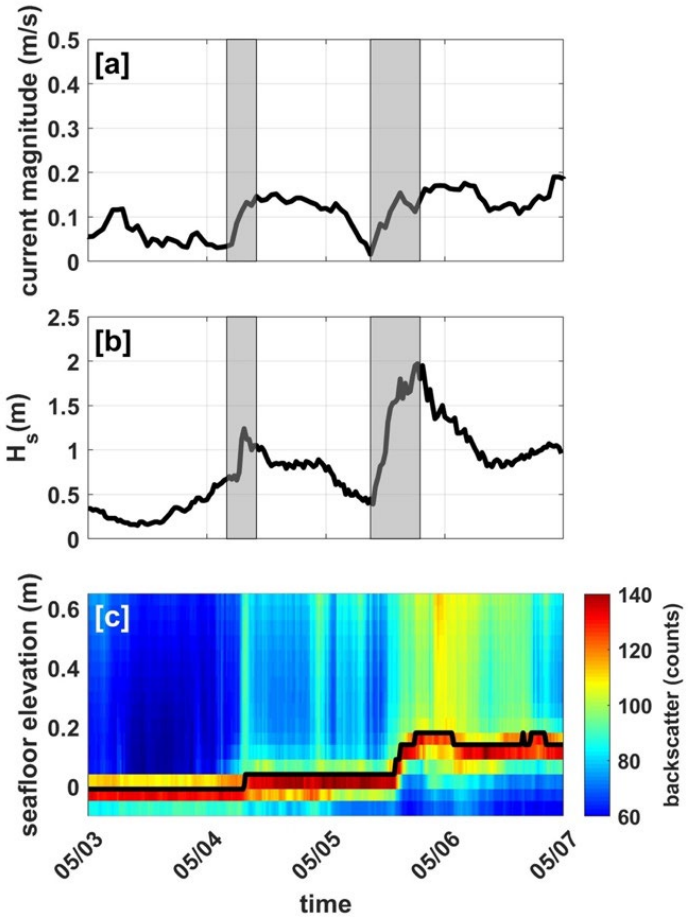

Time series of (a) observed current magnitude (1h-average), (b) significant wave height, and (c) seafloor elevation (black curve) from the PC-ADP maximum backscatter of the water column from the seafloor up to 0.6 m (color plot) from 3 to 5 May are shown. The periods highlighted in gray represent the two periods of sediment accretion at the shallow quadpod location and correspond to the first and second cold front passages.

Figure 15. Time series of observed current magnitude, significant wave height, and seafloor elevation

Klammler et al. (2021) used a poroelastic wave-sediment interaction model to infer that the 15 cm increase in seafloor elevation identified from the PC-ADP maximum backscatter (shown in Figure 15c) is a result of sediment liquefaction by loss of vertical effective stress. In addition, they estimated a 10 cm sinking of the quadpod into the sediment during the passage of the second cold front and recognized the uncertainty about the contributions of bedform migration and scour for the observed morphological data shown in Figure 15c. We use a well-known numerical model, Delft3D, to supplement their contributions to explain the observed increase in seafloor elevation.

K. MODELING SYSTEM

The open-source modeling system Delft3D (Lesser et al. 2004) version 4.04.01 is implemented to predict currents, waves, sediment transport, and morphological evolution in the nearshore environment off the coast of Panama City. The flow module (Delft3D-Flow), either two-dimensional or three-dimensional, is forced by tides, winds, and density, predicts the currents, and feeds the current data as input into the wave and morphology modules (Deltares 2022a). In addition, the flow module is also able to predict suspended sediment transport, bedload transport, and bathymetric variation for both cohesive (e.g., silt and clay) and non-cohesive (e.g., gravel and sand) sediments through solving the advection-diffusion equation with the empirical formulation. However, this study is limited to the sandy seafloor. The cohesive sediments are not included. The wave module (Delft3D-Wave) uses a third-generation model, SWAN, derived from an Eulerian wave action balance equation (Booij et al. 1999) to predict the wave generation, propagation, dissipation, and non-linear wave-wave interactions with inputs from the flow module such as water level, bathymetry, wind, and currents (Deltares 2022b). The morphology module (Delft3D-MOR) is an integrated process-based model to predict the bathymetric change under impact of waves, currents, and sediment transport from the flow and wave modules. The bathymetric change feeds back to the flow and wave modules, and the loop restarts. Similar to earlier studies in this area (Pessanha 2019; Chu et al. 2021), the model grids and tide-forcing boundary conditions are identified in the Delft Dashboard (DDB), which is based on MATLAB and integrated

into Delft3D. Our study area is considered vertically well mixed. Hence, the two-dimensional barotropic model approach is adopted.

1. Grids, Bathymetry, and Wind Input

Two uniform grids with different resolutions for the flow module are nested (Figure 16) to create outer and inner grids. The outer grid (coarser resolution) is 137×75 with 50 m resolution in both alongshore and cross-shore directions. The inner grid (finer resolution) is 139×124 with a 20 m resolution. The sediment transport and morphological evolution are computed only in the inner grid of the flow module to compare with the TREX13 measurements. The domain for the wave module (Figure 16) is determined to avoid the boundary effect and allow the use of deep quadpod data to set up the wave boundary conditions. The wave grid is 273×111 with a 50 m resolution. The bathymetric data (Figure 16) is from the Northern Gulf Coast Digital Elevation Model from NOAA/ NGDC (NOAA/NGDC 2010). The resolution of this data set varies between 1/3 arc-second and 1 arc-second (around 10 and 30 m). The wind input files are set up using the ERA5 Reanalysis data from ECMWF, with a 0.25° (around 28 km) resolution (ECMWF 2019).

2. Initial and Boundary Conditions

Global Inverse Tide Model TPXO 8.0, included in the DDB, is used to create the boundary conditions for the flow module. For the alongshore boundary, the water level is imposed with the astronomic forcing. The water level gradient is set up to zero open boundaries (a so-called Neumann boundary condition). It allows for the flow to leave and enter the lateral boundaries with no spurious circulation (Roelvink and Walstra 2005). The water level is set to zero initially. Additionally, the boundary conditions for sediment transport are set by specifying the inflow concentration as 0 kg/m^3. The initial condition for the sediment concentration is set as 0 kg/m^3, and the initial bed of sediment is set to 5 m. The wave boundary conditions are set based on the measurements from the deep quadpod location using the significant wave height, wave period, wave directions, and directional spreading. These parameters are applied uniformly on the three open boundaries.

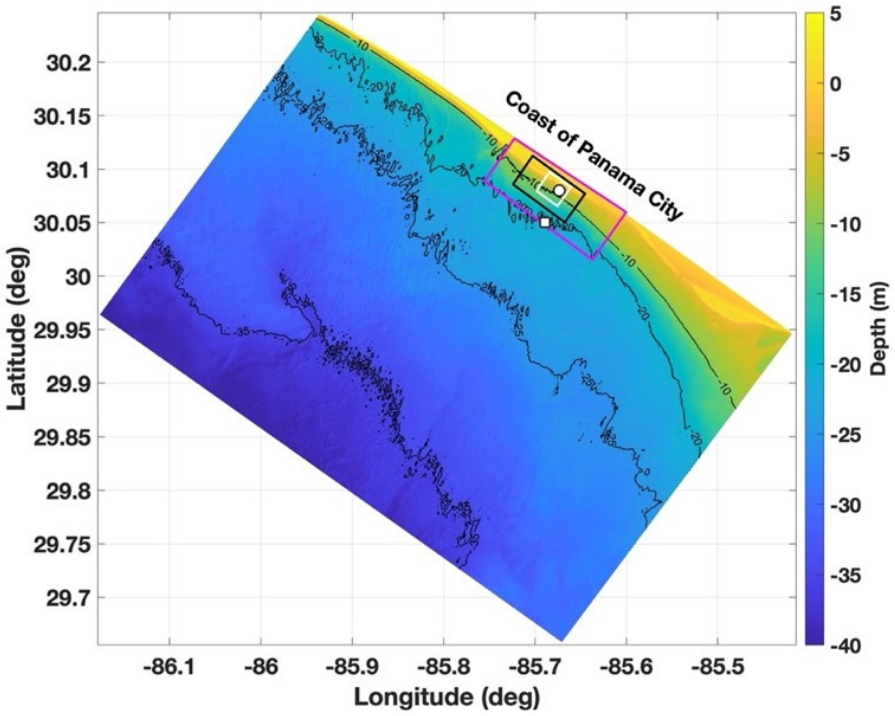

Bathymetry, depth contours (10 m, 20 m, 25 m, and 35 m), wave (magenta), flow outer (black), and flow inner (white) computational grids enclosures are indicated on the map. The black dot represents the shallow quadpod location, and the white square denotes the deep quadpod location.

Figure 16. Bathymetry, depth contours, and computational grids enclosures

3. Calibration and Model Parameters

The calibration is directed to adjust the parameters and allow a better agreement between the model output and measurements. The period between 21 and 27 April is selected for calibration due to observed significant variations in water level, waves, and currents. During the calibration, the model-generated water level, waves, and currents are compared to the observations, and model parameters are adjusted individually, with one being fine-tuned and others remaining unchanged.

Typically, the water level is calibrated by adjustments in the boundary conditions. However, since the minimal difference is reached in amplitude and phase between modeled and measured tides, no boundary condition adjustment is required to calibrate the water level. The waves are calibrated with different JONSWAP bottom friction coefficients and wave height to water depth ratio (γ) in the depth-induced breaking model

(Battjes and Janssen 1978) and with adjustments in the boundary conditions. The Chézy friction coefficient is calibrated with flow velocities. Based on the Courant–Friedrichs–Lewy number, the time step is set as 12 seconds for the coarse domain (50 m) and 6 seconds for the detailed domain (20 m). The model used a uniform Chézy bottom roughness of 65 $m^{1/2}/s$. Horizontal eddy viscosity and horizontal eddy diffusivity were set as 0.5 m^2/s and 10 m^2/s, respectively.

The computational mode for waves is set as stationary. Also, the coupling time between the flow and wave modules is set to 60 minutes. The JONSWAP model (Hasselmann 1974) is used to calculate the bottom friction component of wave dissipation with constant bottom friction. Also, the depth-induced breaking (Battjes and Janssen 1978) is set with α equal to 1 and γ equal to 0.73. The model has a directional resolution of 5° and 24 frequency bins from 0.05 Hz to 1 Hz.

The spin-up interval of 720 minutes is established to prevent any influence of a possible initial hydrodynamic instability on the bottom change calculation, which starts only after the spin-up interval. The sediment type is set as sand with a sediment-specific density of 2,650 kg/m^3.

L. RESULTS AND DISCUSSION

1. Consecutive Cold Fronts

Between 4 and 6 May, two cold fronts passed through Panama City, driving northward swell associated with winds from the south following the historical pattern of frontal incursions into the Gulf of Mexico (DiMego et al. 1976; Guo et al. 2020). Figure 17 presents a sequence of surface weather maps from the Weather Prediction Center website (NOAA/WPC 2020) from 3 to 6 May. On 3 May, the first cold front extended from Arkansas to the southern U.S. and moved across Louisiana towards Florida (Figure 17a). The first cold front reached Panama City between 4 and 5 May (Figure 16b) and coincided with maximum significant wave heights of 1.2 m and a peak wave period of 10 seconds observed at the shallow quadpod location. On 5 May, the second front extended over northern Texas (Figure 17c), and crossed over Panama City between 5 and 6 May (Figure 17d), causing higher wave conditions. For the second cold front passage,

observations at the shallow quadpod location exhibit significant wave heights of 2 m and a peak wave period of 7 seconds for the second cold front passage.

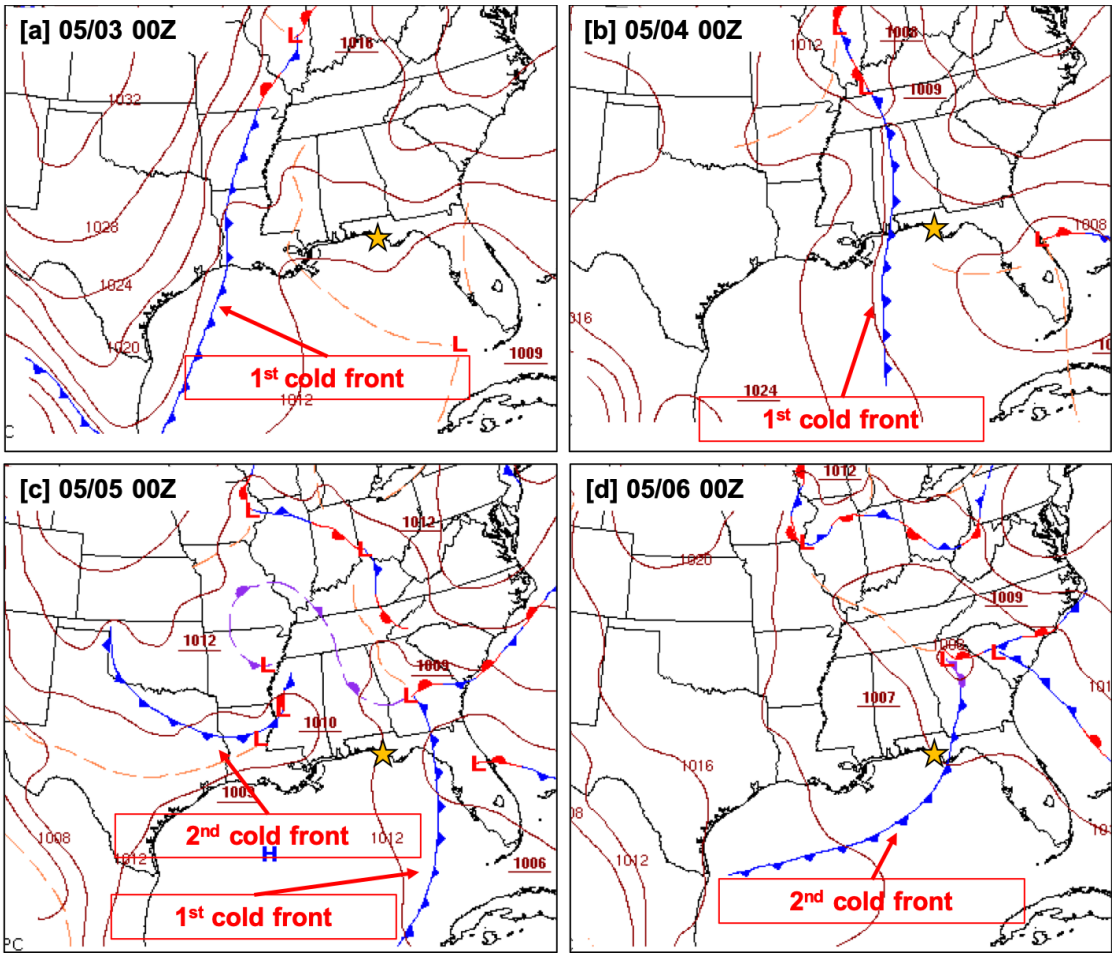

The first cold front reached Panama City (highlighted by the yellow star) between 4 and 5 May and the second front between 5 and 6 May.

Figure 17. Surface analysis including passage of cold fronts through the northern Gulf of Mexico during 3–6 May 2013. Adapted from NOAA/WPC (2020).

2. Model Performance

The model performance is quantified by skill score (Willmott 1981), relative mean absolute error (RMAE) (van Rijn et al. 2003), root-mean-squared error (RMSE), and bias. The skill score reveals the level of the accuracy of the model in estimating the observed variable. The skill score is 1 for the perfect agreement and 0 for the complete disagreement between the modeled and observed data. Table 3 shows a qualification of

error ranges based on wave height and current magnitude (van Rijn et al. 2003), and Table 4 condenses the statistical guidelines to determine the minimum performance of a model based on RMSE and bias (Williams and Esteves 2017). The model capability to predict the quick increase of sediment is evaluated using observed PC-ADP maximum backscatter data and quantified by the Brier Skill Score (BSS) (van Rijn et al. 2003) (shown in Table 5). The model performance is evaluated using the data collected at the shallow quadpod during the TREX13 experiment.

Table 3. Qualification of model performance using RMAE for wave height and current magnitude. Adapted from van Rijn et al. (2003).

Qualification	**Wave height** (m)	**Current Magnitude** (m/s)
Excellent	<0.05	<0.1
Good	0.05–0.1	0.1–0.3
Reasonable/Fair	0.1–0.2	0.3–0.5
Poor	0.2–0.3	0.5–0.7
Bad	>0.3	>0.7

Table 4. Qualification of model performance using RMSE and bias. Adapted from Williams and Esteves (2017).

Model Predictions	**RMSE**	**Bias**
Water Level	No bigger than 0.1m	No bigger than 0.1m
Current Magnitude	Within <0.05m/s is very good, <0.1m/s is good, <0.2m/s is moderate, and 0.3m/s is poor.	No bigger than 0.15m/s

Table 5. Qualification of model performance using BSS for morphological changes. Adapted from van Rijn et al. (2003).

Qualification	**BSS**
Excellent	1.0–0.8
Good	0.8–0.6
Reasonable/fair	0.6–0.3
Poor	0.3–0
Bad	<0

3. Hydrodynamics

The mean water level (1h-average) relative to the local mean sea level is well predicted, although occasionally, the model underestimates the maxima and minima as much as 0.03–0.05 m (Figure 18) with the skill score as 0.99, the bias as 0.001 m, and the RMSE as 0.029 m.

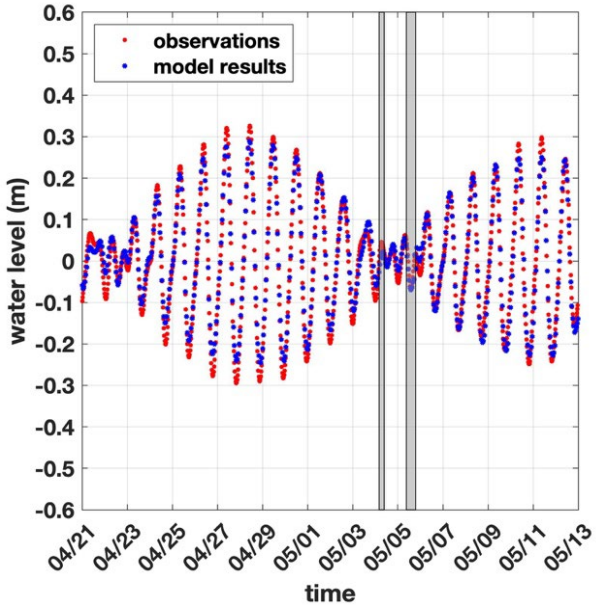

Water level comparison between model results in blue and hourly averaged water level in red from the shallow quadpod location. The water level is referenced to the local mean sea level. The periods highlighted in gray represent the two periods of sediment accretion at the shallow quadpod location and correspond to the first and second cold front passages.

Figure 18. Comparison between observed and predicted water level

The significant wave height (H_s) and mean wave direction (θ) are well predicted (Figures 19a and 19c) with the skill score as 0.951, the bias as 0.062 m, the RMAE as 0.028, and the RMSE as 0.134 m for the significant wave height. Applying the RMAE criteria (Table 3), the model performance for H_s is considered "excellent." However, the wave peak period (T_p) is not well predicted. The model only qualitatively predicts the variation pattern of T_p qualitatively with underestimation in some periods, as illustrated in

Figure 19b. The differences between modeled and observed values may be caused by imperfect boundary conditions or unmodeled physical processes.

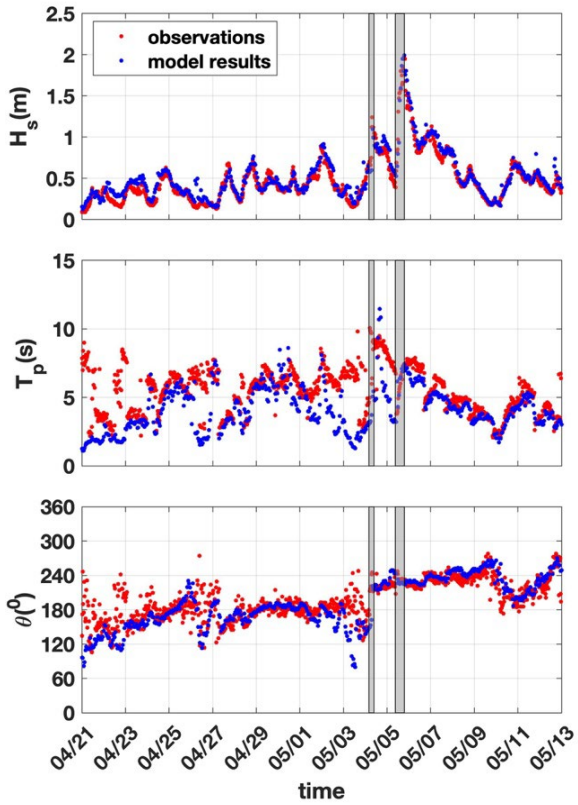

Comparison between observed and predicted significant wave height (H_s), wave peak period (T_p), and mean wave direction (θ) between model results in blue and observations in red from the shallow quadpod location. The mean wave direction is reported as coming from. The periods highlighted in gray represent the two periods of sediment accretion at the shallow quadpod location and correspond to the first and second cold front passages.

Figure 19. Comparison between observed and predicted significant wave height (H_s), wave peak period (T_p), and mean wave direction (θ)

Modeled and observed hourly depth-averaged cross-shore and along-shore currents are determined by rotating the currents 155° clockwise from north to align with the shoreline (Figure 20). The cross-shore component is represented by positive values when the flow moves onshore and negative values when the flow moves offshore (Figure 20a). The along-shore component is defined by positive values when the flow moves eastward and negative values when the flow moves westward (Figure 20b). The quality

of the current speed prediction is represented by the skill score as 0.487, the bias as -0.033 m/s, the RMAE as 0.447, and the RMSE as 0.071 m/s. The bias and RMSE are within limits established in Table 4. The model performance is "reasonable" considering the RMAE criteria (Table 3).

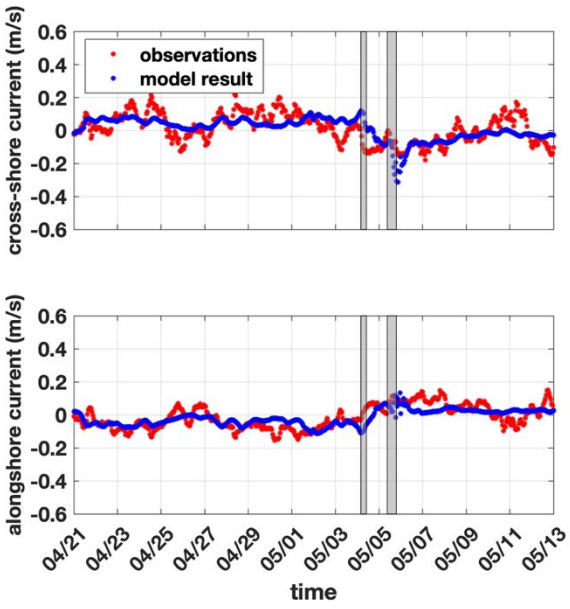

Comparison of cross-shore and alongshore current between model results (in blue) and hourly average currents (in red) observed at the shallow quadpod location. Positive (negative) values of current denote onshore (offshore) flow for the cross-shore component and eastward (westward) flow for the along-shore component. The periods highlighted in gray represent the two periods of sediment accretion at the shallow quadpod location and correspond to the first and second cold front passages.

Figure 20. Comparison between observed and predicted cross-shore and alongshore current

4. Morphological Changes

Let $\eta(x,y,t)$ be the model predicted seafloor elevation with (x, y) the cross-shore and alongshore coordinates. Figure 21 shows the model-observation inter-comparison of the seafloor elevation at the shallow quadpod location (x_s, y_s) for the period between 3 and 10 May with different median grain sizes in the model. The black curve represents the time evolution of the seafloor elevation identified from the PC-ADP maximum

backscatter. Considering that more than 79% of the sediment samples collected during the TREX13 experiment are classified as fine sand (Calantoni et al. 2014), the morphological module is simulated with three median grain sizes D_{50} (150μm, 200μm, 250μm) with D_{50} = 200μm agrees most with the observation. The BSS is computed as 0.913, which is considered as "excellent performance" according to the criteria described in Table 5.

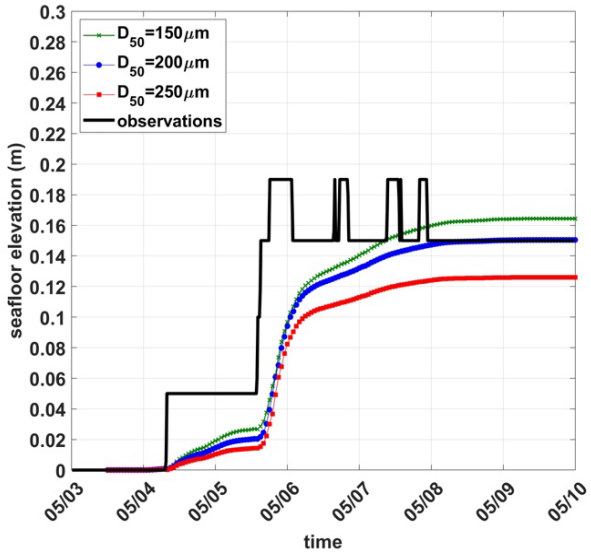

The black line indicates the observed seafloor elevation measured from the PC-ADP maximum backscatter. The green, blue, and red lines represent the model output for sediment accretion with different grain sizes.

Figure 21. Sediment accretion time series at the shallow quadpod location

Figure 22 shows the time evolution of sector scanning sonar images and model predicted sediment erosion/accretion at the shallow quadpod location under the two consecutive cold front passages. All sonar images are averaged in a time window of 4 hours centered on the date/time displayed in each image to reduce the noise. Before the passage of the first cold front on 4 May 0600 (Figure 22a), the sonar image shows sand ripples and three surrogate munitions highlighted by the blue arrows. On 4 May 0900 (Figure 22b), the incoming swell associated with the first front stirred up the bottom and increased the sediment transport. After the passage of the first cold front on 5 May 0600, the sonar image displays munitions on the seafloor and indicates that the sediment

accretion is not sufficient to bury the munitions (Figure 22c). The model prediction of the sediment erosion/accretion before (4 May 0600, Figure 22d), during (4 May 0900, Figure 22e), and after (5 May 0600, Figure 22f) the passage of the first cold front agrees well with observations of minimal sedimentation at the shallow quadpod location represented by the green dot (Figure 22f). The duration of the second cold front is longer than the first front, which leads to more influence on the seafloor. During the second cold front passage on 5 May 1900 and 6 May 0600 (Figure 22g and 22h), the bedform changed dramatically and the sand partially covered the munitions. Eventually, the munitions were completely buried by 7 May 0600 (Figure 22i). On 8 May, all munitions near the shallow quadpod location were recovered during a maintenance dive, confirming the munitions were buried and not carried by the flow. The morphological module predicts quick sedimentation near the shallow quadpod location due to the second cold front passage (Figure 22j, 22l, and 22m), in accordance with the observations.

Let $\hat{\eta}(x,t)$ be the alongshore averaged $\eta(x,y,t)$ to show the temporal and cross-shore variability (Figure 23), i.e., the time evolution of the cross-shore erosion/accretion. The basic feature is the nearshore (within 250 m to the coast) erosion and offshore (more than 250 m from the coast) accretion. After the first front passage on 4 May 0900, the nearshore erosion reaches a maximum around -0.30 m, and the offshore accretion varies between 0.01 m and 0.09 m. During the second front passage from 5 May 1900 to 6 May 0600, the nearshore erosion increases to -0.45 m and the offshore accretion enhances between 0.09 m and 0.25 m. The maximum sedimentation (area in red in Figure 23) is rapidly formed by the end of 5 May between 350 m and 550 m offshore.

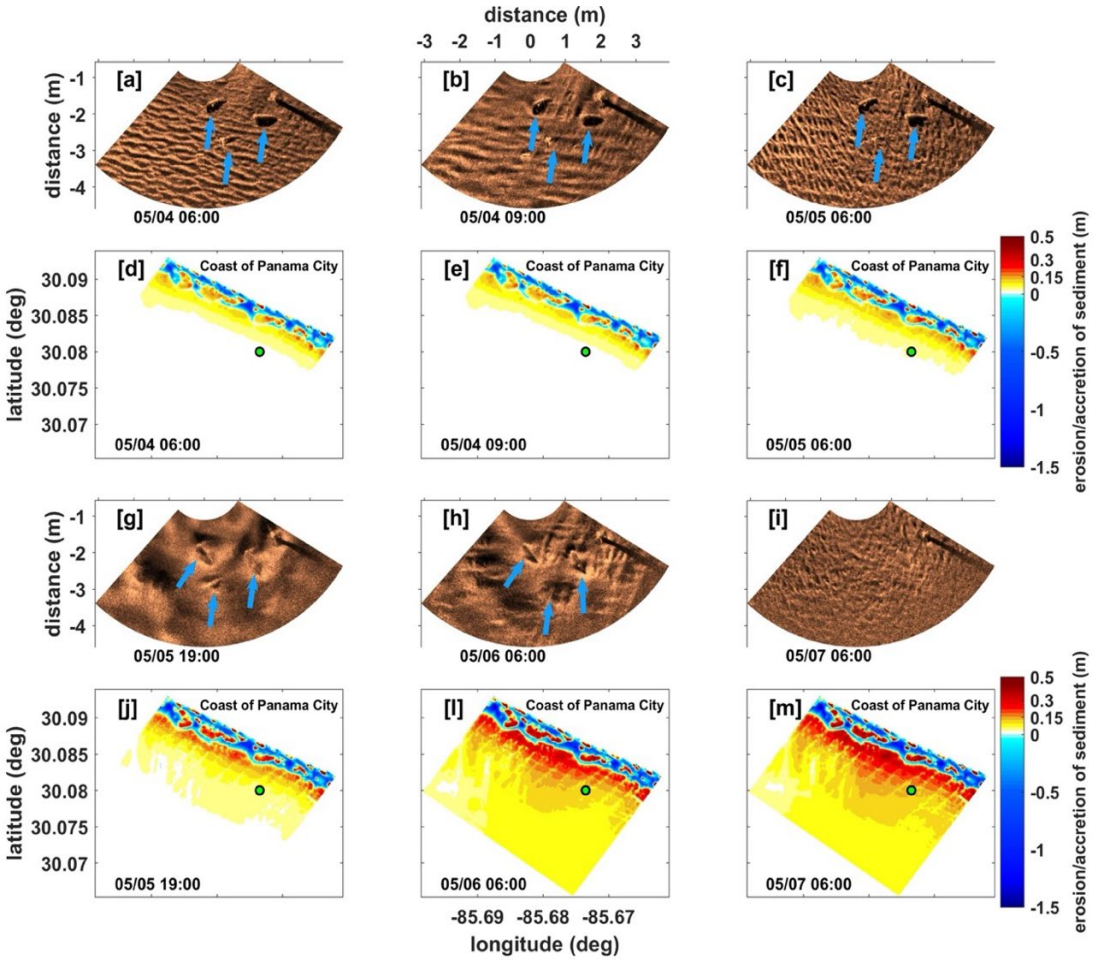

Sector scanning sonar images and model predicted seafloor elevation $\eta(x, y, t)$ for sediment erosion/accretion on 4 May 0600 (a and d), 4 May 0900 (b and e), 5 May 0600 (c and f), 5 May 1900 (g and j), 6 May 0600 (h and l), and 7 May 0600 (i and m). Sonar images show three munitions (highlighted by the blue arrows) near the shallow quadpod location. Model output covers the detailed domain, with the shallow quadpod location represented by the green dot.

Figure 22. Sonar images and predicted seafloor elevation

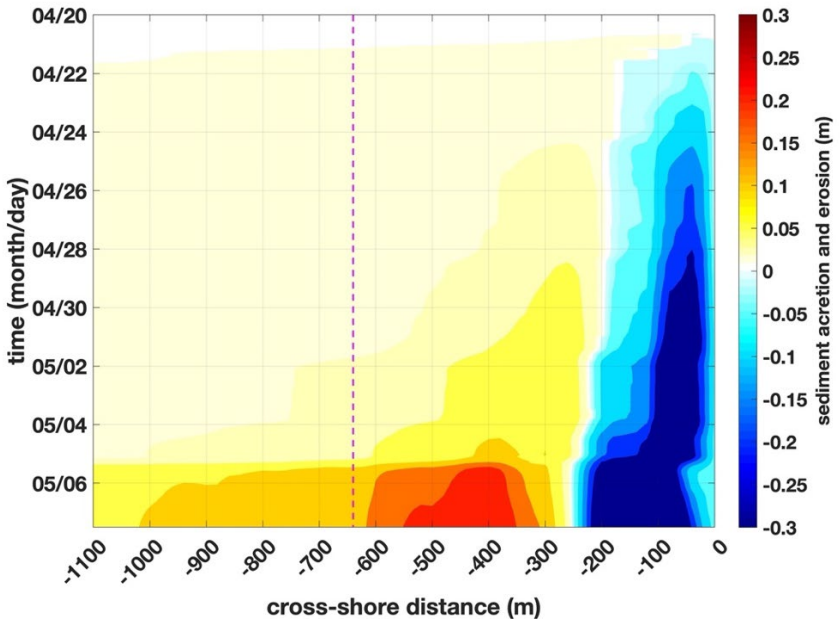

Temporal and cross-shore variability of $\hat{\eta}(x,t)$ between 20 April and 08 May 2013. The magenta dashed line indicates the cross-shore distance to the shallow quadpod location.

Figure 23. Time evolution of the cross-shore erosion/accretion of sediment

Figure 24 presents the model predicted cross-shore bed level profile through the shallow quadpod location before and after the passage of two consecutive cold fronts (Figure 24a). Inlaid in the figure is a zoomed-in region at the shallow quadpod location showing 15 cm of sediment accretion (Figure 24b). The model predicts the peak sediment erosion (-64 cm) and accretion (30 cm) occurred 220 m and 340 m from the shore, respectively. The sediment accretion layer extends in the offshore direction with decreasing thickness as the distance from the shoreline increases. This blanket of 10–20 cm of accretion extends from 500–1200 m from the coastline (Figure 24c).

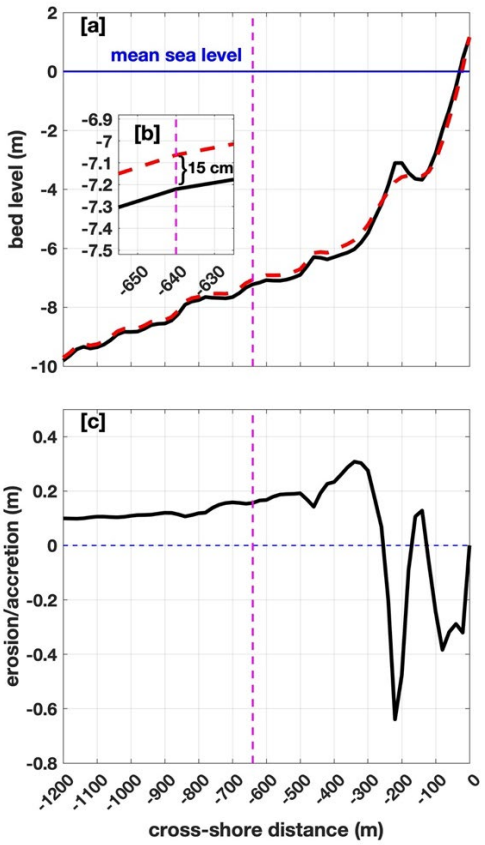

(a) The black line represents the bed level before the passage of two consecutive cold fronts, and the red line is the result of the model simulation denoting the bed level after the consecutive cold front passages. (b) Zooming around the shallow quadpod location to show the 15 cm of sediment accretion. (c) The cross-shore erosion/accretion of sediment along the profile containing the shallow quadpod location. The magenta dashed line indicates the cross-shore distance to the shallow quadpod location.

Figure 24. Development of the cross-shore bed level profile

Tidal currents can greatly influence sediment transport, particularly in areas with a large tidal range. However, during the field experiment, the small tidal range varying between 0.5 m (spring tide cycle) and 0.2 m (neap tide cycle) results in weak tidal currents, especially in the neap tide cycle. To verify the influence of tidal current on sediment transport, a model simulation without waves but with tidal forcing (not shown here) revealed minimal sediment transport and no evident morphological changes in the study area, suggesting that tides play a passive role in short-term (i.e., few weeks) sediment transport and morphological changes. In contrast, the model simulation,

including waves, presented peaks of suspended sediment transport at the shallow quadpod location (Figure 25) during the wave events, implying that waves play the primary role in sediment transport and morphological changes. Furthermore, the model results indicate that suspended sediment transport is predominant, and the bedload sediment transport is minimal.

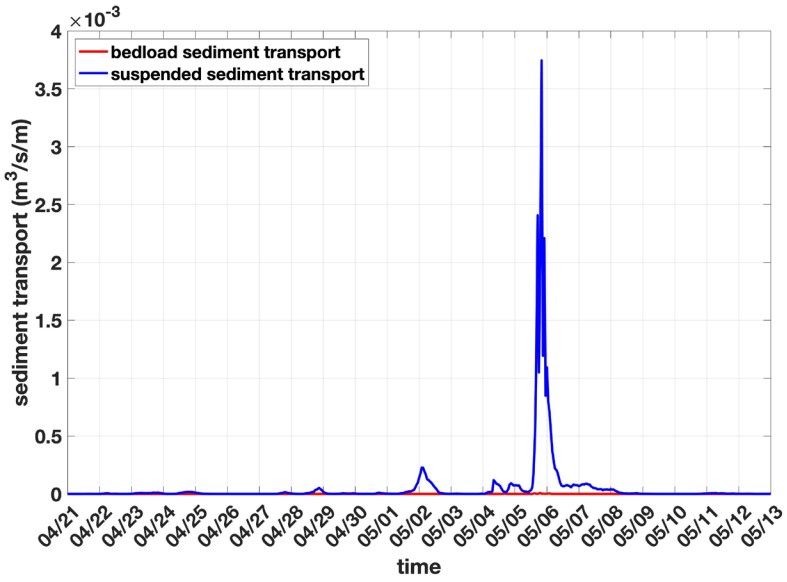

Figure 25. Model results for suspended and bedload sediment transport at the shallow quadpod location

M. CONCLUSION

Interaction between waves and the seafloor during two consecutive atmospheric cold front passages over a lower-energetic area is studied using observations from the TREX13 experiment off the coast of Panama City, Florida, in April–May 2013 and the open-source modeling system Delft3D. The model accurately simulates waves, currents, and morphological changes, including a rapid increase in seafloor elevation after two consecutive cold fronts observed from the PC-ADP at the shallow quadpod (7.5 m water depth). The model simulation indicates that erosion nearshore and sediment accretion offshore starting 250 m from the coast are enhanced during the passage of the cold fronts, suggesting waves have the primary role in driving the observed morphological changes.

In addition, the sediment accretion coincided with the burial of surrogate munitions observed with sonar imagery at the shallow quadpod location, which adds to the contributions of Klammler et al. (2021), who pointed out the occurrence of sediment liquefaction at the exact location during the field experiment, by indicating that sediment accretion also contributes to the observed morphological changes and munition burial. The sediment liquefaction is not included in the Delft3D morphological module and will be investigated in future studies. The results presented in this work demonstrate the possibility of using the model in the risk assessment and cost reduction related to remediation efforts through quality identification of morphological change of seafloor for the prediction of mobility and burial of underwater munitions.

THIS PAGE INTENTIONALLY LEFT BLANK

III. COUPLED MODEL PREDICTIONS OF WAVE-INDUCED LIQUEFACTION AND MORPHOLOGICAL CHANGES

This chapter was submitted to *Journal of Sea Research* for publication (3 August 2022) with minor formatting changes. Co-authors include Vinícius S. Pessanha[4], Peter C. Chu,[4] Matt K. Gough[4], and Mara M. Orescanin[4].

A. INTRODUCTION

In ocean environments, storm-driven waves induce enhanced shear forces on sediment, which may cause seafloor instability affecting coastal structures, such as pipelines, oil storage and production platforms, breakwaters, and the burial of objects (Jeng 2003; Zen et al. 1998; Klammler et al. 2021; Chu et al. 2021). Propagation of ocean waves creates a pressure field that affects the seafloor, inducing stress variations. Changes in the effective stress, which is the difference between total stress and pore water pressure, potentially affect seafloor stability (Sakai et al. 1992).

Both seepage flow and excess pore water pressure modify the effective stress (Zen et al. 1998; Klammler et al. 2021). Seepage flow is the underground motion of seawater into the tiny channels created by the interconnected pore spaces between sediment grains. Seepage is induced by the flow acceleration over the seafloor surface associated with strong horizontal pressure gradients caused by energetic storm waves (Klammler et al. 2020). Excess pore water pressure is created by the temporally variable pressure forcing caused by wave-induced pressure on the seafloor (Zen and Yamazakim 1991; Zen et al. 1998).

Wave-induced liquefaction is a severe case of seafloor instability when the effective stress is zero (Jeng 2018) and the excess pore water pressure causes a decrease in soil strength (de Groot et al. 2006). As a result, the water-sediment mixture behaves like a fluid, causing the seafloor to fail (Sumer 2006), allowing previously resting objects and structures to settle into the sandy seafloor (Sakai et al. 1992). However, models can be used to determine the burial depth of objects owing to liquefaction.

[4] Department of Oceanography, Naval Postgraduate School.

Several models for wave-induced pore pressure and effective stresses have been developed based on different assumptions about soil and fluid characteristics, such as Putnam (1949) assuming a permeable and rigid sandy seafloor and incompressible pore fluid. Yamamoto et al. (1978) developed an analytical solution to study the pore water pressure and effective stress based on poro-elastic theory as proposed by Biot (1941) as well as Madsen (1978), who introduced a similar model for a seafloor of infinite thickness. Another analytical solution was proposed by Hsu and Jeng (1994), but for a seafloor of finite thickness. Jeng (2013) provides a more detailed overview of numerous contributions to modeling wave-induced impacts on the seafloor.

More recently, Klammler et al. (2020) determined the observed burial depth of objects from a site in North Carolina using estimated maximum depths of seafloor failure from wave pressure measurements associated with a dynamic wave-seafloor interaction model (Hsu and Jeng 1994; Jeng 2018) based on a vertical effective stress criterion and the vertical distribution of pore pressures. Using the same methodology (Klammler et al. 2020), Klammler et al. (2021) predicted the burial depth of objects in a field experiment in Florida. Moreover, based on Jia et al. (2014) and Qi and Gao (2018), Klammler et al. (2021) introduced the concept of liquefaction degree, which is defined as the amount of vertical effective stress at the sediment surface that is counteracted by wave-induced pore pressures and can indicate the liquefaction potential. However, both studies did not consider the possible contribution of other processes such as sediment accretion owing to sediment transport in the burial of the objects.

This study has implemented a coupled model comprised of the hydro-morphodynamic model (Delft3D) and wave-induced liquefaction model (Klammler et al. 2020, 2021) to examine the hypothesis that both liquefaction and sediment accretion occurred during the field experiment. The process-based Delft3D model (Lesser et al. 2004) can simulate waves, currents, sediment transport, and morphological evolution in the nearshore environment. Moreover, Delft3D can be used to estimate wave-induced pressure at the seafloor, which is required to assess the liquefaction degree and the depth burial of objects. The wave-induced liquefaction model employed the Delft3D result as the forcing term. The field data were used to verify the model results. In addition, the

model output is employed to create a liquefaction degree and estimated failure depth maps, allowing to expand seafloor instability analysis over the entire area of interest rather than being limited by the location of observation stations as in previous studies.

B. MATERIALS AND METHODS

1. Study Area and Field Experiment[5]

During the field experiment TREX13, which took place in April and May 2013 off the coast of Panama City, Florida, two metal frames called quadpods, on which oceanographic instrumentation was mounted, were deployed. On 20 April, both quadpods were deployed and placed cross-shore (Figure 26); one at a depth of 7.5 m is 2.3 m tall (shallow quadpod), and the other at a depth of 20 m is 3 m tall (deep quadpod). In both quadpod locations, objects of various sizes and densities were set on the seafloor (Calantoni et al. 2014). A 2.25 MHz sector scanning sonar Imagenex 881 with 110 degrees of azimuth and a 6-m range was used to capture the locations of objects as well as the topography of the seafloor once every 12 minutes. Horizontal currents were monitored by upward-facing Nortek AWAC 1 MHz acoustic Doppler current profilers (ADCP) at 2.3 m above the seafloor for 20 minutes every 30 minutes at 2 Hz from the top of each quadpod to the surface at 0.5 m vertical resolution. The hourly depth-averaged flow was used to calculate mean currents. AWAC pressure data was used to determine the mean water level, significant wave height (the highest one-third of waves), mean wave direction, and peak wave period. The depth of maximum backscatter from a facing-down 1.5 MHz Sontek pulse coherent acoustic Doppler profiler (PC-ADP) was also used to determine the seafloor elevation. In addition, the PC-ADP constantly recorded the

[5] The description of the instruments presented in subsection B.1 was previously published by *Journal of Operational Oceanography* (Pessanha et al. 2022).

suspended sediment concentration with 0.05 m bins of spatial resolution and 2 Hz of temporal resolution from the seafloor up to 0.8 m. The seafloor elevation was also determined from the Imagenex 881A pencil beam sonar at 1.21 m above the seafloor with 180 degrees of azimuth, and a 2 m range, performing one scan every 4 hours. On 23 May, all of the equipment was retrieved.

In the study area, typical wave conditions are a mean wave period of 8 seconds and a mean wave height of 0.9 m (Farrar et al. 1994b). Moreover, the diurnal tides have a maximum tidal range of 0.4 m (Bunya et al. 2010). The hurricane season in the study area lasts from June to November, with August and September being the period with the highest number of storms (Chu et al. 2021). The mean wind intensity is around 3 m/s during the off-hurricane season (Chu et al. 2006). The sedimentation is mostly quartz sand with a grain density of 2,650 kg/m^3 (Plant et al. 2013). At the shallow quadpod location (Figure 26), the sediment collected during TREX13 is classified as fine sand (Calantoni et al. 2014).

Two cold fronts passed through Panama City between 4–6 May, driving northward swell along with southerly winds, following the historical pattern of frontal incursions into the Gulf of Mexico (DiMego et al. 1976; Guo et al. 2020). Between 4–5 May, the first cold front passed over Panama City, causing the first wave event at the shallow quadpod location, with a maximum significant wave height of 1.2 m and a peak wave period of 10 seconds. Furthermore, during 5–6 May, a second front crossed over Panama City, causing the second wave event to have more severe wave conditions, with a significant wave height of 2 m and a peak wave period of 7 seconds.

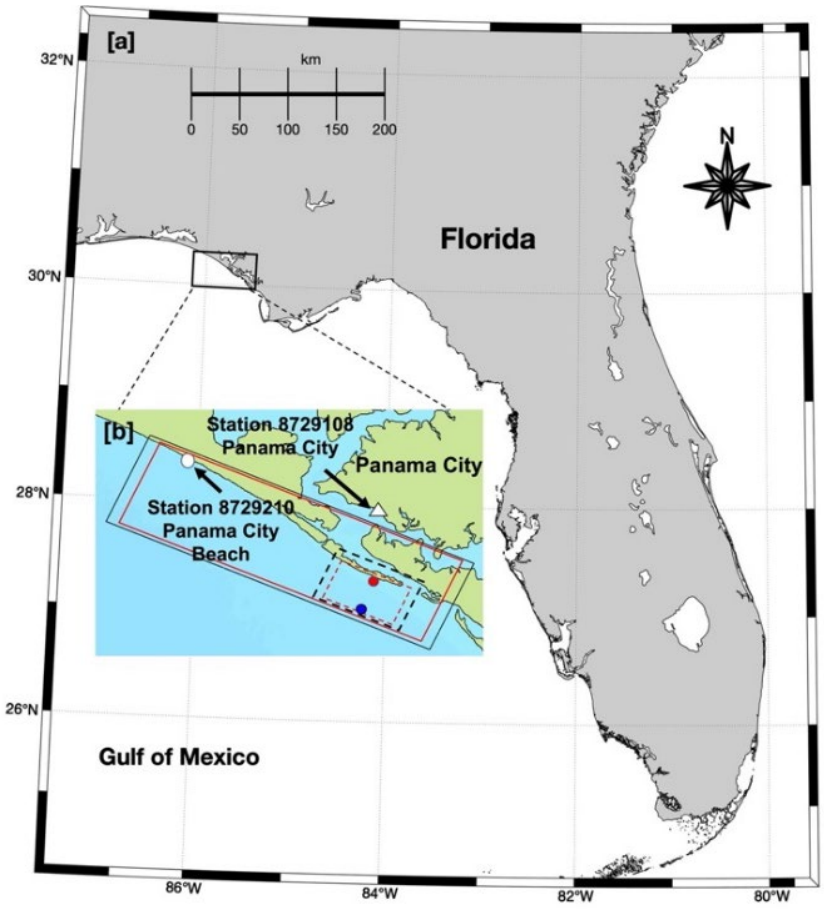

(a) Location of the coast of Panama City indicated by the black rectangle. (b) NOAA stations 8729210 (white dot) at 30.213° N, 85.878° W; 8729108 (white triangle) at 30.152° N, 85.7° W; and model domain area with enclosures for wave outer (black line), flow outer (red line), wave inner (dashed black line), and flow inner (dashed red line) computational grids. The red dot represents the shallow quadpod location (30.08° N, 85.673° W), and the blue dot denotes the deep quadpod location (30.05° N, 85.689° W).

Figure 26. Study area and model domain

2. The Hydro-morphodynamic Model: Approach and Setup

As in recent studies off the coast of Panama City (Pessanha et al. 2022; Chu et al. 2021), the study area was considered vertically well mixed, and density stratification was assumed to be negligible. Thus, the two-dimensional barotropic model approach was adopted using the open-source modeling system Delft3D with three modules: flow, wave, and morphology. The flow module predicts and provides water level and currents as input

for the wave and morphology modules. It also calculates sediment transport under wind and tidal forces and updates bathymetry. The wave module forecasts wave generation, propagation, dissipation, and non-linear wave-wave interactions in the littoral environment using inputs from the flow module such as water level, bathymetry, wind, and currents. Finally, the morphology module works in a cycle with the wave and flow modules to update the bathymetry while considering the sediment transport field. The Delft3D user manual (Deltares 2022a) and Lesser et al. (2004) both offer extra details on the model description.

In order to increase the spatial resolution in the study area, the model was set in two domains: the overall domain with coarse resolution and the nested domain with finer resolution. The overall domain generates the boundary conditions for the nested domain using the offline nesting approach. Therefore, the computation cost is reduced because simulations with the nested domain may be performed independently of the overall domain after generating the boundary conditions. Both domains are composed of two grids, one for the flow and the other for waves (see Figure 26 for grid enclosures). The grids for the overall domain are the flow outer grid covering 34 km alongshore and 11 km across-shore, with a resolution ranging from 500 to 100 m, and the wave outer grid containing 77 × 24 grid points with a 100-meter resolution. For the nested domain, the flow inner grid covers 8.2 km alongshore and 4.8 km across-shore with a resolution of 60 to 20 m, and the wave inner grid has 101×66 grid points with a 40-meter resolution. The sediment transport and morphological evolution were estimated just in the flow inner grid to reduce the computational effort. The bathymetric data (Figure 27) used in all grids were obtained from the Northern Gulf Coast Digital Elevation Model from NOAA/ NGDC (NOAA/NGDC 2010), with the resolution ranging from 1/3 arc-second to 1 arc-second (around 10 and 30 m).

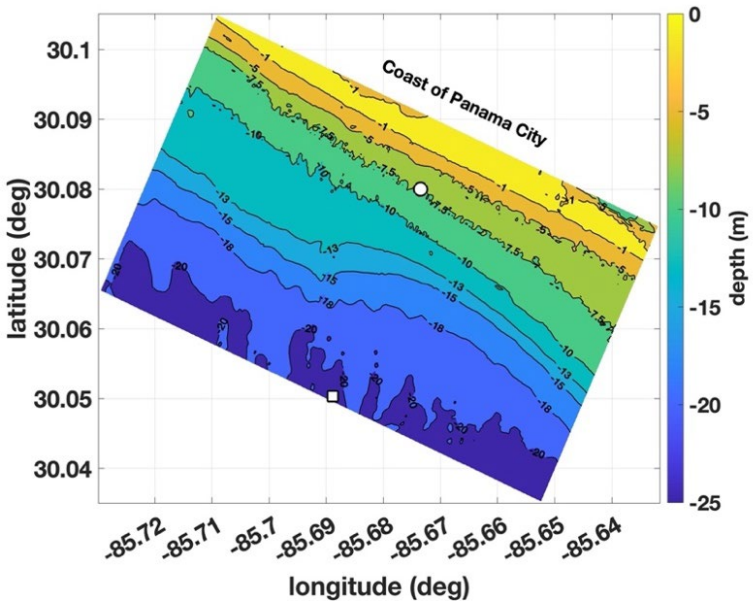

The shallow and deep quadpods are represented by the white dot and white square.

Figure 27. Bathymetry and bathymetric contours

The global inverse solution (Egbert and Erofeeva 2002) based on altimetry data provided the 13 main astronomic constituents used to create the boundary conditions for the flow module. For the alongshore boundary, the water level with astronomic forcing was imposed. The water level gradient (Neumann boundary condition) was chosen with a constant zero water level slope in the longshore direction for both across-shore open boundaries (Chu et al. 2021). It allows for flow to leave and enter the lateral boundaries with no spurious circulation (Roelvink and Walstra 2005). Wave boundary conditions were set based on the measurements from the deep quadpod location using the significant wave height, wave period, wave directions, and directional spreading. These parameters were applied uniformly on the three open boundaries. The wind input files were set up using the ERA5 Reanalysis hourly data from ECMWF, with a 0.25° (around 28 km) resolution (ECMWF 2019).

The time step was set as 12 seconds for the overall domain and 6 seconds for the nested domain based on the Courant–Friedrichs–Lewy number. Default values of the Delft3D model were used for the Chézy bottom roughness (65 $m^{1/2}/s$), horizontal eddy

viscosity (1 m^2/s), initial bed of sediment (5 m), and initial water level (zero m). The computational mode for waves was set as stationary. Furthermore, the coupling time between the flow and wave modules was set to 60 minutes. The JONSWAP model (Hasselmann 1974) was used to calculate the bottom friction component of wave dissipation with constant bottom friction. In addition, the depth-induced breaking (Battjes and Janssen 1978) was set with α equal to 1 and γ equal to 0.73 (default values). The model has a directional resolution of 5° and 24 frequency bins from 0.05 Hz to 1 Hz. The sediment type was set as sand with a sediment-specific density of 2,650 kg/m^3 and median sediment grain size (D_{50}) of 230 μm (Chu et al. 2021). The computation of bottom changes begins only after the 720-minute spin-up interval (default value) that was set to avoid any influence from a possible initial hydrodynamic instability.

3. Wave-Induced Liquefaction Model

The occurrence of wave-induced liquefaction is estimated using the method introduced by Klammler et al. (2020), in which the wave-induced pressure, $p(t)$, is represented as

$$p(t) = \sum_{m=1}^{M} a'_m \cos(-\omega_m t + \varepsilon_m), \tag{14}$$

where t is time, M is the number of terms used, a'_m is amplitude, ω_m is the angular frequency, and ε_m is the phase angle. Using the linear wave theory, the pressure distribution over the seafloor surface, p_b, is calculated as

$$p_b(x,t) = \sum_{m=1}^{M} a_m \cos\left(k_m x - \omega_m t + \varepsilon_m\right), \tag{15}$$

where x is the horizontal location in the direction of wave propagation direction, and the amplitude, a_m, is

$$a_m = a'_m \Big/ \cosh(k_m d_p), \tag{16}$$

with d_p denoting the vertical distance between the pressure sensor and the seafloor surface and k_m representing the wave number computed using the dispersion relation as

$$\omega_m^2 = g k_m \tanh(d k_m), \tag{17}$$

where g is the gravity acceleration and d is mean water depth. The analytical solution (Hsu and Jeng 1994; Klammler et al. 2020) provides the wave-induced pore pressures (p_p), horizontal (σ'_x) and vertical (σ'_z) effective stresses, and shear stress (τ_{xz}) as

$$\begin{bmatrix} p_p \\ \sigma'_x \\ \sigma'_z \\ \tau_{xz} \end{bmatrix} = \mathrm{Re}\left\{ \sum_{m=1}^{M} a_m \begin{bmatrix} P \\ -S_x \\ S_z \\ iT \end{bmatrix} \exp\left[i\left(k_m x - \omega_m t + \varepsilon_m \right) \right] \right\}, \tag{18}$$

where Re{ } is the real part of a complex quantity, i denotes the imaginary unit, z is the vertical coordinate, P, S_x, S_z, and T are complex variables dependent on complex constants and seafloor properties as porosity (n), horizontal (K_x) and vertical (K_y) conductivities, degree of saturation (S_r), shear modulus (G), Poisson ratio (μ), density of sea water (ρ_w), elastic modulus of sea water (K_w). The computation of the complex constants involves approximately 100 expressions described by Jeng (2018). In addition, Klammler et al. (2020) go into further detail regarding how the complex variables and constants are computed. The seafloor and sea water properties used in the computation of the analytical solution are based on Klammler et al. (2020) and listed in Table 6.

Table 6. Seafloor and sea water properties applied to the analytical solution

n [-]	K_x [m/s]	K_z [m/s]	S_r [-]	G [N/m^2]	μ [-]	ρ_w [kg/m^3]	h [m]	K_w [N/m^2]
0.3	10^{-4}	10^{-4}	0.98	10^7	0.3	1025	100	2×10^9

Considering (Jia et al. 2014) and (Qi and Gao 2018), Klammler et al. (2021) proposed a sediment failure criterion based on the annulation of vertical effective stress called liquefaction degree (L), which is defined as

$$L = \begin{cases} \lim\limits_{z\to 0^-}\left[\left(-\gamma_w \sigma'_z\right) / \left(\gamma_s - \gamma_w\right) z \right] & \text{if } \sigma'_z > 0, \\ 0 & \text{if } \sigma'_z \le 0, \end{cases} \tag{19}$$

where specific weights of seawater and saturated sediment are represented by γ_w and γ_s, respectively. As the liquefaction potential is greatest just beneath the seafloor surface, the limit in Equation 19 is evaluated for z tending to 0^-. Negative values of σ'_z cause a

compressive effect on the sediment and act to stabilize it ($L = 0$). Positive σ'_z values, on the other hand, enhance sediment buoyancy and raise the risk of seabed instability ($L > 0$). Values of $L \geq 1$ may indicate an extreme circumstance where the sediment grains float, resulting in a limited and transient episode of wave-induced liquefaction.

4. Simulation Design and Model Performance Assessment

The simulation is designed to hindcast the hydrodynamic conditions observed during the field experiment. First, the model was calibrated and validated. Then the estimated pressure distribution over the seafloor surface from the Delft3D model output was applied as an input for the wave-induced liquefaction model to determine the occurrence of liquefaction. In addition, the morphological changes in the study area were evaluated from the Delft3D model results.

The root mean square error (RMSE) is used to assess the performance of the model in simulating the observed hydrodynamic. Let X be the variable of interest (e.g., significant wave height), X_{mod} the model output, X_{obs} be the observation, N the number of observations, and $\langle X \rangle$ be the time mean.

$$RMSE = \sqrt{\frac{1}{N}\sum\left(X_{\text{mod}} - X_{obs}\right)^2} \tag{20}$$

Likewise, performance is also evaluated using the skill score (SS) defined by

$$\text{SS} = 1 - \left(\sum \left| X_{\text{mod}} - X_{obs} \right|^2\right) \Big/ \left[\sum \left(\left| X_{\text{mod}} - \left\langle X_{obs} \right\rangle \right| + \left| X_{obs} - \left\langle X_{obs} \right\rangle \right|\right)^2\right] \tag{21}$$

to denote the model prediction skill (Willmott 1981) with SS = 1 indicating perfect agreement between model output and observations and SS = 0 indicating total disagreement.

C. RESULTS

1. Model Validation

Model output employing the set-up described in Section B.2 based on previous studies (Chu et al. 2021; Pessanha et al. 2022) was compared with observations at the shallow quadpod location between 24 and 30 April to calibrate the model (not shown).

The model results for mean water level (*MWL*) relative to local mean sea level, significant wave height (H_s), and depth-averaged current in longitudinal (V_e) and latitudinal (V_n) directions were considered satisfactory. Then, no changes to the boundary conditions were applied. The SS for *MWL* was calculated as 0.984 and the RMSE as 0.045 m. The SS for V_e and V_n was calculated as 0.473 and 0.437 and the RMSE as 0.122 m/s and 0.082 m/s, respectively. For H_s, the SS was calculated as 0.924 and the RMSE as 0.079 m.

For model validation, observed *MWL*, V_e, V_n, and H_s are compared with model results at the shallow quadpod location between 22 April and 12 May (Figure 28). The model demonstrated good performance in simulating the observed *MWL* (1h-average). However, after the storm on 5 May, the model underestimated the maxima and minima by as much as 0.1–0.15 m (Figure 28a) owing to the sinking of the shallow quadpod (see Section D.4). The *SS* for *MWL* was calculated as 0.917 and the RMSE as 0.083m. The resulting modeled and observed currents are presented in Figures 28b and 28c. The *SS* for V_e and V_n was calculated as 0.67 and 0.574 and the RMSE as 0.137 m/s and 0.082 m/s, respectively. H_s and mean direction (θ_{dir}) were well represented by the model (Figures 28d and 28e). For H_s, the *SS* was calculated as 0.972 and the RMSE as 0.099 m.

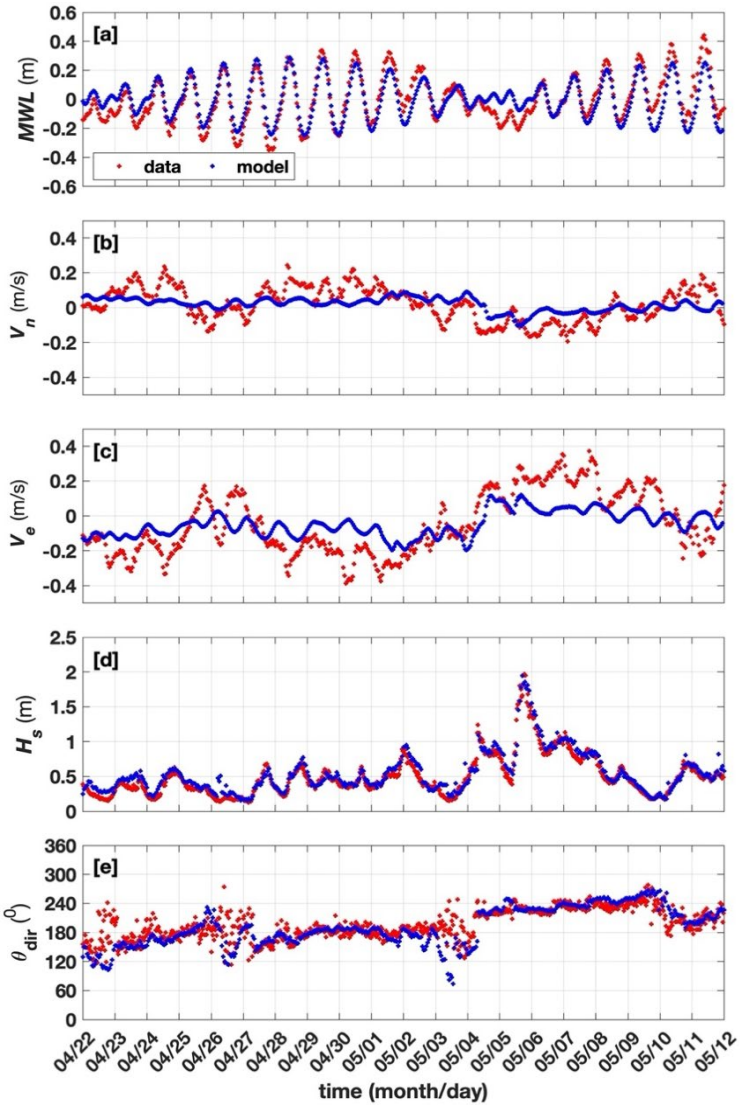

Comparison between model results (in blue) and hourly averaged observations (in red) at the shallow quadpod location for (a) mean water level (*MWL*) relative to local mean sea level, (b) depth-averaged current in longitudinal direction (V_e), (c) depth-averaged current in latitudinal direction (V_n), (d) significant wave height (H_s) and (e) mean wave direction (θ_{dir}) reported as coming from.

Figure 28. Model validation

2. Seafloor Evolution[6]

Seafloor evolution before, during, and after the two wave events at the shallow quadpod location is presented in Figure 29. All sonar images were averaged in a time window of 4 hours centered on the date/time displayed in each image to reduce the noise. Before the first wave event on 4 May 0600 (Figure 29a), the sonar image shows sand ripples and three objects highlighted by the blue arrows. Two of these objects are 15.5 cm in diameter, while the third (near the center of the sonar image) is 8.1 cm. On 4 May 0900 (Figure 29b), the incoming swell associated with the first wave event stirred up the sediment, causing changes in the sand ripples. After the first wave event on 5 May 0600, the sonar image displays objects on the seafloor and indicates that the sediment accretion was not sufficient for the burial of objects (Figure 29c). The second wave event had a more extensive duration and impact on the seafloor. During the second wave event on 5 May 1900 and 6 May 0600 (Figures 29d and 29e), the bedform changed and the sand partially covered the objects. Eventually, the objects were completely buried by 7 May 0600 (Figure 29f). On 8 May, all objects near the shallow quadpod location were recovered during a maintenance dive, confirming the objects were buried and not carried by the flow.

[6] The description of the seafloor elevation presented in subsection C.2 was previously published by *Journal of Operational Oceanography* (Pessanha et al. 2022).

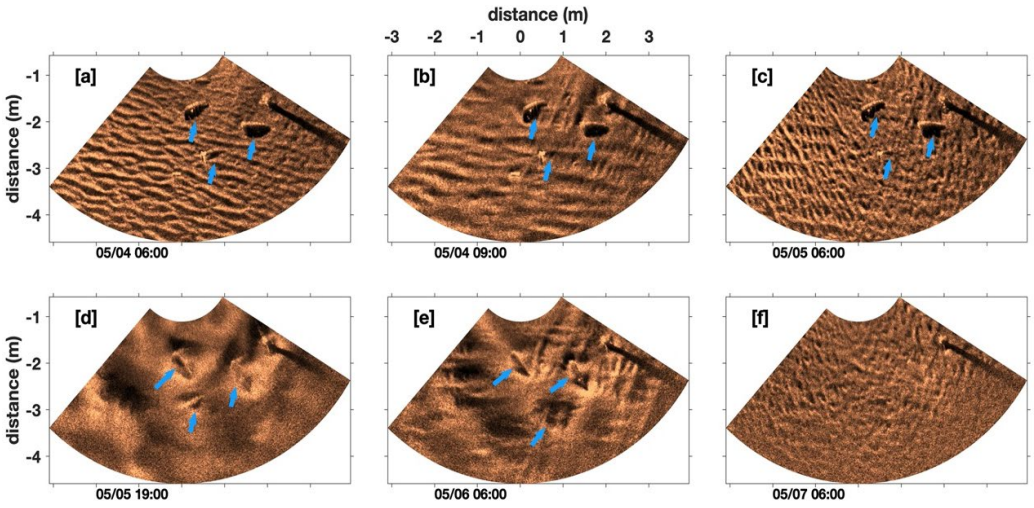

Sector scanning sonar images on (a) 4 May 0600, (b) 4 May 0900, (c) 5 May 0600, (d) 5 May 1900, (e) 6 May 0600, and (f) 7 May 0600. Sonar images show three objects (highlighted by the blue arrows) near the location of the shallow quadpod.

Figure 29. Sonar images

The model output for erosion/accretion of sediment before, during, and after the first wave event (Figures 30a, 30b, and 30c) on 4 May 0600, 4 May 0900, and 5 May 0600 agrees with observations as simulation indicated minimal sedimentation at the shallow quadpod location represented by the green dot (Figure 30c). The second wave event had a more extensive duration and impact on the seafloor. During the second wave event on 5 May 1900 and 6 May 0600 (Figures 30d and 30e), the bedform changed and the sand partially covered the objects. Model results (Figure 30f) indicate approximately 0.05 m of sediment accretion around the shallow quadpod location after the second wave event.

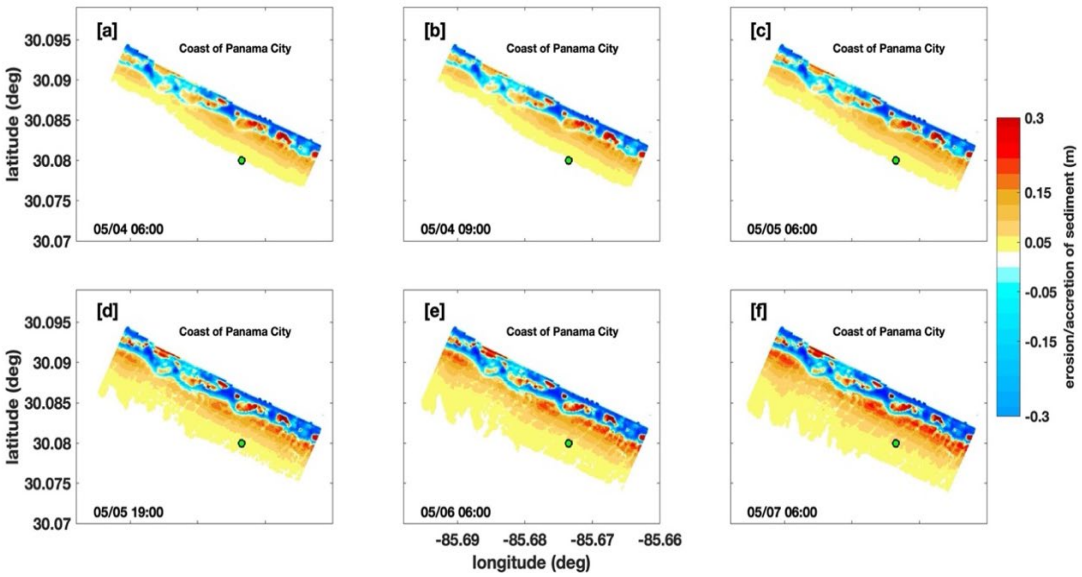

Model output for erosion/accretion of sediment on (a) 4 May 0600, (b) 4 May 0900, (c) 5 May 0600, (d) 5 May 1900, (e) 6 May 0600, and (f) 7 May 0600 are indicated on the map. The shallow quadpod location is represented by the green dot.

Figure 30. Predicted erosion/accretion of sediment

The model results for suspended load and bedload sediment transport at the shallow quadpod location are presented in Figure 31a. Model results indicate that sediment is transported primarily in suspension, with peaks of suspended load transport associated with peaks on H_s and strong backscatter observed in the water column (Figure 31b). In contrast, the bedload sediment transport is nearly zero during the entire period. Figure 31b shows the backscatter of the water column from the seafloor up to 0.6 m and the observed seafloor elevation from the PC-ADP maximum backscatter (black line) and pencil beam sonar (white dot). In Figure 31b, an increase in suspended sediment over the water column is noticed (greenish/yellowish colors) during the first wave event, between 4–5 May, and an observed seafloor elevation by up to 0.05 m from the PC-ADP maximum backscatter and 0.04 m from the pencil beam sonar. Moreover, the backscatter of suspended sediment is even stronger (yellowish/reddish colors) during the second wave event, between 5–6 May, with an additional seafloor elevation by up to 0.15 m from the PC-ADP maximum backscatter and by 0.1 m from the pencil beam sonar. On 6 May, the seafloor elevation from the PC-ADP maximum backscatter decreased 0.05 m

and presented a variation by 0.05 m again between 6–8 May. Observations from the pencil beam sonar presented in the same period but with a smaller amplitude (between 0.02–0.03 m), which may be attributed to sand ripples migration.

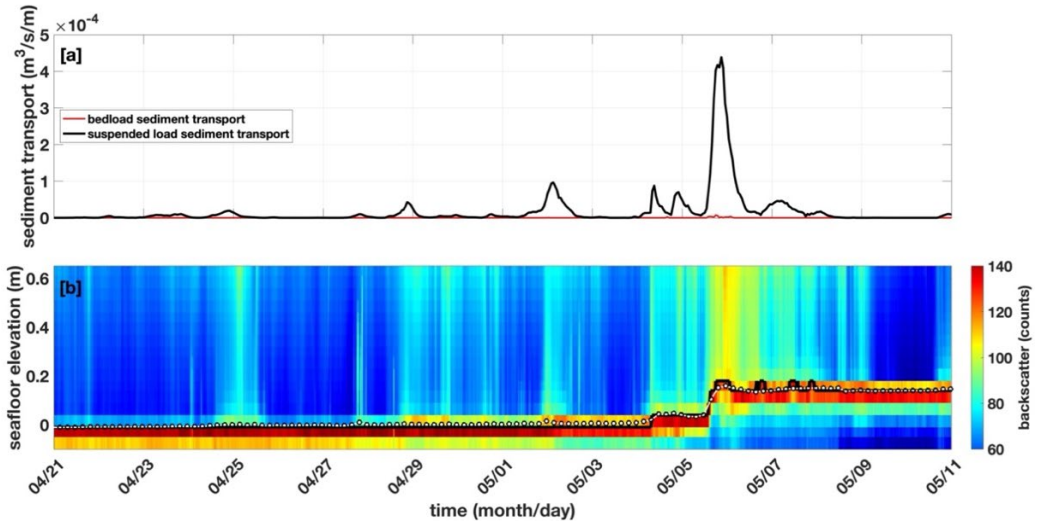

(a) Suspended load (blue line) and bedload sediment transport (red line) from the model output. (b) Backscatter of the water column from the seafloor up to 0.6 m from the PC-ADP. Seafloor elevation is determined from the PC-ADP maximum backscatter (black line) and the pencil beam sonar (white dots). Both model output and observations refer to the shallow quadpod location.

Figure 31. Predicted sediment transport and observed seafloor elevation

3. Liquefaction Degree and Failure Depth

The liquefaction degree (L) was computed at shallow and deep quadpod locations using both the model output and observation. The comparison between them (Figure 32) indicates that L from the model output represented well the L estimated from observation in both locations. Figure 32 presents the L time series, including the storm period (4–6 May). At the shallow quadpod location (Figure 32a), L peaks a maximum of approximately 0.7 during the first wave event. In addition, during the second wave event, the peak of L was approximately 1.1, denoting a seafloor liquefaction condition (L>1). In contrast, low values of L were estimated at the deep quadpod location (Figure 32b) with a peak of approximately 0.4 during the second wave event. The sediment failure depth

calculation based on the criterion of loss of vertical effective stress (Klammler et al. 2020) showed that failure events occurred at the shallow quadpod location on 5 May around 1800, during the second wave event, when $L \geq 1$, and consistent with the period in which the shallow quadpod settled into the sediment. Therefore, for computation using the model output, the maximum failure depth is 0.1 m, and for observation, the maximum failure depth is 0.19 m, which is consistent with Klammler et al. (2021).

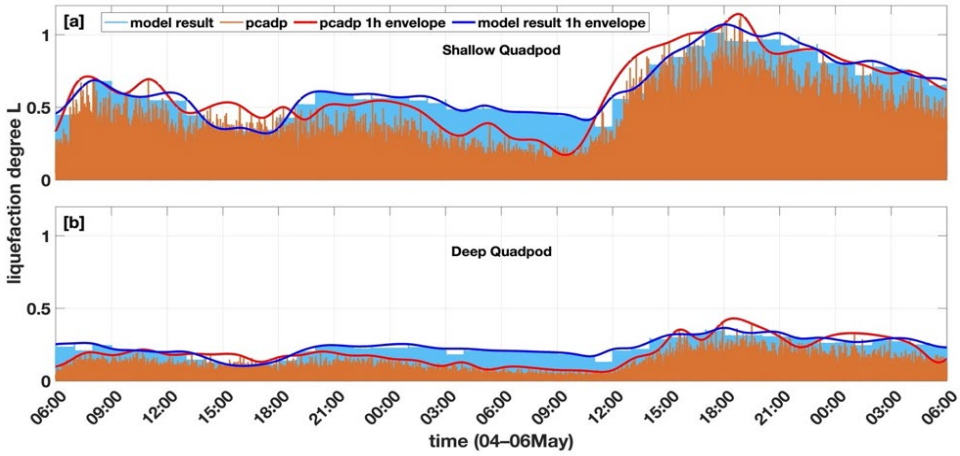

Liquefaction degree (L) time series at (a) shallow and (b) deep quadpod locations. L computed from model output and observation are represented in blue and red. The thick blue and red lines denote the peak envelope of L over local maxima for each 1-hour interval. $L \geq 1$ indicates the occurrence of liquefaction.

Figure 32. Liquefaction degree (L) time series at shallow and deep quadpod locations

The liquefaction degree and depth failure were calculated over the model domain area using the pressure field estimated from the model results, allowing seafloor instability to be mapped and locate areas in which liquefaction occurred. Figure 33a presents the map with maximum L distribution during the first wave event, with maximum L ranging between 0.3 near the deep quadpod location and 0.75 around the shallow quadpod location. During the second wave event (Figure 33b), L varies from 0.4 near the deep quadpod location to 1.1 near the shallow quadpod location. A failure depth map during the second wave event (Figure 33c) is zoomed in around the shallow quadpod

location to identify the area where liquefaction occurred ($L \geq 1$). Results indicate a maximum failure depth of 0.24 m and a failure depth of 0.1 m at the shallow quadpod location. The failure depth and L negatively correlate with local depth, with a correlation coefficient (R) of -0.6 and -0.62, respectively. Higher L and failure depth values are related to shallow areas, which affects the shape of lines with the same L and failure depth values (see Figure 33).

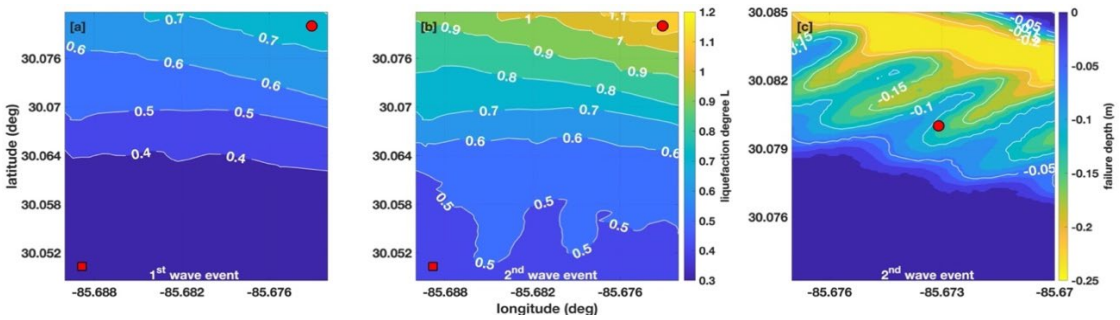

Liquefaction degree (L) map computed from model output during the (a) first wave event and (b) second wave events. $L \geq 1$ indicates the occurrence of liquefaction. (c) Failure depth map computed from model output during the second wave event and zoomed in around the shallow quadpod location. Deep and shallow quadpod locations are denoted by the red square and red dot, respectively.

Figure 33. Liquefaction degree (L) map computed from model output

D. DISCUSSION

1. Impact of Waves and Currents on Morphological Changes

The impact of currents and waves on morphological changes is assessed by comparing (Figure 34) dimensionless Shields parameters for both currents (θ_c) and waves (θ_w) to the critical Shields parameter (θ_{th}), similarly to van Dijk and Kleinhans (2005) and Damen et al. (2018). The θ_c and θ_w presented in Figure 34 are computed using the model output at the quadpod location. The critical value θ_{th} is determined as a function of the non-dimensional grain size, as pointed out by van Rijn (1993), and used as a threshold for initial sediment motion (Shields 1936). Shields parameter and shear stress for currents (τ_c) and waves (τ_w) are calculated as discussed by van Rijn (1993):

$$\theta = \frac{\tau}{(\rho_s - \rho_w) g D_{50}} \tag{22}$$

$$\tau_c = \rho_w g \left[\frac{u_c}{18 \log_{10} \left(\frac{12d}{2.5 D_{50}} \right)} \right]^2 \tag{23}$$

$$\tau_w = \rho_w u_{orb}^2 \exp\left[5.213 \left(\frac{2.5 D_{50}}{A_{orb}} \right)^{0.194} - 5.977 \right] \tag{24}$$

where ρ_s is the density of the sediment, ρ_w is the density of salt water, g is the gravitational acceleration, d is the local depth, u_c is the current velocity, u_{orb} is the wave orbital velocity, and A_{orb} is the wave orbital excursion near bed. Figure 34 show that θ_c is less than θ_{th} during the entire period, which is consistent with the relatively weak u_c with mean of 0.08 m/s and peak of 0.21 m/s. However, θ_w surpasses the threshold during the wave events, suggesting the waves are responsible for the sediment transport.

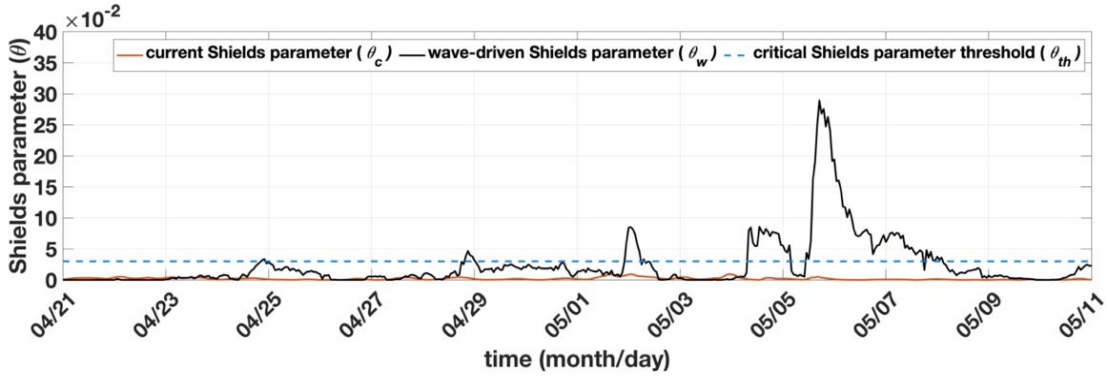

Wave-driven Shields parameter (θ_w) and current Shields parameter (θ_c) time series. The blue dashed line represents the critical Shields parameter (θ_{th}) for initiation of sediment motion.

Figure 34. Shields parameter time series

2. Tide Stations and Observed Sinking of the Shallow Quadpod

During the field experiment, the NOAA station 8729210 in Panama City Beach was unavailable. Therefore, station 8729108 in Panama City Marina on St. Andrew Bay,

approximately 8 km from the shallow quadpod location, is the nearest station to the study area (Figure 26). The tidal time delay between station 8729108 and quadpods was determined from the slope of the cross-spectrum phase (Bendat and Piersol 2012). Therefore, a time delay of 17 minutes was applied to eliminate phase differences and determine the water level difference between station 8729108 and quadpods to evaluate the seafloor elevation gain during the two wave events (Figure 31b) owing to the sediment accretion or sinking of the shallow quadpod.

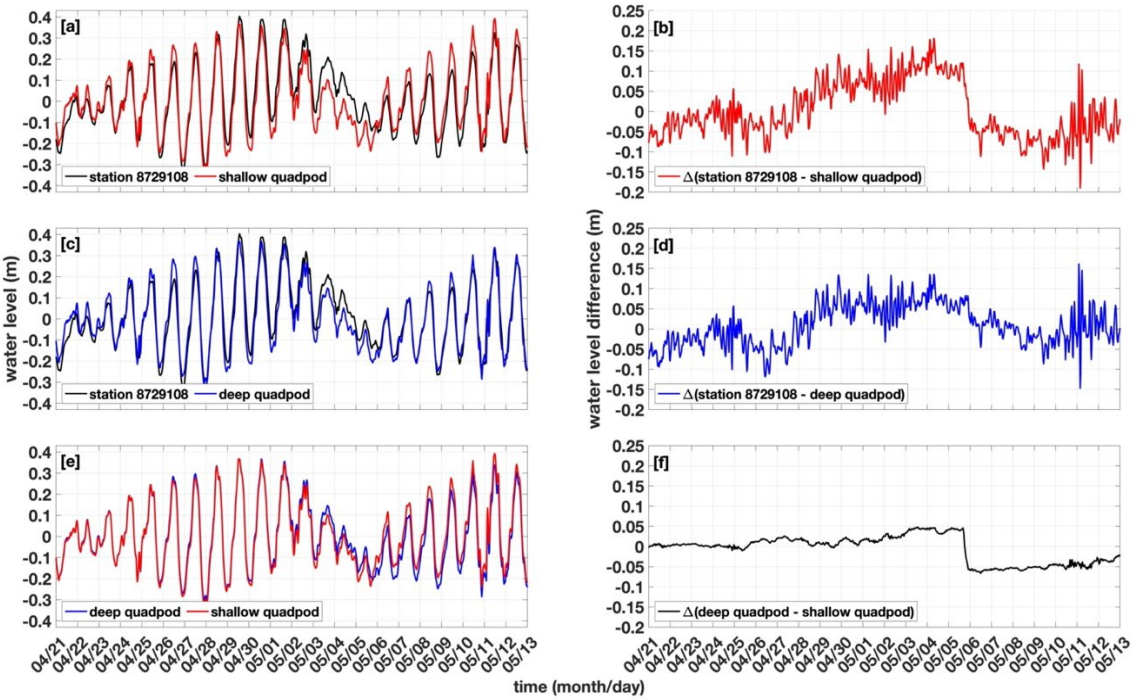

Comparison between the observed water level relative to local mean sea level at station 8729108, shallow quadpod, and deep quadpod (a, c, and e), and respective water level difference (b, d, and f). Water level observations are sampled at 30-minute intervals and time delay adjusted.

Figure 35. Water level difference between stations

Figure 35 shows the comparison of the water level relative to the local mean sea level sampled at 30-minute intervals (on the left) and the water level difference between station 8729108 and quadpods (on the right). A sudden rise in water level at shallow quadpod location was observed between 5–6 May (second wave event), which was not

followed by a rise in water level at station 8729108 (Figure 35a) or deep quadpod location (Figure 35e). This water level offset between shallow and deep quadpod (Figure 35f), estimated at 0.1 m, is also observed between station 8729108 and shallow quadpod (Figure 35b), indicating the shallow quadpod settled 0.1 m into the sandy seafloor. The rapid sinking of the shallow quadpod associated with storm-driven waves suggests the occurrence of seafloor liquefaction. In contrast, station 8729108 and deep quadpod (Figure 35d) show good agreement before and after the storm, suggesting the deep quadpod did not sink into the seafloor, consistent with observations that presented no variation on seafloor elevation at the deep quadpod location (not shown).

The shallow quadpod sinking occurred concurrently with the second seafloor elevation gain of 0.1–0.15 m (Figure 31b) during the second wave event, indicating that the seafloor elevation gain was caused primarily by the shallow quadpod sinking of 0.1 m into the sediment, reducing the distance between the PC-ADP and the seafloor. This result is consistent with Klammler et al. (2021), which reported the settling of the shallow quadpod during the second wave event and employed a poroelastic wave-sediment interaction model to estimate the sinking by 0.1 m, but also acknowledged the uncertainty about the contributions of other morphological processes to the seafloor changes indicated by the PC-ADP and pencil beam sonar.

3. Factors Impacting Liquefaction

Figure 36 depicts the variation of L and failure depth with respect to depth, dissipation of wave energy, and failure depth, as well as the wave steepness (H_s/ wavelength) and failure depth with respect to relative water depth (depth/wavelength) using the model output during the second wave event. Figure 36a indicates failure depth occurrence in areas shallower than 9.5 m, which can be identified by the points above the threshold line of L =1 and the peak of L occurring around 4 m depth. However, L and failure depth decrease in depths shallower than 4 m. From 4 m depth, the dissipation of wave energy increases at a greater rate towards the shore, as shown in Figure 36b, in which failure depths decrease when the dissipation of wave energy is greater than 40 N/ ms. Furthermore, relative water depth is a prominent feature, with failure depth

decreasing as relative water depth increases, and no liquefaction is predicted for relative water depths greater than 0.25 (Figure 36c). Although not as evident as relative water depth influence in Figure 36c, wave steepness affects liquefaction, with greater failure depth associated with greater wave steepness.

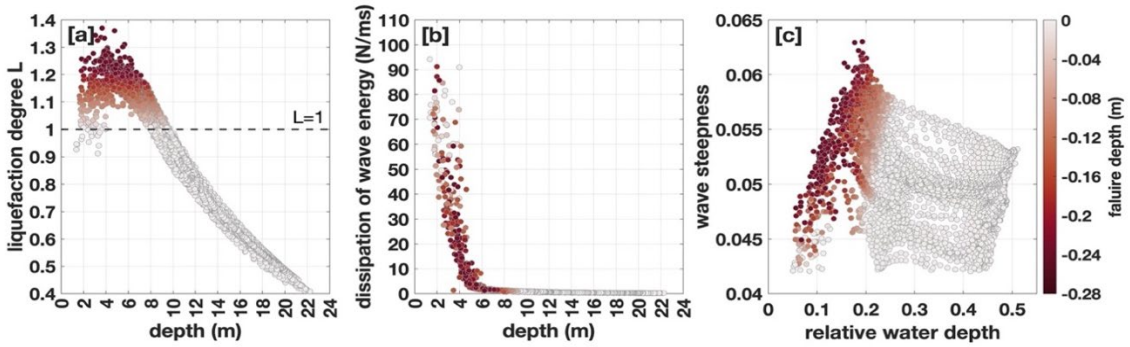

Scatter plots of (a) liquefaction degree (L) and depth, (b) dissipation of wave energy and depth, and (c) wave steepness and relative water depth. Colors denote the failure depth as scale on the right panel (c). The black dashed line on panel (a) represents $L = 1$. Scatter plots consider model output during the second wave event.

Figure 36. Scatter plots of liquefaction degree (L), depth, dissipation of wave energy, wave steepness, and relative water depth

Wave-induced liquefaction occurred during the second wave event, with the shallow quadpod sinking coinciding with the peak of L and consistent with the estimated failure depth (0.1 m). Throughout this time, objects were only partially buried. However, according to sonar images, the total burial of objects occurred on 6 May, beyond the time of peak L values, implying that other processes contributed to the complete burial of objects. In addition, results from the Delft3D model indicate the maximum sediment accretion at the shallow quadpod location occurred after the second wave event, suggesting the storm generated favorable environmental conditions to develop the seafloor liquefaction and sediment accretion.

E. CONCLUSION

A coupled hydro-morphodynamic and wave-induced liquefaction model is used to investigate seafloor evolution and liquefaction. The model was validated against observations from a field experiment off the coast of Panama City, Florida. Comparisons of the water level difference between the NOAA station 8729108 and quadpods and the seafloor elevation from the pencil beam sonar and PC-ADP maximum backscatter indicate that the shallow quadpod settled into the sandy sediment 0.1 m during the second wave event on 5–6 May due to wave-induced liquefaction. During the first wave event, no liquefaction was observed. Furthermore, sector scanning sonar observations show the burial of three objects (8.1 and 15.5 cm in diameter) deployed near the shallow quadpod after the second wave event, suggesting the contributions of other morphological processes in the observed burial of objects. The model result denotes a sediment accretion of up to 0.05 m near the shallow quadpod, which is attributed to sediment transport driven by wave action. In addition, increases in the Shields parameter calculated from the model results were associated with wave events, which occurred at sharp increases in observed backscatter of the water column, suggesting that waves largely enhance sediment transport near the shallow quadpod location.

Liquefaction degree calculated from the model output and observations indicate that sediment failure occurred near the shallow quadpod during the second wave event when the shallow quadpod settled into the sediment. A liquefaction degree map was computed from the model output, showing areas with a higher likelihood of seafloor instability and the predicted failure depth in areas where the liquefaction may occur. Moreover, the relative water depth presented a prominent influence on the failure depth, with no liquefaction expected for relative water depths greater than 0.25.

These results are consistent with the hypothesis that both liquefaction and sediment accretion occurred during the field experiment. Furthermore, it builds upon previous research by allowing morphological evolution and liquefaction analyses to be conducted throughout the area of interest rather than being constrained by the location of observation stations, which has important implications for seafloor instability study and object burial during stormy conditions.

THIS PAGE INTENTIONALLY LEFT BLANK

IV. OBSERVATIONS AND 3D MODEL SIMULATION OF SAND WAVE MIGRATION IN SHALLOW WATER ENVIRONMENT

This chapter was submitted to *International Journal of Sediment Research* for publication (12 August 2022) with minor formatting changes. Co-authors include Vinícius S. Pessanha[7], Peter C. Chu,[7] Matt K. Gough[7], Peter Traykovski,[8] and Mara M. Orescanin[7].

A. INTRODUCTION

In shallow waters, bedforms created by tidal currents or surface waves are commonly observed on the sandy seabed. The spatial scale of these coastal bedforms varies from ripples with characteristic wavelengths and heights of several centimeters to sandbanks with wavelengths of several kilometers and heights up to 30 m (Wang et al. 2019). Sand waves are bedforms in an intermediate spatial scale with wavelengths of hundreds of meters, migration speeds in the order of tens of meters per year, and wave heights of several meters (Besio et al. 2004). They are typically found in regions with tidal currents larger than 0.5 m/s, such as the North Sea (Damen et al. 2018; Krabbendam et al. 2021), Taiwan Strait (Boggs 1974), Argentine coast (Aliotta and Perillo 1987), United States coast (Barnard et al. 2006; Xu et al. 2008; Jones and Traykovski 2019), South China Sea (Li et al. 2011), and Barents Sea (Bellec et al. 2019).

In addition, migrating sand waves may impact human activities by reducing the depth of navigation channels, exposing submarine cables, interacting with pipelines and wind power stations, and causing burial/migration of seabed munition (Besio et al. 2008; Chu et al. 2021, 2022). Therefore, the study of sand wave characteristics is essential and traditionally carried out by analyzing historical field data, which might be improved by morphodynamic models examining the sand wave behavior (Tonnon et al. 2007).

[7] Department of Oceanography, Naval Postgraduate School.

[8] Department of Applied Ocean Physics and Engineering, Woods Hole Oceanographic Institution.

Hulscher (1996) introduced a linear model to explain the formation of sand waves, in which the interaction of tidal current with the seabed generates morphological instabilities and causes sand waves to develop. According to this model, the oscillation of tidal current over seabed perturbations generates recirculation cells in the vertical plane, inducing sediment transport with flow diverging at the troughs and converging at the crests. The gravitational effect induces the sediment transport down slope, balancing the sand wave growth. Németh et al. (2002) and Besio et al. (2004) added a residual current in the oscillatory tidal current presented in the Hulscher (1996) model. Their results show that the sand wave migration is generated by flow asymmetry in regions where the ebb flow is stronger than the flood flow or vice versa. Leenders et al. (2021) provided a detailed overview of several physical processes and contributions added to the model proposed by Hulscher (1996). Nevertheless, linear models are only applicable for the early stages of tidal sand wave development. Therefore, models including non-linear effects are demanded to investigate the long-term behavior of sand waves. Models, such as the one presented by Blondeaux and Vittori (2016), which included a process-based model and an empirical approach, produce good results, even though the entire evolution of sand waves over time cannot be resolved due to the lack of coupling between hydrodynamics and morphodynamics (Krabbendam et al. 2021). Campmans et al. (2018) proposed a nonlinear model to study the effects of wind and surface waves on sand wave development, assuming monochromatic waves, a constant vertical eddy viscosity, and neglecting bed load transport and wave-current interactions. They concluded that wind and surface waves decrease sand wave height and increase migration during storms. Moreover, numerical process-based models were designed to study the characteristics, processes affecting, and long-term dynamics of sand waves (e.g., van den Berg et al. 2012 and Németh et al. 2007). However, these studies were limited by highly idealized parameters such as initial sinusoidal bathymetry, simplified tidal forcing, and simplified equations to estimate sediment transport and turbulence.

The usage of a process-based Delft3D morphodynamic model (Lesser et al. 2004) has arisen as an option to study sand wave dynamics by including many processes. For example, models by Borsje et al. (2013) and Borsje et al. (2014) examined the role of

turbulence formulation and the suspended sediment load, representing the initial stage of sand waves satisfactorily compared with field observations. In addition, van Gerwen et al. (2018) considered the effects of suspended sediment load and tidal asymmetry, indicating that both cause reduction in sand wave heights. Wang et al. (2019) showed that bed slope is essential to model the wavelength and migration of sand wave, analyzing sand waves under various tidal forcing combinations and sediment sizes. Moreover, Damveld et al. (2020) studied sediment sorting patterns in sand waves, showing the influence of tidal asymmetry in sediment distribution. Krabbendam et al. (2021) used a Delft3D model to successfully hindcast and forecast observed sand waves using realistic bathymetry. Furthermore, Leenders et al. (2021) investigated the migration of sand waves toward the top of a sandbank driven by the tidal flow modified by the sandbank topography. The use of an advanced morphodynamic model allows the study of sand waves in a more realistic scenario, reducing the number of simplifications that limit the performance of the models previously.

Recently, Jones and Traykovski (2019) reported the migration of bedforms observed during a field experiment near the southeastern corner of Martha's Vineyard, Massachusetts. Bathymetric surveys and fixed rotary sidescan sonar data showed sand waves with mean migration speed of 50 cm/day while rotating counterclockwise. In addition, they presented a conceptual model to predict sand wave migration speed and describe the dynamics of the interaction of smaller megaripples with larger sand waves. The model performed well in tidally dominated flows. However, it is limited to periods of minimal wave energy because the model neglects the effect of surface waves.

Previous studies were mainly constrained by simplified bathymetry, the 2DV approach, and idealized parameters. Additionally, there is a dearth of studies in regions with shallow depths in particular on the physical processes that impact rapid migrating sand waves. Therefore, this paper supplements the previous work (Jones and Traykovski 2019) by implementing a Delft3D model (three-dimensional [3D] approach) to reproduce the local hydro-morphodynamic, considering the bathymetry, tidal forcing, winds, and surface waves observed during the experiment. In addition, using a data-modeling

approach, this paper investigates the physical processes causing the high migration speed and the rotational aspect of sand waves.

B. MATERIALS AND METHODS

1. Study Area and Field Experiment

The study area is in a region with strong tidal currents and intermittent energetic wave events at Wasque Shoals, about 1 km from the southeastern corner of Martha's Vineyard, Massachusetts (Figure 37). Currents in this region are dominated by the M2 and N2 semidiurnal tidal currents, which are responsible for roughly 80% and 10% of the variance, respectively (Hopkins et al. 2017). Surface wave direction during the field experiment primarily ranges between the south and southwest. Significant wave height, the highest one-third of waves, decreases with decreasing water depth, which indicates reduced wave energy due to wave breaking on the shallow shoals in the south of the study area (Traykovski and Austin 2017). Wasque Shoals is characterized by a sandy seabed and tidal currents exciding 1 m/s with direction predominantly east–northeast and west during the flood and ebb, respectively. According to Hopkins et al. (2017), the ebb jet splits from the sharp shoreline around the southeastern corner of Martha's Vineyard, which reduces the ebb flow in the area of interest and creates an asymmetric flow pattern with a dominant flood. The complex bathymetry, with depth varying from 2 to 7 m, includes periodic bedforms such as megaripples and sand waves. On the shoals, tidal sand wave heights range from 2 to 4 m (Traykovski and Austin 2017).

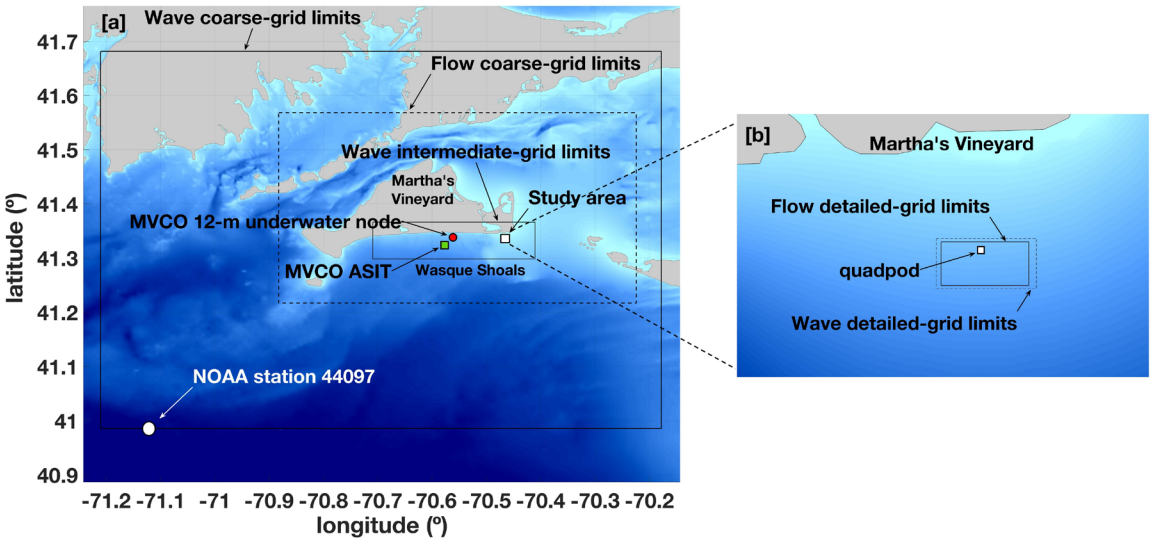

(a) Wave coarse-grid area (thick solid lines), flow coarse-grid area (dashed lines), wave intermediate-grid area (thin solid lines) with the NOAA station 44097 represented by the white dot at the southern boundary of the wave coarse-grid area (40.967° N, 71.126° W), the red dot for the location of the MVCO 12-m underwater node (41.3366° N, 70.5564° W), the green square for the MVCO ASIT at 41.325° N, 70.567° W, and the white marker for the study area. (b) Zoomed-in study area with wave detailed-grid area (dashed lines), flow detailed-grid area (thin solid lines), and the white square at 41.3404° N, 70.459° W for the quadpod of the field experiment.

Figure 37. Study area and limits of model grids

During the field experiment, sand wave migration was observed at the same time as surface waves, and currents. A metal structure, called a quadpod, was deployed on 20 November 2013 (white square in Figure 37b shows its location (41.3404° N, 70.459° W)) in a water depth of approximately 6.5 m (Figure 38). A Nortek Aquadopp sensor was placed on the quadpod with 0.2 m vertical bin measured velocity over a range of 2 m, which were used to compute the hourly mean depth-averaged current velocity. Furthermore, significant wave height, mean wave direction, and peak wave period were estimated from pressure sensors of the acoustic Doppler velocimeters (ADVs) attached to the quadpod. See Traykovski and Austin (2017) and Jones and Traykovski (2019) for detailed instrumentational information.

In addition, two bathymetric surveys were conducted at the beginning (16 October 2013) and ending (10 January 2014). Bathymetry was measured using an autonomous

water jet drive kayak, Jetyak (Kimball et al. 2015), equipped with a 200 kHz echo sounder and a Post-Processed Kinetic (PPK) GPS system with horizontal and vertical resolution within 2–3 cm and 3–5 cm, respectively. The surveys covered an area of 400m×800m with track lines spaced 30 m from each other. The initial and final bathymetric maps (Figure 38) show the migration of a Y-shaped sand wave, herein just called the sand wave, over the quadpod located in the trough and represented by the white dot. The sand wave migrated towards the northeast, burying the quadpod on the same date as the final bathymetry (Jones and Traykovski 2019). Moreover, the bathymetric surveys show that the sand wave has a higher migration speed in the southern portion than the northern portion and indicates counterclockwise rotation of the sand wave.

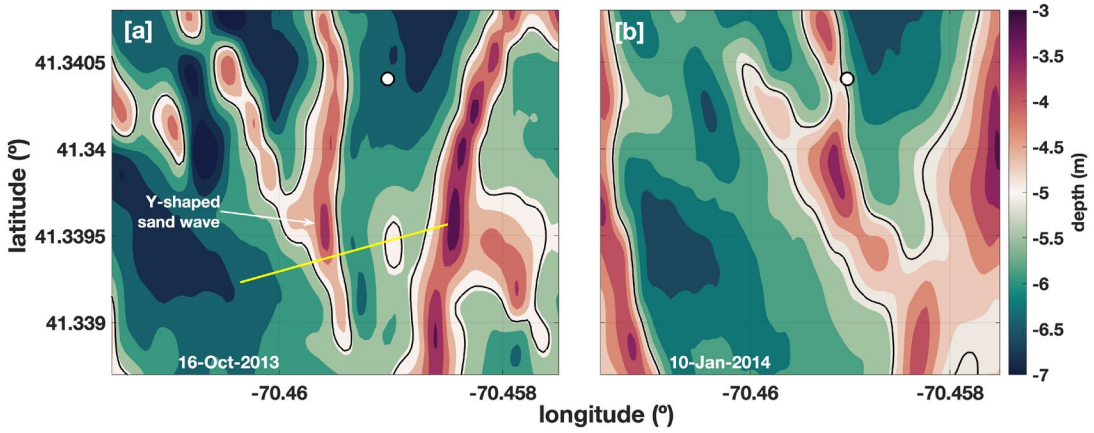

Bathymetric data from the survey performed on (a) 16 October 2013 and (b) 10 January 2014. The white dot demarks the position of the quadpod and the black curve represents the 5 m depth. The yellow line illustrates the transect (160 m length) used to calibrate the model.

Figure 38. Bathymetry in the study area

2. Model Approach and Set-up

The open-source modeling system Delft3D was implemented in the Wasque Shoals area. It is a process-based model, based on shallow water approximation, capable of examining the impact of waves, currents, and sediment transport on morphological evolution. The Delft3D model has three modules: flow, wave, and morphology. The flow module forecasts water level, currents, feeds current data into the wave and morphology

modules as input, computes sediment transport, and updates bathymetry under wind and tidal forces. With inputs such as water level, bathymetry, wind, and currents from the flow module, the wave module predicts wave generation, propagation, dissipation, and non-linear wave-wave interactions in the nearshore environment. Finally, the morphology module works in a cycle with the wave and flow modules to update the bathymetry while taking into account the sediment transport field. The flow field is likewise influenced by waves and morphological changes since the modules are online coupled. Lesser et al. (2004) and the Delft3D user manual (Deltares 2022a) provide more information on the model description.

The model comprises two domains coupled using the offline nesting modeling approach to improve the spatial resolution in the area of interest (Figure 37). In this method, the overall domain (coarse resolution) is modeled to provide (offline) boundary conditions for the nested domain (finer resolution). Once the boundary conditions have been created, simulations using the nested domain can be run independently of the overall domain, reducing the computational cost.

The overall domain uses the two-dimensional horizontal (2DH) model approach with one vertical layer (depth-averaged mode). The flow coarse grid (Figure 37a), with a resolution varying from 1 km to 40 m (in the study area), stretches 40 km north and south and 55 km east and west. The wave coarse grid (86 km in the north-south direction and 80 km in the east-west direction) has a resolution of 1 km, the wave intermediate grid resolution is 200 m, and the wave fine grid resolution is 40 m. Similar to Roelvink and Walstra (2005), the wave model grids cover a larger area than the flow grids preventing boundary disturbances of the wave model from entering the flow domain. In addition, the boundary conditions of the overall domain were defined at the outer boundaries of the flow coarse grid and driven by tidal water level variations calculated using the global inverse solution from altimetry data (Egbert and Erofeeva 2002) with the 13 main astronomic constituents, including M2, S2, N2, K2, O1, and K1. The significant wave height, wave period, wave directions, and directional spreading were used to create wave boundary conditions based on observations from NOAA buoy station 44097, located in the 50-m water depth (Figure 37a). On all open boundaries (wave coarse grid), these

parameters were applied uniformly. Moreover, bathymetric data from the U.S. Coastal Relief Model (NOAA/NGDC 1999), with 90 m resolution, were used in the overall domain that was not covered by the bathymetric survey conducted during the field experiment. The time step was chosen at 9 seconds based on the Courant–Friedrichs–Lewy (CFL) number. Default values of the Delft3D model were applied for the Chézy bottom roughness (65 $m^{1/2}/s$) and horizontal eddy viscosity (1 m^2/s). In addition, the flow and wave module coupling time was adjusted to 60 minutes. The bottom friction component of wave dissipation with constant bottom friction was calculated using the JONSWAP model (Hasselmann 1974). Additionally, the depth-induced breaking (Battjes and Janssen 1978) was adjusted to α equal to 1 and γ equal to 0.73 (default values).

The detailed domain employs the 3D model approach to examine the sand wave dynamics affected by three-dimensional processes. The flow detailed grid (Figure 37b) covers the study area with 8 m horizontal resolution and 20 non-equidistant vertical σ-layers, with resolution in terms of the percentage of the water depth. The first five layers (closer to the seabed) have the highest resolution, 2% of the water depth. The following 12 layers have a resolution of 5%, and the last three layers (closer to the surface) have a resolution of 10% of the water depth. The model used the Riemann boundary conditions on the four open boundaries at the detailed domain to include tidal current, allowing the outgoing waves to pass the open boundary without reflecting back into the computational domain (Verboom and Slob 1984). The sediment transport, including bed load and suspended load transport, and morphological evolution were computed only in the flow detailed grid to allow the comparison with field measurements. Default values of the Delft3D model were applied for the initial bed of sediment (5 m), initial water level (zero m), and a spin-up interval (720-minute) to avoid any impact from an initial hydrodynamic instability on the bottom change computation. The eddy viscosity was computed using the k-ε turbulence model. Moreover, data from the bathymetric survey conducted on 10 October 2013 was set as initial bathymetry. Based on the CFL number, a time step of 6 seconds was established. The sand was chosen as the sediment type, with a median grain size (D_{50}) of 500 μm (Hopkins et al. 2018) and a sediment-specific density of 2,650 kg/m^3. The wind input files were set up using observations from the Air-Sea Interaction

Tower (ASIT), Martha's Vineyard Coastal Observatory (MVCO: https://mvco.whoi.edu), located 3 km south of Martha's Vineyard in 17-m depth (Figure 37b).

3. Simulation Design and Model Performance Assessment

The simulation was designed to hindcast the (Y-shaped) sand wave dynamic observed during the field experiment, which presents a high migration speed and counterclockwise rotation. First, the model was calibrated and validated. Then the possible factors influencing the local morphodynamics were analyzed from simulations considering the inclusion and absence of surface waves and wind.

The performance of the model simulating the local hydrodynamics is assessed by comparing model output variables with observations through the root mean square error (RMSE). Let X be the variable of interest (e.g., significant wave height), X_{mod} be the model output, X_{obs} be the observation, N be the number of observations, and $\langle X \rangle$ be the time mean.

$$RMSE = \sqrt{\frac{1}{N}\sum\left(X_{\mathrm{mod}} - X_{obs}\right)^2} \tag{25}$$

Besides, model performance is also evaluated using the skill score (SS) defined by

$$\mathrm{SS} = 1 - \left(\sum \left|X_{\mathrm{mod}} - X_{obs}\right|^2\right) \Big/ \left[\sum\left(\left|X_{\mathrm{mod}} - \left\langle X_{obs}\right\rangle\right| + \left|X_{obs} - \left\langle X_{obs}\right\rangle\right|\right)^2\right] \tag{26}$$

to represent the model prediction skill (Willmott 1981) with SS = 1 for complete agreement between model output and observations and SS = 0, on the other hand, for total disagreement.

The Brier skill score (BSS) was used to evaluate the ability of the model to represent the morphological changes, as established by van Rijn et al. (2003)

$$BSS = 1 - \left[\left\langle\left(\left|z_{b,c} - z_{b,m}\right| - \Delta z_{b,m}\right)^2\right\rangle \Big/ \left\langle\left(z_{b,0} - z_{b,m}\right)^2\right\rangle\right], \tag{27}$$

where $z_{b,c}$ is the computed bed level, $z_{b,m}$ is the measured bed level, $z_{b,0}$ denotes the initial bed level, and $\Delta z_{b,m}$ is the uncertainty of the measured bed level, here assumed to be 0.05 m. The qualification of the performance of the model suggested by van Rijn et al. (2003)

is excellent as a BSS between 1 and 0.8, good between 0.8 and 0.6, reasonable/fair between 0.6 and 0.3, poor between 0.3 and 0, and bad when less than 0.

C. RESULTS

1. Model Calibration

The model results using the set-up described in Section B.2 were compared to the MVCO 12-m underwater node observations for a period of one month. Figure 39 indicates a good model-data agreement for mean water level (*MWL*), significant wave height (H_s), and mean current velocity (*V*), with positive values of *V* representing the flow moving in the flood tide direction and negative values the flow moving in the ebb tide direction. Since the model produced satisfactory results for *MWL* (SS=0.988), *V* (SS=0.971), and H_s (SS=0.959), calibration was performed with regard to morphology.

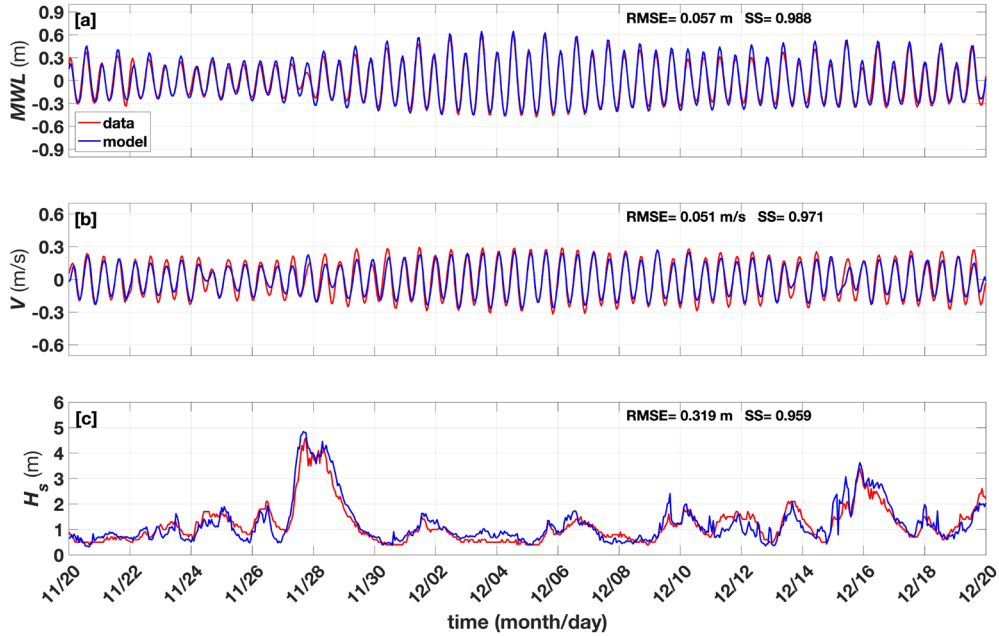

Comparison between model results (blue) and observations at the MVCO 12-m underwater node (red) for (a) mean water level (*MWL*), (b) depth-averaged current (*V*) with positive values indicating the flow moves in the flood tide direction and negative values denoting the flow moves in the ebb tide direction, and (c) significant wave height (H_s). The root mean square error (RMSE) and skill score (SS) for each comparison are provided in the upper right of the panels.

Figure 39. Model calibration for hydrodynamics

The calibration was conducted by adjusting the bed slope parameter (α_{BS}). This parameter accounts for the effect of the bed slope in bedload transport and must be calibrated to adequately predict sand wave migration (Wang et al. 2019). Higher values of α_{BS} produce a stronger bed slope effect, decreasing upslope and increasing the downslope sediment transport. The model result was compared with observed bathymetry along the calibration transect (160 m length) depicted in Figure 38, which is oriented in the mean flow direction. The parameter α_{BS}=0.2 achieved the best result with BSS=0.916. Figure 40 shows the model result for different values of α_{BS} (0.1, 0.2, 0.5, and 1) considering the observed bathymetry and summarizes the results along the calibration transect.

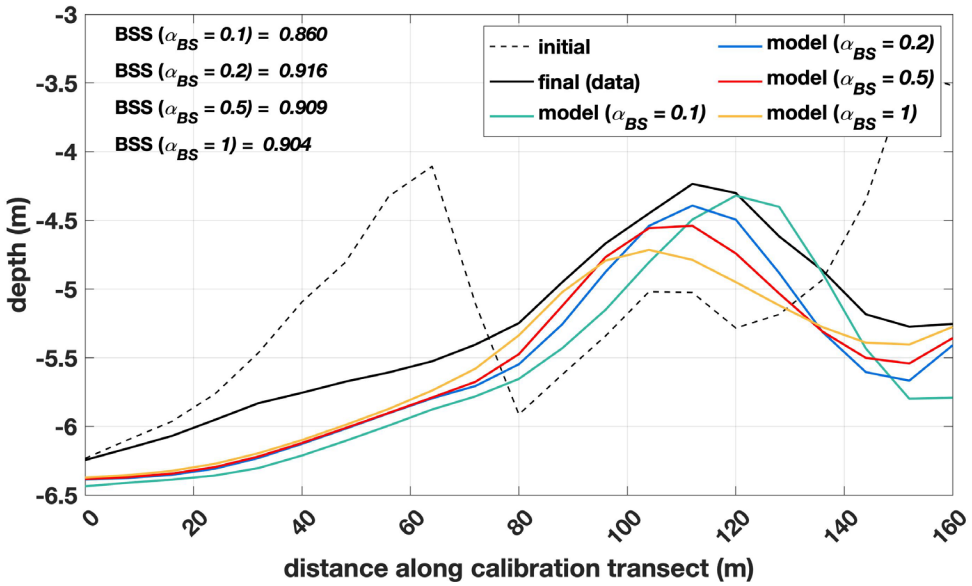

Bed level profiles along the calibration transect (shown in Figure 38). Comparison between model results for different values of bed slope parameter α_{BS} (0.1, 0.2, 0.5, and 1) and observed bathymetry. The Brier skill score (BSS) for each model result in comparison with the observed bathymetry is provided in the upper left of the panel.

Figure 40. Model calibration for morphology

2. Model Validation

The *MWL*, *V*, and H_s observed at quadpod location were compared with the model output for a period of 50 days (Figure 41). The *MWL* was predicted by the model (Figure 41a) with the calculated SS (0.979) and RMSE (0.066 m). In Figure 41b, *V* is represented by positive values when the flow moves in the flood tide direction and negative values when the flow moves in the ebb tide direction. The SS of *V* was calculated as 0.816 and the RMSE as 0.074 m/s. For H_s (Figure 41c), the SS was calculated as 0.962 and the RMSE as 0.131 m.

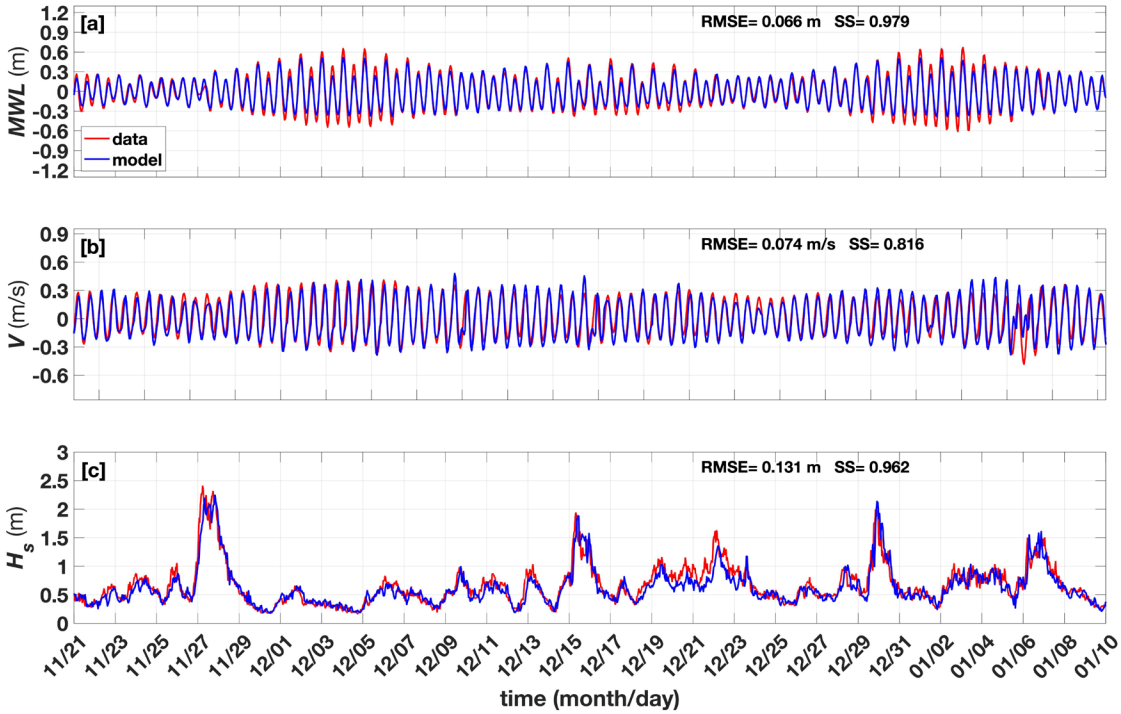

Comparison between model results (blue) and observations (red) at the quadpod location for (a) mean water level (*MWL*), (b) depth-averaged current (*V*) with positive values indicating the flow moves in the flood tide direction and negative values denoting the flow moves in the ebb tide direction, and (c) significant wave height (H_s). The root mean square error (RMSE) and skill score (SS) for each comparison are provided in the upper right of the panels.

Figure 41. Model validation for hydrodynamics

In order to qualitatively assess the model results, the bathymetric changes were calculated by subtracting the initial bathymetry from the observed and simulated final bathymetry. Figure 42 presents the respective observed and simulated bathymetric change maps showing the location of sediment accretion (in yellow) and erosion (in blue). The model result closely reflects the observed pattern of changes, with erosion in the areas where sand wave crests existed and sediment deposition in the areas where the initial bathymetry presented troughs.

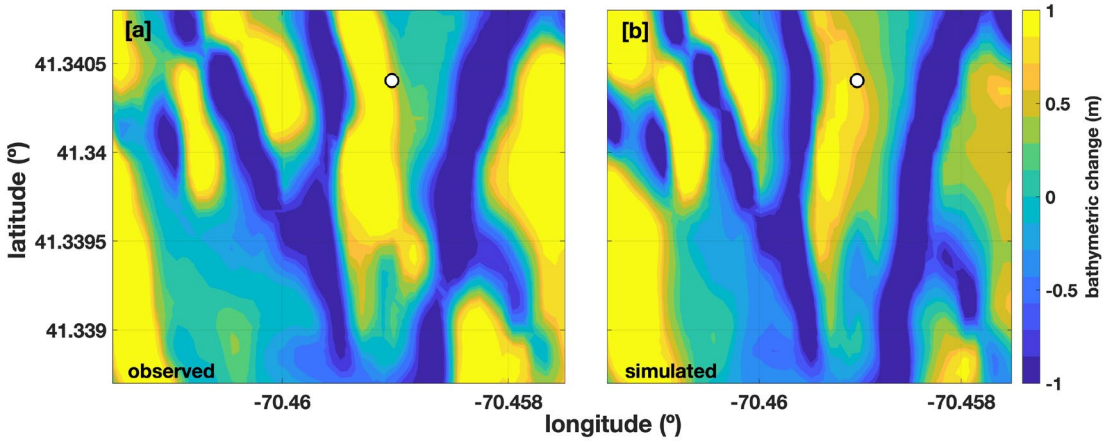

(a) Observed and (b) simulated bathymetric change considering the difference between the initial (16 October 2013) and final (10 January 2014) bathymetry. Yellow is sediment accretion, and blue is erosion. The white dot demarks the position of the quadpod.

Figure 42. Observed and simulated bathymetric change

Furthermore, the model performance was evaluated by comparing simulated and observed final bathymetry along seven transects (Figure 43a). These parallel transects are oriented in the mean flow direction and separated by 20 m from each other. Each transect is 160 m long and composed of 21 points equally spaced by 8 m (model spatial resolution), totaling 147 points considering all transects. Figure 43b shows a scatter plot comparing the observed and predicted depth for these 147 points. The model adequately simulated the seabed evolution with a mean BSS of 0.862 (considering all transects).

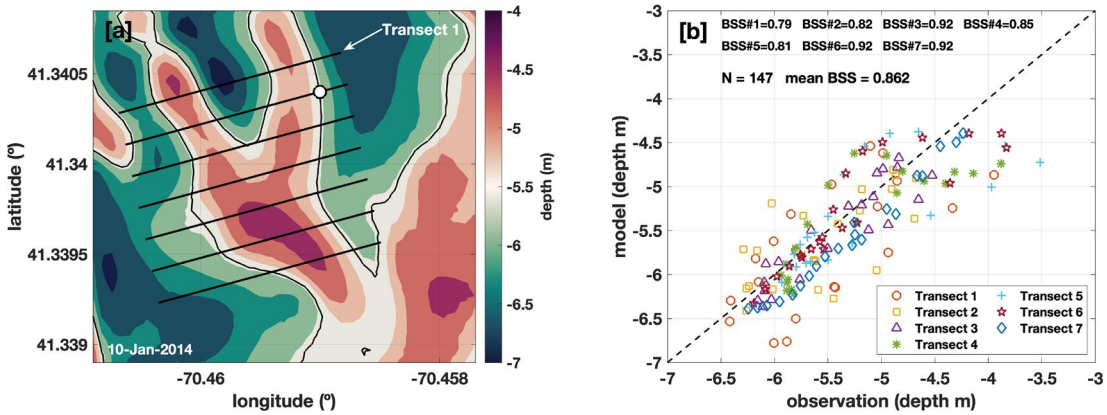

Bed level from the model result for (a) the final bathymetry (10 January 2014). The seven transects and the quadpod location are represented by the black lines and white dot, respectively. (b) Scatter plot presenting the modeled and observed bathymetry on 10 January 2014. The 1:1 ratio line is represented by the black dashed line. The Brier skill score (BSS) for model results in comparison with the observed bathymetry for each transect is provided in the upper panel (b), as the number of points considered and the mean BSS.

Figure 43. Model performance for morphology

3. Sensitivity Studies

Comparison between observed and simulated bed level profiles along transect 3 was carried out to determine the impact of surface waves and winds on sand wave migration. A reference model run, referred to as case I, accounts for tidal, wave, and wind forcing with parameters as described in Section B.2. A subsequent model run, case II, considers only tidal and wind forcing (without surface waves). Finally, case III includes tidal and wave forcing (without wind). Figure 44 presents the bed level profiles for transect 3 with the initial bed level as a dashed black line; the final observed bed level profile as a black line; and case I, case II, and case III final bed level profiles as blue, yellow, and red lines, respectively. Sand wave migration was to the right (northeast direction), with mean migration of 36 m. For the simulation without surface waves (case II), the model results show approximately 65% less sand wave migration relative to case I, indicating that surface waves play an important role in sand wave migration in the study area. Moreover, the results for the simulation without wind (case III) indicate

approximately 15% more migration, implying that wind forcing reduces the sand wave migration during the experiment.

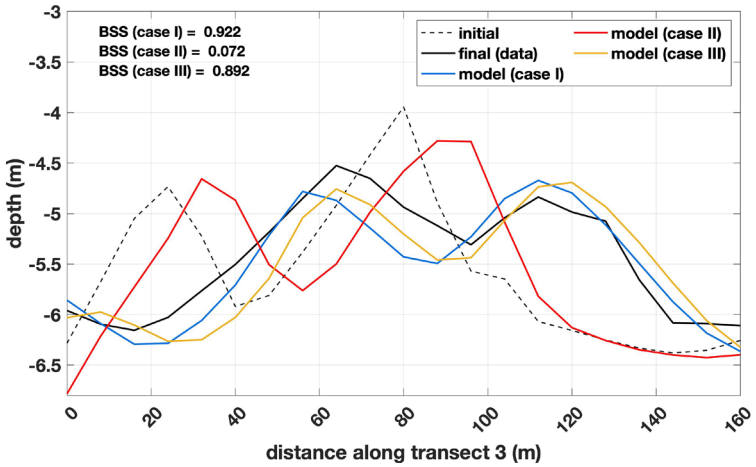

Bed level profiles on 10 January 2014 along transect 3. The lines represent the model result for case I, including tidal, wave, and wind forcing (blue line); case II, including tidal and wind forcing (yellow line); and case III, including tidal and wave forcing (red line). The black dashed line represents the initial bed level on 16 October 2013 and the solid black line denotes the observed final bathymetry on 10 January 2014.

Figure 44. Bed level profiles along transect 3 for cases I, II, and III

D. DISCUSSION

1. Tidal Flow Asymmetry, Wind, and Surface Waves

The tidal flow asymmetry is essential for sand wave migration. The recirculation cells in the vertical plane generated by the oscillation of the tidal current are distorted by the tidal flow asymmetry. This distortion causes sediment convergence to no longer occur at the sand wave crest, resulting in net transport in the direction of the asymmetric flow and sand wave migration (van Gerwen et al. 2018). Although tidal flow asymmetry is the primary driver of sand wave migration, wind and surface waves can also substantially impact sand wave migration (Le Bot and Trentesaux 2004). The wind during the field experiment was primarily from the northwest (Figure 45a), although the strongest winds (15–23 m/s) were mostly from the south and southeast. Wind speed reached a high of 23

m/s and an average speed of 8.8 m/s. The surface waves (Figure 45b) come predominantly from the south and southwest, with H_s ranging from 0.2 to 2.3 m and an average of 0.66 m.

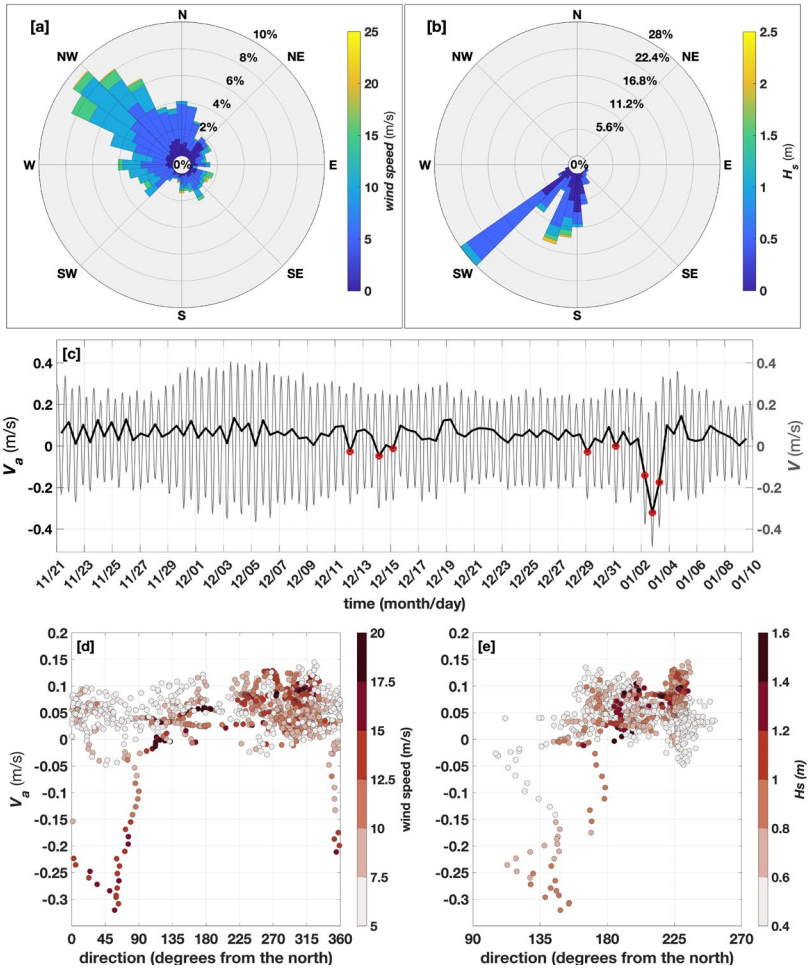

Radial histogram for (a) wind data and (b) surface waves observed during the field experiment. (c) Tidal peak current velocity asymmetry (V_a), in black, and depth-averaged current (V), in gray. Positive values indicate the flow moves in the flood tide direction (predominantly to east–northeast), and negative values (highlighted by red dots) denote the flow moves in the ebb tide direction (predominantly to west). Scatter plot of (d) tidal peak current velocity asymmetry (V_a), wind speed, and wind direction; and (e) V_a, significant wave height (H_s) and wave direction. Wind data from the Air-Sea Interaction Tower (ASIT), currents, and waves were observed at the quadpod location. Direction is reported as coming from.

Figure 45. Tidal flow asymmetry, wind, and surface waves

The tidal flow asymmetry may be characterized by the tidal peak current velocity asymmetry (V_a), which is the difference between flood peak and ebb peak velocities (Le Bot and Trentesaux 2004). Figure 45c shows the V and Va time series at the quadpod location. From V, the maximum ebb and flood peak current velocity are -0.48 m/s and 0.41 m/s, with mean of -0.23 m/s (ebb) and 0.28 m/s (flood). Values of V_a range between -0.32 m/s and 0.15 m/s. For most of the observation period, V_a presents positive values (in the flood tide direction), except for short periods of negative values highlighted by the red dots, which denote V_a in the ebb tide direction. Mean V_a is 0.05 m/s in the flood tide direction. Larger negative values of V_a (2–4 January) correspond to a period of wind from northeast with 16 m/s and waves from south–southeast with H_s of 0.85 m. The variation of V_a and wind speed with regard to wind direction, as well as the variation of V_a and H_s with respect to wave direction, are depicted in Figures 45d and 45e. Negative values of V_a are associated with moderate winds primarily from north to east and small waves (H_s < 1 m) from south to southeast, showing that wind-driven currents can affect V_a and impact the sand wave migration, as mentioned by Le Bot and Trentesaux (2004). The influence of wind-driven currents on sand wave migration are supported by the model results where case III (without wind) exhibited a 15% larger sand wave migration than case I (with wind) (see Figure 44) and a mean V_a that was 9.8% higher at the quadpod location (not shown).

2. Influence of Tidal Currents and Surface Waves on Sand Wave Migration

During the 3-month simulation, the model produced hourly bathymetric maps from 16 October 2013 to 10 January 2014. For each hour, a seabed profile along transect 2 is determined from each bathymetric map from which hourly sand wave migration distance and speed toward the northeast direction can be estimated (Figure 46a). The influence of tidal current and surface wave on sand wave migration is evaluated by comparing (Figure 46b) dimensionless Shields parameters for both tidal currents (θ_t) and surface waves (θ_w) to the critical Shields parameter (θ_{cr}), similarly to van Dijk and Kleinhans (2005) and Damen et al. (2018). The migration speed, θ_t, and θ_w presented in Figure 46 are computed using the model result at the quadpod location. The critical value

θ_{cr} is determined as a function of the non-dimensional grain size (van Rijn 1993), and used as a threshold for initial sediment motion (Shields 1936). Shields parameter and shear stress for tidal currents (τ_t) and surface waves (τ_w) are calculated following van Rijn (1993)

$$\theta = \frac{\tau}{\left(\rho_s - \rho_w\right) g D_{50}} \tag{28}$$

$$\tau_t = \rho_w g \left[\frac{V}{18 \log_{10}\left(\frac{12d}{2.5 D_{50}} \right)} \right]^2 \tag{29}$$

$$\tau_w = \rho_w u_{orb}^2 \exp\left[5.213 \left(\frac{2.5 D_{50}}{A_{orb}} \right)^{0.194} - 5.977 \right], \tag{30}$$

where ρ_s is the density of the sediment, ρ_w is the density of salt water, g is the gravitational acceleration, d is the local depth, u_{orb} is the wave orbital velocity, and A_{orb} is the wave orbital excursion near bed.

The average migration speed over the 3-month model simulation is 40.4 cm/day along transect 2 and 55.8 cm/day along transect 7, which is consistent with the sand wave migration observed in the bathymetric data and with the observed mean migration speed of 50 cm/day over a 9-month period, from 16 October 2013 to 18 July 2014, reported by Jones and Traykovski (2019). However, the estimated migration speed is not constant as large peaks in migration speed can be observed to occur on 28 November; 16, 22, and 30 December; and 7 January (Figure 46a). The peak migration speed is estimated as high as 627.3 cm/day. The regularly spaced smaller peaks are related to θ_t and migration driven by the tidal currents. A qualitative comparison between mean migration speed and Shields parameter (Figure 46) indicates that peaks of estimated migration speed correspond to peaks of θ_w, which also coincide with periods of wave events when H_s >1.5 m (Figure 41c), which highlight the influence of surface waves on the sand wave migration speed.

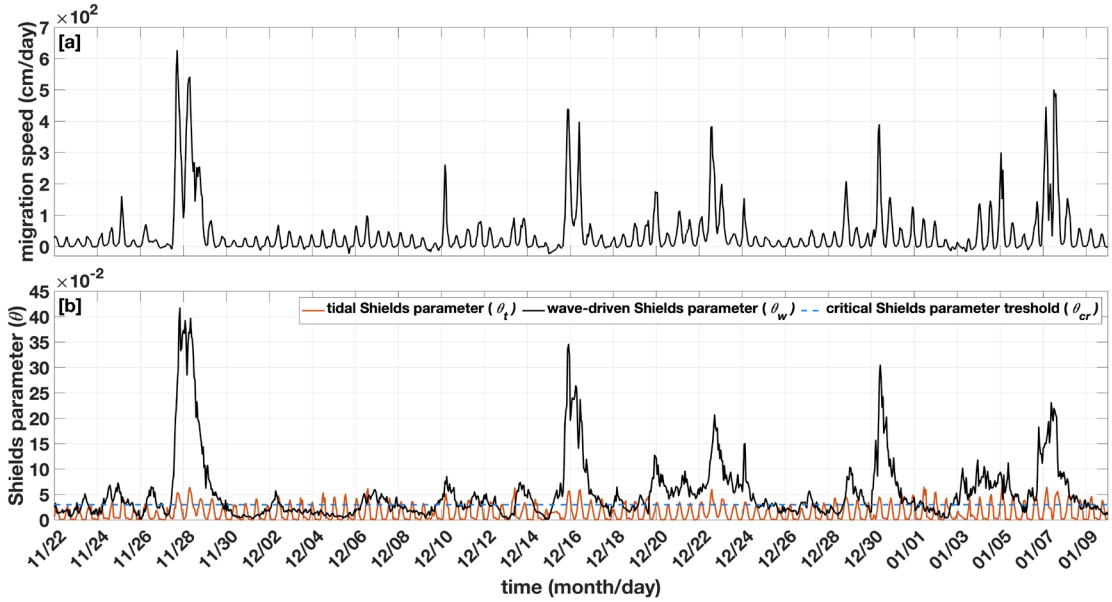

(a) Hourly mean migration speed estimated from the model output, (b) wave-driven Shields parameter (θ_w), and tidal current Shields parameter (θ_t) time series. The blue dashed line represents the critical Shields parameter (θ_{cr}) for initiation of sediment motion.

Figure 46. Predicted mean sand wave migration speed and Shields parameter

From 29 November to 15 December 2013 (16 days), no large surface wave events occurred (H_s < 1 m with mean H_s = 0.467 m, see Figure 41c), which is reflected in the relatively small θ_w during this time (Figure 47b). Figure 47a zooms in on the hourly mean migration speed estimated from a simulation including surface waves (back curve) and a simulation without surface waves (red curve) during this time. The simulation, including surface waves, presented an average migration speed of 17 cm/day, consistent with field observations of 12 ± 3.6 cm/day (95% confidence interval) estimated from a rotary sidescan sonar data in this exact location and period (Jones and Traykovski 2019). For the simulation without surface waves, the average migration speed is 5.6 cm/day, representing a reduction of 67% in the average migration speed when surface waves are taken into consideration. The migration speed and θ_t are correlated in simulations with and without surface waves, with correlation coefficient (R) of 0.70 and 0.72, respectively. Peaks of migration speed in the simulation accounting for surface waves corresponds to periods in which θ_w is greater than the θ_{cr} (Figure 47b).

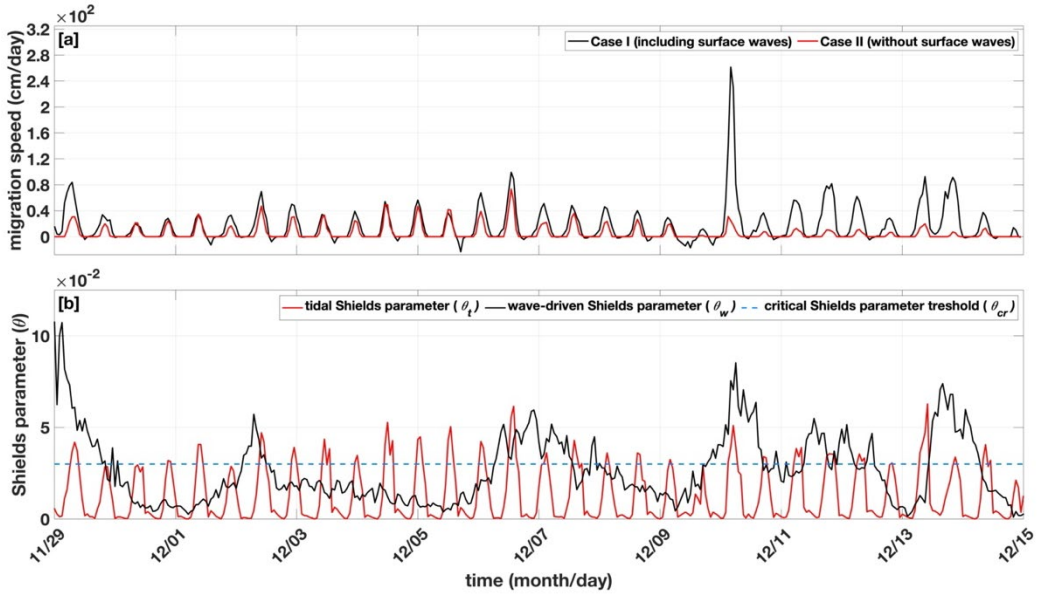

(a) Hourly mean migration speed, (b) wave-driven Shields parameter (θ_w), and tidal current Shields parameter (θ_t) time series estimated from model results in a period (16 days) of no large surface wave event. The blue dashed line represents the critical Shields parameter (θ_{cr}) for initiation of sediment motion. The mean migration speed was estimated from a simulation including surface waves (black curve) and from a simulation without surface waves (red curve).

Figure 47. Predicted mean sand wave migration speed and Shields parameter for a period with no large surface wave events

According to Campmans et al. (2018), although surface wave events do not trigger sand wave migration, they can boost the migration of sand waves in the presence of asymmetrical tidal flow, decreasing sand wave growth and eventually reducing sand wave height. These conclusions come from simulations using a highly idealized 2DV model considering storm conditions in a region with a mean water depth of 30 m. However, when they modeled sand wave migration for a more realistic scenario with surface waves in brief intervals of stormy conditions alternating with periods of good weather conditions, the results were similar to simulations for sand wave migration considering only tidal forcing. In contrast, the result presented in Figure 47 implies that the influence of surface waves on shallow areas (water depth less than 10 m) is relevant even during less energetic periods.

3. Rotation of the Sand Wave

The comparison between the observed initial and final bathymetry (Figure 38) exhibits counterclockwise sand wave rotation where the southern portion of the sand wave migrates faster than the northern portion. Figure 48 presents a comparison between two simulations, the first including surface waves (case I) and the second a simulation without surface waves (case II) along transect 1 (northern portion of the sand wave) and transect 7 (southern portion). For case I, the sand wave migration along transect 7 is 48 m (distance between the black and blue arrow), which is 16 m further than the migration on transect 1 (32 m). Both transects for case II underestimated the migration and sand wave rotation, as evidenced by the decreased migration, distance between the black and red arrow, on transects 1 (12 m) and 7 (16 m).

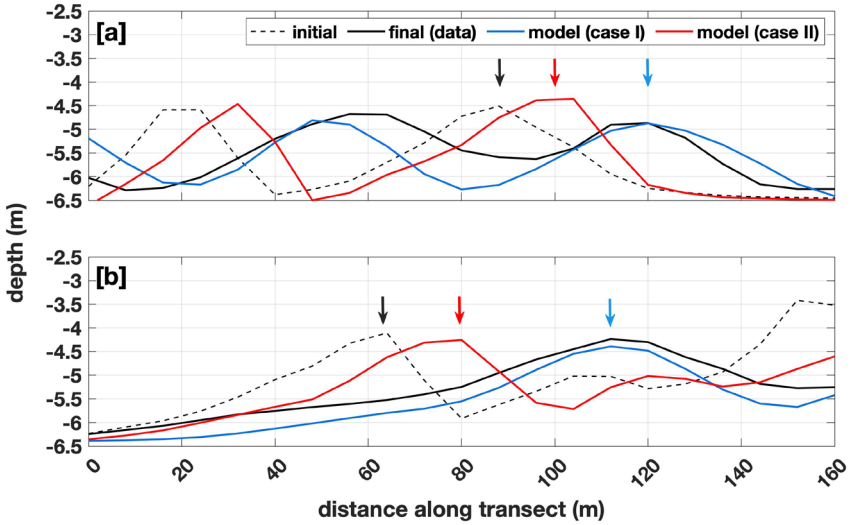

Bed level profiles along (a) transect 1 and (b) transect 7. Bathymetry on 16 October 2013 and 10 January 2014 are shown as the dashed black and solid black curves, respectively. The blue line represents the model result for case I, including surface waves, and red line, for case II, simulation without surface waves. The black arrow indicates the observed initial position of a sand wave peak, blue and red arrows indicate the modeled final position of the same sand wave peak for case I and case II, respectively.

Figure 48. Bed level profiles along transects 1 and 7 for cases I and II

Sand wave rotation has been attributed to spatially changing migration speeds related to depth since migration speeds tend to be slower in deeper locations and faster in shallower areas, which tilt the original sand wave axis (Tonnon et al. 2007). In shallow areas, the flow acceleration owing to the energy conservation enhances the spatial tidal flow variation impacting sand wave migration speed along with the sand wave rotation. A similar effect on the spatial variation of sand wave migration speed is caused by the orbital motions from surface waves, which stir up the sediment at the seabed in shallow areas when surface waves are sufficiently vigorous (Tonnon et al. 2007); this stirring can amplify the migration (Campmans et al. 2018).

The Shields parameters (θ_w and θ_t) were calculated over the area of interest to examine the impact of tidal current and surface waves on the sand wave migration and rotation. Figure 49 shows θ_w maps for wave event condition (H_s = 2.4 m) and small wave condition (H_s = 0.5 m), and θ_t maps for maximum tidal conditions (V = 0.41 m/s) during the spring tidal conditions and mean tidal conditions, considering the average of peak tidal current (V = 0.28 m/s). The highest values of θ_w and θ_t are reached for wave event and maximum tidal conditions, in which Shields parameter exceeds the θ_{cr} in the entire area of interest (Figures 49a and 49c). In contrast, θ_w and θ_t do not surpass the θ_{cr} values in areas highlighted in gray (Figures 49b and 49d) for the small wave and mean tidal conditions. All maps exhibit higher values of Shields parameter to the south, where higher migration speed is observed. These results reveal that the combined effects of tidal flow and surface waves cause a faster migration speed in the southern portion, forcing the sand wave to rotate counterclockwise.

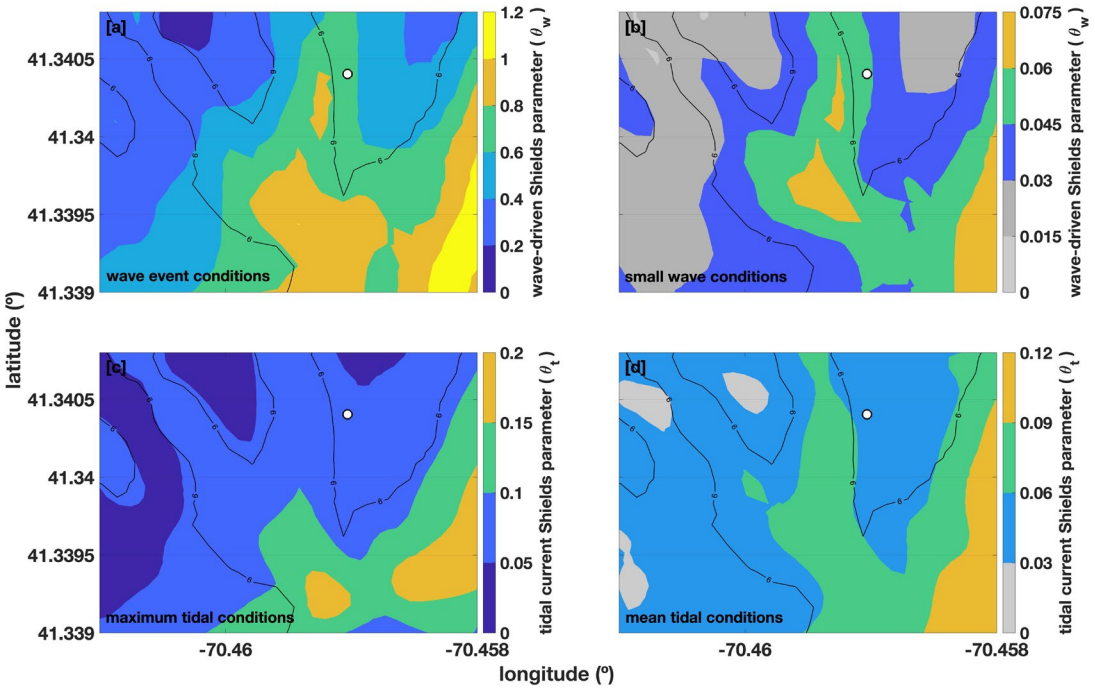

Wave-driven Shields parameter (θ_w) map for (a) wave event condition (H_s = 2.4 m) and (b) small wave condition (H_s = 0.5 m), and tidal current Shields parameter (θ_t) map for (c) maximum tidal conditions (V = 0.41 m/s) and (d) mean tidal conditions (V = 0.28 m/s). The 6-m depth contour is represented by the black line and the quadpod location is denoted by the white dot.

Figure 49. Shields parameter map

E. SUMMARY AND CONCLUSIONS

Sand wave migration at Wasque Shoals off the coast of Martha's Vineyard is examined by analyzing observational data and the output from a Delft3D model capable of simulating flow, waves, and morphological responses. The main goal is to implement a model using the 3D approach that accurately represents the sand wave dynamics near the coast. Additionally, the physical processes responsible for the high migration speed in the study area are investigated.

Comparisons between the model output and field observations indicate that the model accurately depicted the hydrodynamics in the study area, as skill scores for mean water level, current velocity, and significant wave height were 0.979, 0.816, and 0.962, respectively. In addition, the ability of the model to represent seabed evolution was

verified by comparing observed and simulated bathymetric changes. The comparison between the simulated and observed final bathymetry reveals that the model accurately reproduced seabed evolution, with a mean Brier Skill Score of 0.862.

The effects of the surface waves and wind on sand wave migration were assessed by running the model for several simulations. The simulation without surface waves (case II) presented 65% less migration than a simulation including surface waves (case I), showing that surface waves greatly increase sand wave migration. In addition, a simulation without wind (case III) overestimated the migration by 15%, indicating that wind decreases sand wave migration during the experiment.

The modeled sand wave migration speed correlates with the tidal current Shields parameter (R = 0.7). In addition, increases in the wave-driven Shields parameter associated with energetic surface wave events were found to occur at times of sharp increases in modeled sand wave migration, showing that surface waves enhance sand wave migration speed. Comparisons between the wave-driven Shields parameter and the modeled migration speed for a period with no big surface wave events show that the effect of surface waves on shallow areas can be important even when the waves are less energetic. An observed counterclockwise sand wave rotation was found to be associated with the combination of tidal currents, surface waves, and sloping bathymetry, along with spatial Shields parameter maps computed from model outputs.

We are unaware of another study that has presented a three-dimensional model, using Delft3D, in a shallow water area, with an average sand wave migration speed of 50 cm/day and observations including sand wave rotation. Other studies in this field typically adopt models in the 2DV approach and mostly simplifications, including idealized bathymetry. Moreover, considering the observed complex bathymetry, surface waves, tidal, and wind forcing make this study unique for areas with local depths of less than 10 m. Waves alone do not drive sand wave migration, which is caused by tidal asymmetry; however, the results of this paper suggest rapid sand wave migration observed over Wasque Shoals, with at least one order of magnitude larger than many previous studies, is greatly speed up by wave forcing and owing to the shallow nature of the field site. Additionally, the simulations demonstrate that the relatively shallow depth

makes the influence of surface waves important even during less energetic periods (H_s < 1m). Thus, while asymmetric tidal currents are essential for sand wave migration, such model fidelity allows for the confirmation of the hypothesis that shallow depths with wave events are largely responsible for periods of rapid migration and rotation in contrast to wind or tidal currents alone, which might apply to coastal areas with similar hydrodynamic conditions.

THIS PAGE INTENTIONALLY LEFT BLANK

V. CONCLUSION

This dissertation aimed to improve the understanding of the physical processes causing the mobility and burial of munitions through modeling the hydro-morphodynamic forcing. Each of the major chapters focuses on a specific topic and is presented in a journal paper format, including its own results. Chapters II, III, IV, and V address scour, sediment transport, wave-induced liquefaction, and sand wave migration, which all impact the burial of munitions. In addition, each Chapter discussed the local hydrodynamics, which influences the mobility of munitions. This final chapter concludes by summarizing the research results in connection to the dissertation goal and contribution.

Chapter II (Chu et al. 2021) discusses the mobility and scour burial of munitions. The implemented Coupled Delft3D-object model satisfactorily represented the local hydrodynamics and the mobility of submerged objects when compared with observations. The higher the density of an object, the smaller its mobility parameter for percentage burial and the likelihood of rolling the object. A2 (20 mm cartridge with a mass of 0.11 kg and a density of 1,429 kg m^{-3}) and C2 (81 mm mortar with a mass of 1.45 kg and a density of 1.199 kg m^{-3}) displaced 20.7 m and 6.52 m, respectively. Other objects such as A5 (density of 2,597 kg m^{-3}), B5 (density of 2,356 kg m^{-3}), C4 (density of 3,109 kg m^{-3}), C6 (density of 7,194 kg m^{-3}), D3 (density of 2,721 kg m^{-3}), and D6 (density of 4,444 kg m^{-3}), are almost immobile. Despite the good performance of the Coupled Delft3D-object model, considering only cylindrical objects is one of the limitations. Additionally, the model only accounts for a cylinder that rolls around its major axis, while the pitch and yaw movements are ignored. The seafloor is also assumed to be flat. Object modeling must be expanded for practical application to include a more accurate representation of the seafloor environment, object shapes, and mobility.

In Chapter III, the Delft3D model is used to study changes in the seafloor elevation owing to sediment transport observed during the passage of two consecutive cold fronts. The model outputs are compared with data collected in the field, including the burial of objects shown in sonar images. The model adequately predicted the local

hydrodynamics and morphological changes consistent with the burial of objects. Additionally, the model indicated cross-shore seafloor changes with erosion nearshore and accretion offshore, starting at approximately 250 m from the coast, and suggested the seafloor elevation increase (near the observation station) was a result of sediment accretion associated with front-driven waves. The Delft3D morphological module does not include wave-induced liquefaction, which was investigated in Chapter IV. Despite this constraint, the model results indicate that sediment accretion plays a role in the observed morphological changes and munition burial.

In Chapter IV, a coupled hydro-morphodynamic and wave-induced liquefaction model is presented to predict morphological changes and seafloor instability. The model represented well the observed hydrodynamics characteristics, morphological changes, and wave-induced liquefaction. Both the model results and observations show that sediment failure occurred near the shallow quadpod during the second wave event when the shallow quadpod settled into the sediment. Observations and model results also suggest the observed burial of objects was caused by wave-induced liquefaction and sediment accretion. In addition, the model results were used to create a liquefaction degree map, which shows areas with a higher chance of seafloor instability as well as the estimated failure depth in areas where liquefaction may occur. The model allows for the expansion of morphological evolution and liquefaction assessments over the entire area of interest, rather than being restricted by the location of the observation station as in previous work.

In Chapter V, a three-dimensional model is implemented to examine the physical processes responsible for the observed rapid migration and rotational aspect of a sand wave. Results show the model accurately represented the hydro-morphodynamics observed in the study area. The findings imply that the observed sand wave migration is greatly speed up by wave forcing and the migration speed is faster than in many earlier studies due to the shallow water depth in the study area. While asymmetric tidal currents are necessary for sand wave migration, such model fidelity supports the idea that shallow depths with wave occurrences, rather than wind or tidal currents alone, are predominantly

responsible for periods of fast migration and rotation, which may impact the mobility and burial of munitions.

This study has shown that numerical modeling, using the Delft3D model, is an effective tool for evaluating physical processes impacting the mobility and burial of munitions. Possible applications include the simulation of the local hydro-morphodynamics, which can be used as a forcing term by other models, such as the object and wave-induced liquefaction models. These coupled models can simulate not only the effect of sediment transport and bedform migration but also the burial scour and wave-induced liquefaction, allowing a more detailed investigation of these mechanisms. However, further research is required to test this modeling approach applied to other sites of differing characteristics. In addition, the object model used in this study needs to be improved and evaluated in future work. Despite that, the results presented in this dissertation show great potential for determining and predicting the fate of munitions and can be applied to plan remediation actions.

THIS PAGE INTENTIONALLY LEFT BLANK

APPENDIX A. LOCATION OF OBJECT'S ROTATION AXIS IN SEDIMENT[9]

The roll of an object on the sandy floor needs a supporting point in sediment. The compressive normal stress of sediment on the object is represented by

$$F_S = -\mathbf{n}\kappa u_o \sin\psi \,, \tag{A1}$$

where **n** is unit vector normal to the cylinder surface and κ is the compressive coefficient. Let **n** be decomposed into

$$\mathbf{n} = -e_h \sin\psi - e_v \cos\psi \,, \tag{A2}$$

where (e_h, e_v) are horizontal and vertical unit vectors (see Figure 50). The sediment compressive normal stress $\boldsymbol{F}_S$ is decomposed as

$$F_S = e_h \kappa u_o \sin^2\psi + e_v \kappa u_o \sin\psi\cos\psi \,. \tag{A3}$$

With b as the axis of rotation, the sediment above (below) the depth b generates torque to resist (enhance) the rolling with the total torque from the sediment

$$T_S = \int_0^{\psi_B} \left[\left(r - r_b\right) \times F_S \right] d\psi = \int_0^{\psi_B} \left[r \times F_S \right] d\psi - r_b \times \int_0^{\psi_B} F_S \, d\psi \,, \tag{A4}$$

where r is the position vector at any point on the circle and $\boldsymbol{r}_b$ is the position vector at point b with point E as the origin.

$$r = \frac{D}{2}\left[-e_h \sin\psi + e_v (1 - \cos\psi) \right], \quad r_b = \frac{D}{2}\left[-e_h \sin\psi_b + e_v (1 - \cos\psi_b) \right] \tag{A5}$$

The depths B and b are represented by

$$B = \frac{D}{2}(1 - \cos\psi_B), \quad b = \frac{D}{2}(1 - \cos\psi_b) \,. \tag{A6}$$

If we assume that at the depth b the total torque from the sediment is zero (i.e., zero-sum sediment torque for rolling), the result is

$$T_S = 0 \,. \tag{A7}$$

Substitution of (A3)–(A5) into (A7) gives

[9] This Appendix was previously published by *Fluids* (Chu et al. 2021). Co-authors include Peter C. Chu, Vinícius S. Pessanha, Chenwu Fan, and Joseph Calantoni. Content related to this research has also been published by IEEE (Chu et al. 2022). In addition, as part of this research effort, Dr. Chu's interim report published by SERDP (Chu 2020) reported on the earlier progress of this research by Dr. Chu.

$$\psi_b = \tan^{-1}\left(\frac{\psi_B - \sin\psi_B \cos\psi_B}{\sin^2\psi_B}\right). \tag{A8}$$

The ratio $\lambda = b/B$ can be obtained from (A6) and (A8).

$$\lambda \equiv b/B = \frac{1-\cos\left[\tan^{-1}\left(\frac{\psi_B - \sin\psi_B \cos\psi_B}{\sin^2\psi_B}\right)\right]}{1-\cos\psi_B} \tag{A9}$$

The ratio, λ, varies with the burial percentage $p_B = B/D$ mildly from near 0.4445 for p_B = 0 and 0.4630. Here, we take $\lambda = 0.453$ in this study.

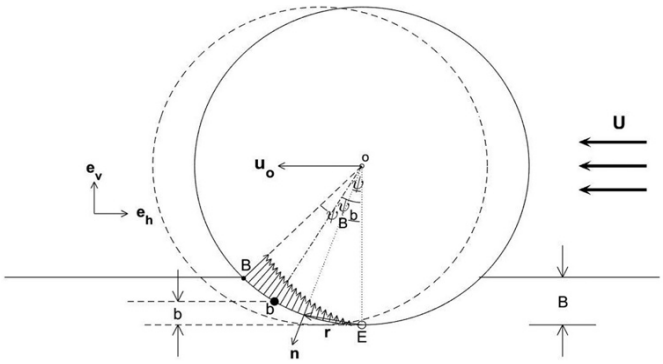

The location of the axis of rotation of the cylinder in the sediment, *b*, is determined by the assumption of zero-sum torque to the roll.

Figure 50. Axis of rotation of the cylinder in the sediment

APPENDIX B. DYNAMICS OF ROLLING OBJECT[10]

The drag force (F_d) and lift force (F_l) (see Appendix C) roll the object forward with the torque T_F (Figure 51).

$$\begin{aligned} T_F &= F_d(D/2 + B/2 - b) + F_l\sqrt{b(D-b)} \\ &= \frac{1}{2}C_d\rho_w U^2 L\left[(D-B)(D/2+B/2-b) + \frac{C_l}{C_d}D\sqrt{b(D-b)}\right]\left(1-\frac{u_o}{U}\right)^2 \end{aligned} \tag{A10}$$

The buoyancy force and added mass roll the object backward with the torque, $T_B = T_w + T_a$,

$$\begin{aligned} T_B &= F_w\sqrt{b(D-b)} + F_a(D/2+B/2-b) \\ &= \frac{\pi}{4}gLD^2(\rho_o-\rho_w)\sqrt{b(D-b)} + \frac{du_o}{dt}\rho_w \forall (D/2+B/2-b) \end{aligned} . \tag{A11}$$

When $T_F > T_B$ the object accelerates if it is in motion or starts to move if it is at rest ($u_o = 0$, $du_o/dt = 0$). When $T_F < T_B$ the object decelerates if it is in motion or keeps motionless if it is at rest. When $T_F = T_B$ the object keeps velocity constant if it is in motion or keeps motionless if it is at rest. Thus, the threshold for the munition's mobility becomes

$$T_F > T_B . \tag{A12}$$

The acceleration-deceleration ratio is defined by

$$\frac{T_F}{T_B} = \theta_{opb}\left(1-\frac{u_o}{U}\right)^2 , \tag{A13}$$

where

$$\begin{aligned} \theta_{opb} &= \frac{\theta_0}{\pi}\left[\frac{1-p_b}{\sqrt{p_b(1-p_b)}}(1+p_B-2p_b)+2\gamma\right], \\ \theta_0 &\equiv \left[\frac{C_d U^2}{gD(S_o-1)}\right], \quad p_b = \frac{b}{D}, \quad S_o = \frac{\rho_o}{\rho_w} > 1 \end{aligned} \tag{A14}$$

[10] This Appendix was previously published by *Fluids* (Chu et al. 2021). Co-authors include Peter C. Chu, Vinícius S. Pessanha, Chenwu Fan, and Joseph Calantoni. Content related to this research has also been published by IEEE (Chu et al. 2022). In addition, as part of this research effort, Dr. Chu's interim report published by SERDP (Chu 2020) reported on the earlier progress of this research by Dr. Chu.

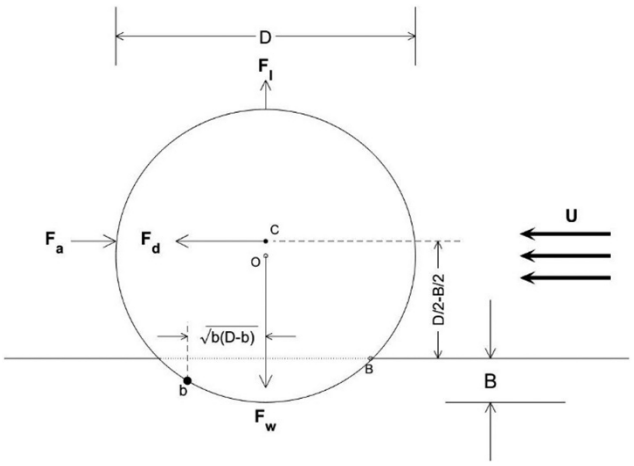

Forces and torques due to drag, lift, buoyancy, and added mass on a partially buried cylinder by combination of ocean currents and bottom wave orbital velocity (U) perpendicular to the major axis of the cylinder.

Figure 51. Forces and torques on a partially buried cylinder

Here, θ_{opb} is the object's mobility parameter for percentage burial p_b (Traykovski and Austin 2017) and S_o is the relative density of the object. For motionless munitions (u_o = 0), the condition for the object to move is obtained through substituting (A13) into (A12).

$$\theta_{opb} > 1 \tag{A15}$$

The corresponding moment of momentum equation of the rolling object is given by

$$\begin{cases} I_A \dfrac{d\omega}{dt} = T_F - T_B \quad \text{if} \quad p_B < 0.5, \quad \theta_{opb} > 1 \\ \omega = 0, \quad \text{otherwise} \end{cases}. \tag{A16}$$

Substitution of (T_F, T_B) in (A10) (A11) into (16) leads to

$$\begin{cases} I_A^* \dfrac{d\omega}{dt} = T_F - \Pi(\rho_o - \rho_w)\sqrt{b\left(D-b\right)} \quad \text{if} \quad p_B < 0.5, \quad \theta_{opb} > 1 \\ \omega = 0, \quad \text{otherwise} \\ I_A^* = I_A + \left(\dfrac{D}{2} - b\right)\rho_w \Pi(D/2 + B/2 - b) \end{cases}, \tag{A17}$$

with

$$I_A = I_o + \rho_o \Pi D^2 / 4, \tag{A18}$$

where I_o is the rolling moment about the symmetric axis of the munition, I_A is the rolling moment of munition about the point *b* (see Figure 51) using the parallel axis theorem, and Π is the volume of the munition.

THIS PAGE INTENTIONALLY LEFT BLANK

APPENDIX C. DRAG, LIFT, BUOYANCY FORCES, AND ADDED MASS[11]

The drag force (F_d), lift force (F_l), buoyancy force (F_w), and added mass (F_a) exerted on the object for rolling by the perpendicular component, U, are given by

$$F_d = \frac{\rho_w C_d U^2 L(D-B)}{2}, \quad F_l = \frac{\rho_w C_l U^2 LD}{2}, \\ F_w = g(\rho_o - \rho_w)\Pi, \quad F_a = -\rho_w \Pi \frac{du_o}{dt} \tag{A19}$$

where g = 9.81 m/s^2 is the gravitational acceleration, ρ_w = 1,025 kg/m^3 is the density of seawater, ρ_o is the density of the cylindrical object, and (C_d, C_l) are the drag and lift coefficients across-cylinder's main axis with vortex shedding caused by the oscillating flow (U) due to waves. If time averaged U within a certain time period is used, the mean coefficients for drag and lift (C_d, C_l), depending solely on the Reynolds number and aspect ratio (see Appendix D), can be used. Since the wave component (i.e., the bottom wave orbital velocity) in V_w for the object model is computed from a linear wave model with the temporal resolution of 30 minutes, the mean coefficients for drag and lift are used. The vortex shedding from objects is neglected. Besides, the lift coefficient is less certain, we assume

$$C_l = \gamma C_d \,, \tag{20}$$

where γ is the ratio of lift coefficient versus drag coefficient with γ being taken as value of 0.2.

[11] This Appendix was previously published by *Fluids* (Chu et al. 2021). Co-authors include Peter C. Chu, Vinícius S. Pessanha, Chenwu Fan, and Joseph Calantoni. Content related to this research has also been published by IEEE (Chu et al. 2022). In addition, as part of this research effort, Dr. Chu's interim report published by SERDP (Chu 2020) reported on the earlier progress of this research by Dr. Chu.

THIS PAGE INTENTIONALLY LEFT BLANK

APPENDIX D. DRAG COEFFICIENT[12]

For cylindrical objects, the drag force is decomposed into along and cross-axis components. The drag coefficient across-cylinder's main axis C_d depends on the Reynolds number

$$\mathrm{Re} = \frac{UD}{\nu}, \tag{A21}$$

where $\nu = 0.8\times10^{-6}$ m^2/s, is the sea water kinematic viscosity; U is the horizontal water velocity perpendicular to the cylinder's main axis; and D is the cylinder's diameter (see Figure 6). An empirical formula is used to calculate C_d (Rouse 1938)

$$Cd = \begin{cases} 1.9276 + 8/\mathrm{Re}, & \text{if} \quad \mathrm{Re} \le 12 \\ 1.261 + 16/\mathrm{Re}, & \text{if} \quad 12 < \mathrm{Re} \le 180 \\ 0.855 + 89/\mathrm{Re}, & \text{if} \quad 180 < \mathrm{Re} \le 2000 \\ 0.84 + 0.00003\mathrm{Re}, & \text{if} \quad 2000 < \mathrm{Re} \le 12000 \\ 1.2 - 4/\eta, & \text{if} \quad 12000 < \mathrm{Re} \le 150000, \quad \eta \ge 10 \\ 0.835 - 0.35/\eta, & \text{if} \quad 12000 < \mathrm{Re} \le 150000, \quad 2 \le \eta < 10 \\ 0.7 - 0.08/\eta, & \text{if} \quad 12000 < \mathrm{Re} \le 150000, \quad \eta < 2 \\ 1.875 - 0.0000045\mathrm{Re}, & \text{if} \quad 150000 < \mathrm{Re} \le 350000 \\ 1/\left(641550/\mathrm{Re} + 1.5\right), & \text{if} \quad \mathrm{Re} > 350000 \end{cases}, \tag{A22}$$

where $\eta = L/D$, is the cylinder's aspect ratio.

[12] This Appendix was previously published by *Fluids* (Chu et al. 2021). Co-authors include Peter C. Chu, Vinícius S. Pessanha, Chenwu Fan, and Joseph Calantoni. Content related to this research has also been published by IEEE (Chu et al. 2022). In addition, as part of this research effort, Dr. Chu's interim report published by SERDP (Chu 2020) reported on the earlier progress of this research by Dr. Chu.

THIS PAGE INTENTIONALLY LEFT BLANK

LIST OF REFERENCES

Aliotta, S., and G. M. E. Perillo, 1987: A sand wave field in the entrance to Bahia Blanca Estuary, Argentina. *Mar. Geol.*, **76**, https://doi.org/10.1016/0025-3227(87)90013-2.

Barnard, P. L., D. M. Hanes, D. M. Rubin, and R. G. Kvitek, 2006: Giant sand waves at the mouth of San Francisco Bay. *Eos (Washington, DC)*, **87**, https://doi.org/10.1029/2006eo290003.

Battjes, J. A., and J. P. F. M. Janssen, 1978: Energy loss and set-up due to breaking random waves. *Coast. Eng. Proc.*, **1**, https://doi.org/10.9753/icce.v16.32.

Bellec, V. K., and Coauthors, 2019: Sandbanks, sandwaves and megaripples on Spitsbergenbanken, Barents Sea. *Mar. Geol.*, **416**, https://doi.org/10.1016/j.margeo.2019.105998.

Bendat, J. S., and A. G. Piersol, 2012: Random Data: Analysis and Measurement Procedures: Fourth Edition.

Bennett, R. H., 2000: Mine burial prediction workshop report and recommendations (Technical Report SI-0000-03).

van den Berg, J., F. Sterlini, S. J. M. H. Hulscher, and R. van Damme, 2012: Non-linear process based modelling of offshore sand waves. *Cont. Shelf Res.*, **37**, https://doi.org/10.1016/j.csr.2012.01.012.

Besio, G., P. Blondeaux, M. Brocchini, and G. Vittori, 2004: On the modeling of sand wave migration. *J. Geophys. Res. Ocean.*, **109**, https://doi.org/10.1029/2002JC001622.

Besio, G., and Coauthors, 2008: The morphodynamics of tidal sand waves: A model overview. *Coast. Eng.*, **55**, https://doi.org/10.1016/j.coastaleng.2007.11.004.

Biot, M. A., 1941: General theory of three-dimensional consolidation. *J. Appl. Phys.*, **12**, https://doi.org/10.1063/1.1712886.

Blondeaux, P., and G. Vittori, 2016: A model to predict the migration of sand waves in shallow tidal seas. *Cont. Shelf Res.*, **112**, 31–45, https://doi.org/10.1016/j.csr.2015.11.011.

Boggs, S., 1974: Sand-Wave Fields in Taiwan Strait. *Geology*, **2**, https://doi.org/10.1130/0091-7613(1974)2<251:SFITS>2.0.CO;2.

Booij, N., R. C. Ris, and L. H. Holthuijsen, 1999: A third-generation wave model for coastal regions: 1. Model description and validation. *J. Geophys. Res. Ocean.*, **104**, 7649–7666, https://doi.org/10.1029/98JC02622.

Borsje, B. W., P. C. Roos, W. M. Kranenburg, and S. J. M. H. Hulscher, 2013: Modeling tidal sand wave formation in a numerical shallow water model: The role of turbulence formulation. *Cont. Shelf Res.*, **60**, 17–27, https://doi.org/10.1016/j.csr.2013.04.023.

——, W. M. Kranenburg, P. C. Roos, J. Matthieu, and S. J. M. H. Hulscher, 2014: The role of suspended load transport in the occurrence of tidal sand waves. *J. Geophys. Res. Earth Surf.*, **119**, https://doi.org/10.1002/2013JF002828.

Le Bot, S., and A. Trentesaux, 2004: Types of internal structure and external morphology of submarine dunes under the influence of tide- and wind-driven processes (Dover Strait, northern France). *Mar. Geol.*, **211**, 143–168, https://doi.org/10.1016/j.margeo.2004.07.002.

Bunya, S., and Coauthors, 2010: A High-Resolution Coupled Riverine Flow, Tide, Wind, Wind Wave, and Storm Surge Model for Southern Louisiana and Mississippi. Part I: Model Development and Validation. *Mon. Weather Rev.*, **138**, 345–377, https://doi.org/10.1175/2009MWR2906.1.

Calantoni, J., T. Staples, and A. Sheremet, 2014: Long Time Series Measurements of Munitions Mobility in the Wave-Current Boundary Layer SERDP Project Number 2320.

Callaghan, D. P., P. Nielsen, A. Short, and R. Ranasinghe, 2008: Statistical simulation of wave climate and extreme beach erosion. *Coast. Eng.*, **55**, https://doi.org/10.1016/j.coastaleng.2007.12.003.

Campmans, G. H. P., P. C. Roos, H. J. de Vriend, and S. J. M. H. Hulscher, 2018: The Influence of Storms on Sand Wave Evolution: A Nonlinear Idealized Modeling Approach. *J. Geophys. Res. Earth Surf.*, **123**, 2070–2086, https://doi.org/10.1029/2018JF004616.

Cataño-Lopera, Y. A., S. T. Demir, and M. H. García, 2007: Self-burial of short cylinders under oscillatory flows and combined waves plus currents. IEEE *J. Ocean. Eng.*, **32**, https://doi.org/10.1109/JOE.2007.890968.

Chu, P., and C. Fan, 2005: Pseudocylinder Parametrization for Mine Impact Burial Prediction. *J. Fluids Eng.*, **127**, https://doi.org/10.1115/1.2060741.

Chu, P. C., 2009: Mine impact burial prediction from one to three dimensions. *Appl. Mech. Rev.*

——, and C. Fan, 2006: Prediction of falling cylinder through air-water-sediment columns. *ASME J. Appl. Mech.*

Chu, P. C., 2020: Coupled Ensemble Seafloor Environment and 6-DOF (CESE6D) Model for Assessing Characteristics of Munitions Underwater and Their Environment SERDP Project Number MR19-1073.

Chu, P. C., and C. Fan, 2007: Mine-impact burial model (IMPACT35) verification and improvement using sediment bearing factor method. IEEE *J. Ocean. Eng.*, **32**, https://doi.org/10.1109/JOE.2007.890942.

Chu, P. C., and C. W. Fan, 2022: User's Guide: Underwater Munition Scour Burial (UnMUSB) Model (Technical Report, NPS-OC-22-002).

Chu, P. C., C. W. Fan, A. D. Evans, and A. Gilles, 2004: Triple coordinate transforms for prediction of falling cylinder through the water column. *J. Appl. Mech*.

——, A. Gilles, and C. Fan, 2005: Experiment of falling cylinder through the water column. *Exp. Therm. Fluid Sci*.

——, P. Pauly, and S. D. Haeger, 2006: Wind and Tidal Effects on Chemical Spill in St Andrew Bay System. *Coast. Environ. Water Qual.*, 47–68.

Chu, P. C., V. S. Pessanha, C. Fan, and J. Calantoni, 2021: Coupled delft3D-object model to predict mobility of munition on sandy seafloor. *Fluids*, **6**, https://doi.org/10.3390/fluids6090330.

——, C. Fan, J. Calantoni, and A. Sheremet, 2022: Prediction of Mobility and Burial of Objects on Sandy Seafloor. IEEE *J. Ocean. Eng.*, **47**, https://doi.org/10.1109/JOE.2021.3098391.

Damen, J. M., T. A. G. P. van Dijk, and S. J. M. H. Hulscher, 2018: Spatially Varying Environmental Properties Controlling Observed Sand Wave Morphology. *J. Geophys. Res.*, https://doi.org/10.4121/uuid:0d7e016d-2182-46ea-bc19-cdfda5c20308.

Damveld, J. H., B. W. Borsje, P. C. Roos, and S. J. M. H. Hulscher, 2020: Horizontal and Vertical Sediment Sorting in Tidal Sand Waves: Modeling the Finite-Amplitude Stage. *J. Geophys. Res. Earth Surf.*, **125**, https://doi.org/10.1029/2019JF005430.

Deltares, 2022a: Delft3D-Flow: Simulation of multi-dimensional hydrodynamic flows and transport phenomena, including sediments, User Manual.

——, 2022b: Delft3D-Wave: Simulation of short-crested waves with SWAN, User Manual.

Demir, S. T., and M. H. García, 2007: Experimental Studies on Burial of Finite-Length Cylinders under Oscillatory Flow. *J. Waterw. Port, Coastal, Ocean Eng.*, **133**, https://doi.org/10.1061/(asce)0733-950x(2007)133:2(117).

van Dijk, T. A. G. P., and M. G. Kleinhans, 2005: Processes controlling the dynamics of compound sand waves in the North Sea, Netherlands. *J. Geophys. Res. Earth Surf.*, **110**, https://doi.org/10.1029/2004JF000173.

DiMego, G. J., L. F. Bosart, and G. W. Endersen, 1976: An Examination of the Frequency and Mean Conditions Surrounding Frontal Incursions into the Gulf of Mexico and Caribbean Sea. *Mon. Weather Rev.*, **104**, https://doi.org/10.1175/1520-0493(1976)104<0709:aeotfa>2.0.co;2.

ECMWF, 2019: ERA5 Reanalysis (0.25 Degree Latitude-Longitude Grid), Research Data Archive at the National Center for Atmospheric Research.

Egbert, G. D., and S. Y. Erofeeva, 2002: Efficient Inverse Modeling of Barotropic Ocean Tides. *J. Atmos. Ocean. Technol.*, **19**, 183–204, https://doi.org/10.1175/1520-0426(2002)019<0183:EIMOBO>2.0.CO;2.

Farrar, P. D., L. E. Borgman, L. B. Glover, R. D. Reinhard, J. Pope, A. Swain, and B. A. Ebersole, 1994a: *Storm impact assessment for beaches at Panama City, Florida (Report CERC-94-11)*.

Farrar, P. D., L. E. Borgman, L. B. Glover, R. D. Reinhard, and A. Swain, 1994b: *Storm Impact Assessment for Beaches at Panama City, Florida*.

Ferreira, Ó., 2005: Storm groups versus extreme single storms: Predicted erosion and management consequences. *J. Coast. Res.*, **21**.

Friedrichs, C. T., S. E. Rennie, and A. Brandt, 2016: Self-burial of objects on sandy beds by scour: A synthesis of observations. *Scour and Erosion - Proceedings of the 8th International Conference on Scour and Erosion, ICSE 2016*.

van Gerwen, W., B. W. Borsje, J. H. Damveld, and S. J. M. H. Hulscher, 2018: Modelling the effect of suspended load transport and tidal asymmetry on the equilibrium tidal sand wave height. *Coast. Eng.*, **136**, 56–64, https://doi.org/10.1016/j.coastaleng.2018.01.006.

de Groot, M. B., M. Kudella, P. Meijers, and H. Oumeraci, 2006: Liquefaction Phenomena underneath Marine Gravity Structures Subjected to Wave Loads. *J. Waterw. Port, Coastal, Ocean Eng.*, **132**, 325–335, https://doi.org/10.1061/(ASCE)0733-950X(2006)132:4(325).

Guo, B., M. V. Subrahmanyam, and C. Li, 2020: Waves on Louisiana Continental Shelf Influenced by Atmospheric Fronts. *Sci. Rep.*, **10**, https://doi.org/10.1038/s41598-019-55578-w.

Hasselmann, K., 1974: On the spectral dissipation of ocean waves due to white capping. *Boundary-layer Meteorol.*, **6**, 107–127, https://doi.org/10.1007/BF00232479.

Hopkins, J., S. Elgar, and B. Raubenheimer, 2017: Flow separation effects on shoreline sediment transport. *Coast. Eng.*, **125**, 23–27, https://doi.org/10.1016/j.coastaleng.2017.04.007.

——, ——, and ——, 2018: Storm Impact on Morphological Evolution of a Sandy Inlet. *J. Geophys. Res. Ocean.*, **123**, 5751–5762, https://doi.org/10.1029/2017JC013708.

Hsu, J. R. C., and D. S. Jeng, 1994: Wave-induced soil response in an unsaturated anisotropic seabed of finite thickness. *Int. J. Numer. Anal. Methods Geomech.*, **18**, 785–807.

Hulscher, S. J. M. H., 1996: Tidal-induced large-scale regular bed form patterns in a three-dimensional shallow water model. *J. Geophys. Res. Ocean.*, **101**, https://doi.org/10.1029/96JC01662.

Jeng, D. S., 2003: Wave-induced sea floor dynamics. *Appl. Mech. Rev.*, **56**, 407–429, https://doi.org/10.1115/1.1577359.

——, 2013: *Porous models for wave-seabed interactions*. Springer-Verlag Berlin Heidelberg, 289 pp.

——, 2018: Mechanics of Wave-Seabed-Structure Interactions.

Jia, Y., L. Zhang, J. Zheng, X. Liu, D. S. Jeng, and H. Shan, 2014: Effects of wave-induced seabed liquefaction on sediment re-suspension in the Yellow River Delta. *Ocean Eng.*, **89**, 146–156, https://doi.org/https://doi.org/10.1016/j.oceaneng.2014.08.004.

Jones, K. R., and P. Traykovski, 2019: Interaction of Superimposed Megaripples and Dunes in a Tidally Energetic Environment. *J. Coast. Res.*, **35**, 948–958, https://doi.org/10.2112/JCOASTRES-D-18-00084.1.

Kamke, E., 1977: Differentialgleichungen: Losungsmethoden und Losungen. I. B. G. Teubner.

Kimball, P., and Coauthors, 2015: The WHOI Jetyak: An autonomous surface vehicle for oceanographic research in shallow or dangerous waters. *2014* IEEE*/OES Autonomous Underwater Vehicles, AUV 2014*.

Klammler, H., A. Sheremet, and J. Calantoni, 2020: Seafloor Burial of Surrogate Unexploded Ordnance by Wave-Induced Sediment Instability. IEEE *J. Ocean. Eng.*, **45**, 927–936, https://doi.org/10.1109/JOE.2019.2919356.

——, A. M. Penko, T. Staples, A. Sheremet, and J. Calantoni, 2021: Observations and Modeling of Wave-Induced Burial and Sediment Entrainment: Likely Importance of Degree of Liquefaction. *J. Geophys. Res. Ocean.*, **126**, https://doi.org/10.1029/2021JC017378.

Komar, P. D., 1998: *Beach processes and sedimentation*. 2nd ed. Prentice Hall.

Krabbendam, J., A. Nnafie, H. de Swart, B. Borsje, and L. Perk, 2021: Modelling the past and future evolution of tidal sand waves. *J. Mar. Sci. Eng.*, **9**, https://doi.org/10.3390/jmse9101071.

Lee, G. Hong, R. J. Nicholls, and W. A. Birkemeier, 1998: Storm-driven variability of the beach-nearshore profile at Duck, North Carolina, USA, 1981–1991. *Mar. Geol.*, **148**, https://doi.org/10.1016/S0025-3227(98)00010-3.

Leenders, S., J. H. Damveld, J. Schouten, R. Hoekstra, T. J. Roetert, and B. W. Borsje, 2021: Numerical modelling of the migration direction of tidal sand waves over sand banks. *Coast. Eng.*, **163**, https://doi.org/10.1016/j.coastaleng.2020.103790.

Lesser, G. R., J. A. Roelvink, J. A. T. M. van Kester, and G. S. Stelling, 2004: Development and validation of a three-dimensional morphological model. *Coast. Eng.*, **51**, 883–915, https://doi.org/10.1016/j.coastaleng.2004.07.014.

Li, Y., M. Lin, W. B. Jiang, and F. X. Fan, 2011: Process control of the sand wave migration in Beibu Gulf of the South China Sea. *J. Hydrodyn.*, **23**, https://doi.org/10.1016/S1001-6058(10)60134-5.

Madsen, O. S., 1978: Wave-induced pore pressures and effective stresses in a porous bed. *Géotechnique*, **28**, 377–393, https://doi.org/10.1680/geot.1978.28.4.377.

Morton, R. A., J. C. Gibeaut, and J. G. Paine, 1995: Meso-scale transfer of sand during and after storms: implications for prediction of shoreline movement. *Mar. Geol.*, **126**, https://doi.org/10.1016/0025-3227(95)00071-6.

Németh, A. A., S. J. M. H. Hulscher, and H. J. De Vriend, 2002: Modelling sand wave migration in shallow shelf seas. *Cont. Shelf Res.*, **22**, https://doi.org/10.1016/S0278-4343(02)00127-9.

Németh, A. A., S. J. M. H. Hulscher, and R. M. J. Van Damme, 2007: Modelling offshore sand wave evolution. *Cont. Shelf Res.,* **27**, https://doi.org/10.1016/j.csr.2006.11.010.

Nielsen, P., 1992: Coastal Bottom Boundary Layers and Sediment Transport. World Scientific, 340 pp.

NOAA/NDBC, Surface wind vector data at the Station PACF1 8729108 – Panama City, FL. https://www.ndbc.noaa.gov/station_page.php?station=pacf1 (Accessed September 10, 2018).

NOAA/NGDC, 1999: U.S. Coastal Relief Model Vol.1- Northeast Atlantic. https://www.ncei.noaa.gov/access/metadata/landing-page/bin/iso?id=gov.noaa.ngdc.mgg.dem:713 (Accessed July 26, 2022).

——, 2010: Northern Gulf 1 arc-second MHW Coast Digital Elevation Model. *NOAA Natl. Centers Environ. Inf.*

NOAA/WPC, 2020: Weather Prediction Center's Surface Analysis Archive. https://www.wpc.ncep.noaa.gov/archives/web_pages/sfc/ (Accessed August 10, 2020).

Pessanha, V. S., 2019: Modeling of Morphological Responses to a Storm Event During TREX13. Naval Postgraduate School.

Pessanha, V. S., P. C. Chu, and M. K. Gough, 2022: Sediment accretion in a lower-energetic location during two consecutive cold fronts. *J. Oper. Oceanogr.*, https://doi.org/10.1080/1755876X.2022.2100145.

Plant, N. G., J. W. Long, P. S. Dalyander, D. M. Thompson, and E. A. Raabe, 2013: Application of a hydrodynamic and sediment transport model for guidance of response efforts related to the Deepwater Horizon oil spill in the northern Gulf of Mexico along the coast of Alabama and Florida (Report number 2012–1234).

Putnam, J. A., 1949: Loss of wave energy due to percolation in a permeable sea bottom. *Eos, Trans. Am. Geophys. Union*, **30**, https://doi.org/10.1029/TR030i003p00349.

Qi, W. G., and F. P. Gao, 2018: Wave induced instantaneously-liquefied soil depth in a non-cohesive seabed. *Ocean Eng.*, **153**, 412–423, https://doi.org/https://doi.org/10.1016/j.oceaneng.2018.01.107.

Rennie, S. E., A. Brandt, and C. T. Friedrichs, 2017: Initiation of motion and scour burial of objects underwater. *Ocean Eng.*, **131**, https://doi.org/10.1016/j.oceaneng.2016.12.029.

Roelvink, D. J. A., and D. J. Walstra, 2005: Keeping it simple by using complex models. *Advances in Hydroscience and Engineering*, **6**.

van Rijn, L. C., 2013: Erosion of Coastal Dunes Due To Storms [online]. https://www.leovanrijn-sediment.com/papers/Coastalduneerosion2013.pdf (Accessed October 15, 2021).

van Rijn, L. C., D. J. R. Walstra, B. Grasmeijer, J. Sutherland, S. Pan, and J. P. Sierra, 2003: The predictability of cross-shore bed evolution of sandy beaches at the time scale of storms and seasons using process-based Profile models. *Coast. Eng.*, **47**, 295–327, https://doi.org/10.1016/S0378-3839(02)00120-5.

van Rijn, L., 1993: Principles of Sediment Transport in Rivers, Estuaries and Coastal Seas. Aqua Publications.

Roelvink, D., and A. Reniers, 2012: *A Guide to Modeling Coastal Morphology*. World Scientific, 292 pp.

Roelvink, D. J. A., and D. J. Walstra, 2005: Keeping It Simple By Using Complex Models. *Adv. Hydro–Science Eng.*, **6**, 1–11.

Rouse, H., 1938: *Fluid Mechanics for Hydraulic Engineers*. 1st Ed. Mcgraw-Hill Book Company Inc., 422 pp.

Sakai, T., K. Hatanaka, and H. Mase, 1992: Wave-Induced Effective Stress in Seabed and Its Momentary Liquefaction. *J. Waterw. Port, Coastal, Ocean Eng.*, **118**, 202–206, https://doi.org/https://doi.org/10.1061/(ASCE)0733-950X(1992)118:2(202).

SERDP, 2010: Munitions in the Underwater Environment: State of the Science and Knowledge Gaps (White Paper).

Shields, A., 1936: Application of Similarity Principles and Turbulence Research to Bed-load Movement (translated version). *Hydrodyn. Lab.*, **167**.

Sumer, B. M., C. Truelsen, T. Sichmann, and J. Fredsøe, 2001: Onset of scour below pipelines and self-burial. *Coast. Eng.*, **42**, https://doi.org/10.1016/S0378-3839(00)00066-1.

Sumer, M. B., 2006: Special Issue on Liquefaction around Marine Structures. *J. Waterw. Port, Coastal, Ocean Eng.*, **132**, https://doi.org/10.1061/(asce)0733-950x(2006)132:4(225).

Taiani, L., L. Benedet, L. Silveira, S. Keehn, N. Sharp, and R. Bonanata, 2012: Sand Borrow Area Design Refinement to Reduce Morphological Impacts: A Case Study of Panama City Beach, Florida, USA. *Coast. Eng. Proc.*, **1**, https://doi.org/10.9753/icce.v33.sediment.103.

Tonnon, P. K., L. C. van Rijn, and D. J. R. Walstra, 2007: The morphodynamic modelling of tidal sand waves on the shoreface. *Coast. Eng.*, **54**, 279–296, https://doi.org/10.1016/j.coastaleng.2006.08.005.

Traykovski, P. A., and T. Austin, 2017: Continuous Monitoring of Mobility, Burial and Re-exposure of Underwater Munitions in Energetic Nearshore Environments (Report No. MR-2319).

Trembanis, A. C., C. T. Friedrichs, M. D. Richardson, P. Traykovski, P. A. Howd, P. A. Elmore, and T. F. Wever, 2007: Predicting seabed burial of cylinders by wave-induced scour: Application to the sandy inner shelf off Florida and Massachusetts. IEEE *J. Ocean. Eng.*, **32**, https://doi.org/10.1109/JOE.2007.890958.

Verboom, G. K., and A. Slob, 1984: Weakly-reflective boundary conditions for two-dimensional shallow water flow problems. *Adv. Water Resour.*, **7**, 192–197, https://doi.org/10.1016/0309-1708(84)90018-6.

Vousdoukas, M. I., L. P. M. Almeida, and Ó. Ferreira, 2012: Beach erosion and recovery during consecutive storms at a steep-sloping, meso-tidal beach. *Earth Surf. Process. Landforms*, **37**, https://doi.org/10.1002/esp.2264.

Wang, Z., B. Liang, G. Wu, and B. W. Borsje, 2019: Modeling the formation and migration of sand waves: The role of tidal forcing, sediment size and bed slope effects. *Cont. Shelf Res.*, **190**, https://doi.org/10.1016/j.csr.2019.103986.

Whitehouse, R. J. S., 1997: Scour at marine structures: a manual for practical applications. Thomas Telford Publishing.

Wiberg, P. L., and C. R. Sherwood, 2008: Calculating wave-generated bottom orbital velocities from surface-wave parameters. *Comput. Geosci.*, **34**, https://doi.org/10.1016/j.cageo.2008.02.010.

Williams, J. J., and L. S. Esteves, 2017: Guidance on Setup, Calibration, and Validation of Hydrodynamic, Wave, and Sediment Models for Shelf Seas and Estuaries. *Adv. Civ. Eng.*, **2017**, 1–25, https://doi.org/10.1155/2017/5251902.

Willmott, C. J., 1981: On the Validation of Models. *Phys. Geogr.*, **2**, 184–194, https://doi.org/10.1080/02723646.1981.10642213.

Xu, J. P., F. L. Wong, R. Kvitek, D. P. Smith, and C. K. Paull, 2008: Sandwave migration in Monterey Submarine Canyon, Central California. *Mar. Geol.*, **248**, https://doi.org/10.1016/j.margeo.2007.11.005.

Yamamoto, T., H. L. Koning, H. Sellmeijer, and E. V. Van Hijum, 1978: On the response of a poro-elastic bed to water waves. *J. Fluid Mech.*, **87**, https://doi.org/10.1017/S0022112078003006.

Zen, K., and H. Yamazakim, 1991: Field observation and analysis of wave-induced liquefaction in seabed. *Soils Found.*, **31**, 161–179, https://doi.org/https://doi.org/10.3208/sandf1972.31.4_161.

——, D. S. Jeng, J. R. C. Hsu, and T. Ohyama, 1998: Wave-induced seabed instability: Difference between liquefaction and shear failure. *Soils Found.*, **38**, 37–47, https://doi.org/10.3208/sandf.38.2_37.

THIS PAGE INTENTIONALLY LEFT BLANK

INITIAL DISTRIBUTION LIST

1. Defense Technical Information Center
   Ft. Belvoir, Virginia

2. Dudley Knox Library
   Naval Postgraduate School
   Monterey, California

DUDLEY KNOX LIBRARY

NAVAL POSTGRADUATE SCHOOL

WWW.NPS.EDU

WHERE SCIENCE MEETS THE ART OF WARFARE